

1  
2

CONNECTING OBSERVED MICROBURST PRECIPITATION WITH ITS  
SCATTERING MECHANISM

3

by

Mykhaylo Sergeevich Shumko

4

A dissertation submitted in partial fulfillment  
of the requirements for the degree

of

Doctor of Philosophy

in

Physics

5

MONTANA STATE UNIVERSITY  
Bozeman, Montana

October 2019

6

7

©COPYRIGHT

8

by

Mykhaylo Sergeevich Shumko

2019

All Rights Reserved

## DEDICATION

<sup>9</sup> I dedicate this to all MSU students who use L<sup>A</sup>T<sub>E</sub>X. Dedication is optional  
<sup>10</sup> and may be no longer than one page, single spaced, and should precede the  
<sup>11</sup> acknowledgments page.

## ACKNOWLEDGEMENTS

<sup>12</sup> I would like acknowledge the countless engineers, technicians, and scientists who  
<sup>13</sup> made the FIREBIRD, AC-6, and RBSP missions a success. This work was supported  
<sup>14</sup> by Montana State University and by NASA Headquarters under the NASA Earth and  
<sup>15</sup> Space Science Fellowship Program - Grant 80NSSC18K1204. **Add co-author support.**

## TABLE OF CONTENTS

16	1. INTRODUCTION .....	1
17	Charged Particle Motion in Electric and Magnetic Fields .....	2
18	Particle Populations and Their Interractions in the Magnetosphere .....	8
19	Inner Magnetosphere Populations.....	11
20	Plasmasphere.....	13
21	Ring Current .....	15
22	Radiation Belts.....	16
23	Radiation Belt Particle Sources and Sinks .....	20
24	Adiabatic Heating .....	20
25	Wave Resonance Heating .....	21
26	Particle Losses .....	25
27	Microbursts .....	26
28	Scope of Reserach .....	29
29	2. CHAPTER TWO	
30	EVIDENCE OF MICROBURSTS OBSERVED NEAR THE EQUA-	
31	TORIAL PLANE IN THE OUTER VAN ALLEN RADIATION	
32	BELT .....	31
33	Contribution of Authors and Co-Authors .....	31
34	Manuscript Information .....	32
35	Key Points .....	33
36	Abstract .....	33
37	Introduction .....	33
38	Spacecraft Instrumentation .....	36
39	Observations .....	37
40	Analysis.....	40
41	Microburst and Source PSD .....	40
42	Motion of resonant electrons in phase space .....	43
43	Comparing the microburst PSD to diffusion theory .....	46
44	Discussion and Conclusions .....	48
45	Acknowledgments .....	49
46	3. CHAPTER THREE	
47	MICROBURST SCALE SIZE DERIVED FROM MULTIPLE BOUNCES	
48	OF A MICROBURST SIMULTANEOUSLY OBSERVED WITH	
49	THE FIREBIRD-II CUBESATS .....	51
50	Contribution of Authors and Co-Authors .....	51

## TABLE OF CONTENTS – CONTINUED

51	Manuscript Information .....	52
52	Key Points .....	53
53	Abstract .....	53
54	Introduction .....	54
55	Spacecraft and Observation .....	56
56	Analysis.....	59
57	Electron Bounce Period .....	60
58	Microburst Energy Spectra .....	62
59	Microburst Scale Sizes .....	62
60	Discussion and Conclusions .....	65
61	Acknowledgments .....	67
62	<b>4. CHAPTER FOUR</b>	
63	<b>MICROBURST SIZE DISTRIBUTION DERIVED WITH AEROCUBE-</b>	
64	<b>6 .....</b>	68
65	Contribution of Authors and Co-Authors .....	68
66	Manuscript Information .....	69
67	Key Points .....	70
68	Abstract .....	70
69	Introduction .....	71
70	Instrumentation.....	74
71	Methodology .....	75
72	Microburst Detection.....	75
73	Microburst Size Distribution in LEO and Magnetic Equator .....	77
74	Modeling the Distribution of Microburst Sizes .....	83
75	Monte Carlo and Analytic Models to Calculate $\bar{F}(s)$ .....	83
76	Methods for estimating optimal $\theta$ parameters.....	84
77	Estimating optimal parameters for various microburst size models.....	87
78	Discussion .....	89
79	Conclusions .....	94
80	Acknowledgments .....	95
82	<b>5. CONCLUSIONS AND FUTURE WORK .....</b>	96
83	Future Work.....	97
84	<b>REFERENCES CITED.....</b>	101

## TABLE OF CONTENTS – CONTINUED

<sup>85</sup>	APPENDIX: Appendix A.....	110
<sup>86</sup>	APPENDIX: Appendix B.....	113
<sup>87</sup>	APPENDIX: Appendix C.....	121

## LIST OF TABLES

Table		Page
88	C.1 Range of log-normal model parameters consistent 89 with the observed AC6 $\bar{F}(s)$ .....	124
90	C.2 Range of Weibull model parameters consistent with 91 the observed AC6 $\bar{F}(s)$ .....	124

## LIST OF FIGURES

Figure	Page
92      1.1 The three periodic motions of charged particles 93      in Earth's dipole magnetic field. These motions 94      are: gyration about the magnetic field line, bounce 95      motion between the magnetic poles, and azimuthal 96      drift around the Earth. Figure from (Baumjohann 97      and Treumann, 1997). ....	2
98      1.2 Charged particle motion in a uniform magnetic field 99 $\vec{B}$ . Panel (A) shows the geometry defining the 100     pitch angle, $\alpha$ . Panel (B) and (C) show two helical 101     electron trajectories with dashed lines assuming a 102     large and small $\alpha$ (corresponding to a small and large 103     parallel velocity $v_{  }$ ), respectively. ....	6
104     1.3 Contours of constant gyration, bounce, and drift 105     frequencies for electrons and protons in a dipole field. 106     Figure from Schulz and Lanzerotti (1974). ....	7
107     1.4 Macroscopic structures in the outer magnetosphere. 108     The solar wind with its frozen-in interplanetary 109     magnetic field is shown on the left and is traveling 110     supersonically towards the right. The solar wind 111     envelops Earth's magnetic field to create the mag- 112     netosphere cavity. Since the solar wind is traveling 113     supersonically, it creates a bow shock up stream. 114     Downstream of the bow shock the shocked solar wind 115     plasma inside the magnetosheath flows around the 116     magnetopause, a boundary between the solar wind 117     and magnetosphere. Figure from Baumjohann and 118     Treumann (1997). ....	9
119     1.5 Macroscopic structures in the inner magnetosphere 120     most relevant to this dissertation. The plasmas- 121     phere, and the radiation belts are shown and ring 122     current is co-located there as well. Sun is to the left. 123     Figure from Baumjohann and Treumann (1997). ....	10
124     1.6 The series of steps involved in magnetic reconnection 125     with a southward IMF. Figure from Baumjohann 126     and Treumann (1997). ....	12

## LIST OF FIGURES – CONTINUED

Figure	Page
127 128 129 130 131 132 133  1.7 Equipotential lines and electric field arrows due to the superposition of the co-rotation and convection electric fields. Electrons in the shaded region execute closed orbits. Outside of the shaded regions the electrons are not trapped and will escape. The region separating the two regimes is called the Alfvén layer. Figure from Baumjohann and Treumann (1997).....	14
134 135 136 137 138 139 140 141 142 143 144 145 146 147 148 149 150  1.8 The DST index during the St. Patrick's Day 2015 storm. This storm was caused by a coronal mass ejection on March 15th, 2015. The storm phases are: initial phase, main phase, and recovery phase. The initial phase occurred when the Dst peaked at +50 nT on March 17th during which the ring current was eroded by the coronal mass ejection during the interval shown by the red bar. Then the rapid decrease to $\approx -200$ nT was during the main phase where many injections from the magnetotail pumped up the ring current which reduced Earth's magnetic field strength at the ground and is shown with the green bar. Lastly, the recovery phase lasted from March 18th to approximately March 29th during which the ring current particles were lost and the ring current returned to its equilibrium state. The recovery phase is shown with the blue bar.....	17
151 152 153  1.9 The two radiation belts with a the locations of various satellites and orbits. Figure from (Horne et al., 2013). .....	18
154 155 156 157 158 159  1.10 The dynamics of the outer radiation belt in 1997 from the POLAR satellite. Top panel shows the 1.2-2.4 MeV electron flux as a function of L and 1997 day of year. The middle panel shows the DST index, and bottom panel shows the solar wind velocity. Figure from (Reeves et al., 2003). .....	19

## LIST OF FIGURES – CONTINUED

Figure	Page
160      1.11 The trajectories of an electron and a right-hand cir- 161      cularly polarized wave during a cyclotron resonance. 162      The electron's $v_{  }$ and the wave's $k_{  }$ are in opposite 163      directions such that the wave's frequency is Doppler 164      shifted to a integer multiple of the electron cyclotron 165      frequency. Figure from (Tsurutani and Lakhina, 1997). ....	22
166      1.12 Various wave modes in the magnetosphere. Ultra 167      low frequency waves occur throught the magneto- 168      sphere. Chorus waves are typically observed in 169      the 0-12 midnight-dawn region. EMIC waves are 170      typically observed in the dusk MLT sector. Hiss 171      waves are observed inside the plasmasphere. Figure 172      from Millan and Thorne (2007).....	24
173      1.13 An example train of microbursts observed by FIREBIRD- 174      II unit 4 on February 2nd, 2015. The colored curves 175      show the differential energy channel count rates in 176      six channels from $\approx 200$ keV to greater than 1 MeV. 177      The x-axis labels show auxiliary information such as 178      time of observation and the spacecraft position in L, 179      MLT, latitude and longitude coordinates. ....	27
180      1.14 Relativistic ( $> 1\text{MeV}$ ) distribution of microburst 181      occurrence rates as a function of L and MLT. The 182      three panels show the microburst occurrence rate 183      dependence on geomagnetic activity, parameterized 184      by the auroral electrojet (AE) index for (a) $\text{AE} <$ 185      100 nT, (b) $100 < \text{AE} < 300$ nT and (c) $\text{AE} > 300$ 186      nT. Figure from Douma et al. (2017).....	28

## LIST OF FIGURES – CONTINUED

Figure	Page
187 2.1 Electron and wave conditions from the MagEIS-A 188 and EMFISIS WFR sensors for the microburst time 189 interval. Panels (a), (b), and (c) are from RBSP-A 190 with its position information annotated in panel (a). 191 Panels (d), (e), and (f) are from RBSP-B with its 192 position information annotated in panel (d). Panel 193 (a) is the MagEIS-A high rate timeseries. Panels (b) 194 and (e) show the evolution of the MagEIS-A $J$ as a 195 function of $\alpha_L$ from the $\sim 40$ to $\sim 60$ keV channel. 196 Every 10th point is shown in panel (b). The solid 197 black line in panels (a) and (b) mark the end of 198 the time period used for the PSD fit extrapolation 199 analysis explained in section 3. The dashed black 200 lines in panels (a) and (b) show the time interval 201 used for the observed microburst PSD. Panels (c) 202 and (f) show the EMFISIS WFR spectra, with the 203 available burst data superposed. The red, green, and 204 cyan traces are equatorial $f_{ce0}$ , $f_{ce0}/2$ , and $f_{ce0}/10$ , 205 respectively. ....	39
206 2.2 Panel (a) shows the MagEIS-A high rate timeseries. 207 Panel (b) shows the RBSPICE EBR count rate 208 timeseries for $\zeta 19$ keV electrons. The microbursts 209 were observed between 11:17:10 - 11:17:12 UT and 210 are indicated with the vertical black arrows in panels 211 (a) and (b) for MagEIS-A times. Panel (c) shows the 212 RBSPICE EBR (family of relatively sparse sampled 213 curves) and MagEIS-A $J$ from the 29-41 keV energy 214 channel (single curve) as a function of $\alpha_L$ . The 215 vertical dashed lines show the time interval for the 216 PSD analysis.....	41

## LIST OF FIGURES – CONTINUED

Figure	Page
217      2.3 The colored annulus represents $f(p_\perp, p_{\parallel})$ in normalized momentum space, parallel and perpendicular to the background magnetic field. The microburst $f(p_\perp, p_{\parallel})$ is highlighted with the white circle. The columns show different powers of the sine extrapolation, and rows show the different magnetic latitudes of the scattering. The white dotted traces represent the boundary between the data and extrapolation. The green, red, and white solid traces are the resonance curves for $\omega = 0.2\Omega_{ce}$ , $0.4\Omega_{ce}$ , $0.6\Omega_{ce}$ , respectively. The cyan dashed traces are the diffusion curves for a $\omega = 0.4\Omega_{ce}$ wave (waves of other frequency have similar diffusion curves). The magnetic latitude of the scattering, the ratio of the plasma to the cyclotron frequency, and the power of the sine extrapolation is annotated in each panel. For the resonance and diffusion curves, the density model assumed a $n_L = 1 e^-/cm^3$ and $\psi = -1$ .....	44
235      3.1 HiRes data of the microburst observed at February 2nd, 2015 at 06:12:53 UT, smoothed with a 150 ms rolling average. The subsequent bounces showed some energy dispersion. As discussed in Appendix B, a time correction of -2.28 s was applied to FU3. While the flux from five energy channels is shown, only channels with reasonable counting statistics were used for the spatial scale analysis. Vertical colored bars show the $\sqrt{N}$ error every 10th data point and vertical black bars are lined up with the peaks in the 220-283 keV energy channel to help identify dispersion.	58

## LIST OF FIGURES – CONTINUED

Figure	Page
247 3.2 Observed and theoretical $t_b$ for electrons of energies 248 from 200 to 770 keV. The solid black line is $t_b$ 249 in a dipole magnetic field, derived in Schulz and 250 Lanzerotti (1974). The red dotted and cyan dashed 251 lines are the $t_b$ derived using the T89, and T04 252 magnetic field models with IRBEM-Lib. Lastly, 253 the blue dot-dash curve is the $t_b$ derived using the 254 Olson & Pfitzer Quiet model. The green and purple 255 rectangles represent the observed $t_b$ for FU3 and 256 FU4 using a Gaussian fit, respectively. The blue 257 rectangles represent the observed $t_b$ calculated with 258 the minima between the bounces. The width of the 259 boxes represent the width of those energy channels, 260 and the height represents the uncertainty from the fit.....	61
261 3.3 The topology of the FIREBIRD-II orbit and the 262 multiple bounces of the microburst projected onto 263 latitude and longitude with axis scaled to equal 264 distance. Attributes relating to FU3 shown in red 265 dashed lines, and FU4 with blue solid lines. The 266 spacecraft path is shown with the diagonal lines, 267 starting at the upper right corner. The labels P1- 268 4 for FU4 and P1-5 for FU3 indicate where the 269 spacecraft were when the $N^{th}$ peak was seen in 270 the lowest energy channel in the HiRes data. The 271 stars with the accompanying energy labels represent 272 the locations of the electrons with that energy that 273 started at time of P1, and were seen at the last peak 274 on each spacecraft. The rectangles represent the 275 lower bound of the microburst scale size, assuming 276 that the majority of the electrons were in the upper 277 boundary of energy channel 4.....	64
278 4.1 AC6 mission properties for (a) spacecraft separation 279 and (b) number of simultaneous quality 10 Hz 280 samples as a function of L and MLT.....	75

## LIST OF FIGURES – CONTINUED

Figure	Page
281      4.2 Examples of $> 35$ keV microbursts observed simultaneously by AC6-A in red and AC6-B in blue. Panels 282      (a), (c), (e), and (g) show the temporally-aligned 283      time series when AC6 were separated by $s = 5$ , 284      16, 37, and 69 km, respectively. The corresponding 285      panels (b), (d), (f), and (h) show the spatially- 286      aligned time series which is made by shifting the 287      AC6-A time series in the above panels by the in- 288      track lag (annotated with $dt$ ) that show any spatially 289      correlated structures. The clear temporal correla- 290      tion and lack of spatial correlation demonstrates that 291      these events are microbursts. ....	78
293      4.3 Microburst size distribution in low Earth orbit. 294      Panel (a) shows the percent of microbursts observed 295      above that separation after normalizing for the 296      uneven AC6 sampling in separation. Panel (b) shows 297      the microburst probability density (size histogram) 298      as a function of separation. Lastly, panel (c) shows 299      the normalization, i.e. number of simultaneous 300      samples AC6 observed as a function of separation. 301      The colored lines show the distributions binned by 302      L, and the thick black curve for the entire radiation 303      belt ( $4 < L < 8$ ). The gray shading around the 304      black curve shows the uncertainty due to counting 305      statistics. ....	81
306      4.4 Microburst size distribution mapped to the magnetic 307      equator in the same format as Fig. 4.3. ....	82

## LIST OF FIGURES – CONTINUED

Figure	Page
308      4.5 Panels A-C show the varying geometries of the 309      analytic model. The two spacecraft are shown 310      as black dots. The enclosing black circle around 311      each spacecraft bounds the area where a microburst 312      will be observed by one or both AC6 units if the 313      microburst's center lies inside the circle. Panel 314      (A) shows the case where microburst diameter is 315      smaller than the AC6 separation and all microbursts 316      will be observed by either unit A or B and never 317      simultaneously. Panel (B) shows the intermediate 318      case where the microburst diameter is comparable to 319      the AC6 separation and some fraction of microbursts 320      will be observed simultaneously. The fraction of the 321      microbursts simultaneously observed is proportional 322      to the circle intersection area $A(r, s)$ and is shown 323      with grey shading. Panel (C) shows the case where 324      the microburst diameter is much larger than the 325      spacecraft separation and nearly all microbursts will 326      be observed by both spacecraft. Lastly panel (D) 327      shows $\bar{F}(s)$ from the AC6 data with a solid black 328      line, and modeled MC and analytic $\bar{F}(s)$ curves for 329      a single-sized microburst distribution with $d = 40$ km.....	85
330      4.6 Range of plausible microburst sizes assuming all 331      microbursts are one fixed size. Panel (a) shows the 332      posterior probability density function of microburst 333      diameters in black. The red, green, and blue vertical 334      lines at 38, 73, and 129 km represent the 2.5, 50, and 335      97.5 posterior percentiles, respectively. A uniform 336      prior between 0 and 200 km was assumed for this 337      MCMC run and is shown in cyan. Panel (b) shows 338      the percent of microbursts observed above an AC6 339      separation for $4 < L < 8$ in black. The 2.5, 50 340      and 97.5 size percentiles were estimated from the 341      posterior and plotted in red, green, and blue curves, 342      respectively.....	90

## LIST OF FIGURES – CONTINUED

Figure	Page
343      4.7 Plausible microburst percent curves assuming mi- 344      croburst size distribution is bimodal consisting of 345      two sizes $d_0$ and $d_1$ with a mixing term that quanti- 346      fies the relative occurrence of the $d_0$ to $d_1$ microburst 347      populations. Panel (a) shows the posterior distri- 348      bution for the microburst population mixing term, 349 $a$ with a median value of 0.02. The $a$ prior was 350      uniform between 0 and 0.2. Panel (b) shows the 351      posterior distribution for $d_0$ , the larger microburst 352      population estimated with a uniform prior between 353      50 and 200 km and the posterior median diameter of 354      122 km. Panel (c) shows the posterior distribution 355      for $d_1$ , the smaller microburst population, estimated 356      using a uniform prior between 0 and 50 km with a 357      median diameter of 28 km. Panel (d) is similar to 358      Fig. 4.6b and shows the AC6 microburst fraction for 359 $4 < L < 8$ in black. A set of 1000 random parameter 360      triples ( $a$ , $d_0$ , and $d_1$ ) were drawn from the posterior 361      and used to generate a family of $\bar{F}(s)$ curves. At 362      each $s$ the range of consistent $\bar{F}(s)$ were quantified 363      by the 2.5, 50 and 97.5 percentiles and shown with 364      the red, green, and blue curves, respectively. .... 91	91
365      A.1 Panel (A) shows the magnetic power spectral density 366      as a function of frequency and time from the EMFI- 367      SIS WFR instrument on board RBSP-A. The “hiss- 368      like” wave used for the resonant diffusion analysis 369      was observed starting at 11:17:03 UT. In the same 370      format as panel (A), panel (B) shows the polar angle 371      of the wave vector for this time period. The wave 372      of interest had a normal wave vector, $\theta_k < 30^\circ$ . 373      Since the results in panel (B) are valid only for high 374      planarity, panel (C) shows planarity in the same 375      format as panels (A) and (B). The wave of interest 376      was found to have a planarity of $> 0.8$ . Lastly, panel 377      (D) shows the available burst mode data. .... 111	111

## LIST OF FIGURES – CONTINUED

Figure	Page
378      A.2 Ratio of the RBSPICE EBR at microburst times 379      indicated with the black vertical arrows in Fig. 2, 380      to the EBR at the same pitch angles one spin prior 381      (quiet time). The microburst flux was enhanced by 382      10-80% across $100^\circ < \alpha_L < 160^\circ$ PA, and appear to 383      be peaked closer to $\alpha_L = 90^\circ$ .....	112
384      B.1 Cross-correlation time lag analysis applied to a train 385      of microbursts. Panel (a) and (b) show the count 386      rate from the lowest energy channel. Panel (c) shows 387      the cross-correlation coefficient as a function of time 388      lag. Panel (d) shows the shifted timeseries. Clock 389      difference was 2.23 s .....	115
390      B.2 Same analysis as Fig. B.1 on a different time period. 391      Clock difference was 2.21 s.....	116
392      B.3 Same analysis as Fig. B.1 on a different time period. 393      Clock difference was 2.25 s.....	117
394      B.4 Same analysis as Fig. B.1 on a different time period. 395      Clock difference was 2.27 s.....	118
396      B.5 Same cross-correlation time lag analysis applied to 397      stationary spatial structures. The cross-correlation 398      lag between these events is a sum of the clock differ- 399      ence and time lag due to the spacecraft separation. 400      The lag derived at this time was 4.95 s .....	119
401      B.6 Same analysis as Fig. B.5 applied to a different 402      stationary spatial feature. The lag derived at this 403      time was 5.01 s .....	120

## NOMENCLATURE

$L$	L-Shell
$MLT$	magnetic local time
$\lambda$	magnetic latitude
$\alpha$	pitch angle
$\alpha_L$	local pitch angle at the spacecraft
$\alpha_{eq}$	pitch angle maped to the magnetic equator
$c$	speed of light
$R_E$	Earth's radius
$J$	flux
$f$	phase space density
$E$	energy
$E_0$	exponential e-folding energy
$p$	momentum
$\vec{E}$	electric field
$\vec{B}$	magnetic field
$B_w$	wave amplitude
$v$	velocity
$\Omega_e$	electron gyrofrequency
$\omega_{pe}$	plasma frequency
$k$	wave vector
$D_{xx}$	diffusion coefficient
$s$	spacecraft separation
$t_b$	electron bounce period

404

405

## INTRODUCTION

406 Above Earth's atmosphere are the a pair of Van Allen radiation belts, a complex  
407 and dynamic plasma environment that effects our technology-driven society. These  
408 effects include: a higher radiation dose for astronauts and cosmonauts, higher chance  
409 of spacecraft failure due to single event upsets that can lead to catastrophic latchups,  
410 degradation of silicon (changing the silicon doping) from an extended radiation dose  
411 that can degrade a transistor to the point where it no longer function as a switch,  
412 and the degradation of the ozone layer due to the chemical production of  $\text{NO}_X$  and  
413  $\text{HO}_X$  molecules. With these effects in mind, it is no surprise that the radiation belts  
414 have been extensively studied since their discovery in the 1960s.

415 One natural phenomenon in the radiation belts that has been a topic of interest  
416 in the space physics community is wave-particle intersections that, as we will explore  
417 throughout this dissertation, can accelerate particles to very high energies (e.g.  $\approx$   
418 MeV for electrons) and scatter them into the atmosphere.

419 The goal of this dissertation is to study the wave-particle mechanism that  
420 scatters microbursts, a sub-second impulse of electrons into Earth's atmosphere.  
421 Before we dive deep into the physics of wave-particle interactions, an introduction to  
422 Earth's magnetosphere is warranted. Single charged particle motion in Earth's electric  
423 and magnetic fields will be described first. Then the major particle populations in  
424 the magnetosphere and the coupling between them will be described. Lastly, a brief  
425 overview of wave-particle interactions and their effects will be presented.

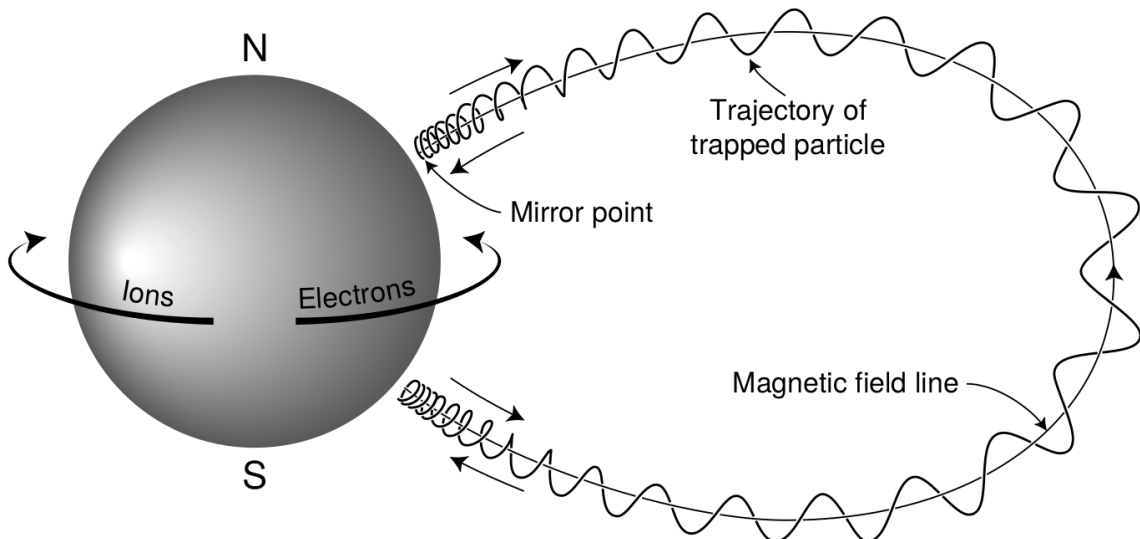


Figure 1.1: The three periodic motions of charged particles in Earth's dipole magnetic field. These motions are: gyration about the magnetic field line, bounce motion between the magnetic poles, and azimuthal drift around the Earth. Figure from (Baumjohann and Treumann, 1997).

426

### Charged Particle Motion in Electric and Magnetic Fields

A charged particle trapped in the magnetosphere will experience three types of periodic motion in Earth's nearly dipolar magnetic field. The three motions are ultimately due to the Lorentz force that a particle of momentum  $\vec{p}$ , charge  $q$ , and velocity  $\vec{v}$  experiences in an electric field  $\vec{E}$  and magnetic field  $\vec{B}$  and is given by

$$\frac{d\vec{p}}{dt} = q(\vec{E} + \vec{v} \times \vec{B}). \quad (1.1)$$

- 427 In the magnetosphere, the three periodic motions in decreasing frequency are gyration,  
 428 bounce, and drift and are schematically shown in Fig. 1.1. Each of these  
 429 motions have a corresponding conserved quantity i.e. an adiabatic invariant.

The highest frequency periodic motion is gyration about a magnetic field of

magnitude  $B$ . This motion is circular with a Larmor radius of

$$r = \frac{mv_{\perp}}{|q|B} \quad (1.2)$$

where  $m$  is the mass and  $v_{\perp}$  the particle's velocity perpendicular to  $\vec{B}$ . This motion has a corresponding gyrofrequency

$$\Omega = \frac{|q|B}{m} \quad (1.3)$$

in units of radians/second. Inside the radiation belts the electron gyrofrequency,  $\Omega_e$  is on the order of a kHz. The corresponding adiabatic invariant is found by integrating the particle's canonical momentum around the particle's path of gyration

$$J_i = \oint (\vec{p} + q\vec{A}) \cdot d\vec{l} \quad (1.4)$$

where  $J_i$  is the  $i^{th}$  adiabatic invariant and  $\vec{A}$  is the magnetic vector potential. This integral is carried out by integrating the first term over the circumference of the gyro orbit and integrating the second term using Stokes theorem to calculate the magnetic flux enclosed by the gyro orbit. With suitable integration,  $J_1 \sim v_{\perp}^2/B$  and is conserved as the frequency of the driving force,  $\omega$  satisfies  $\omega \ll \Omega_e$ .

The second highest frequency periodic motion is bouncing due to a parallel gradient in  $\vec{B}$ . This periodic motion naturally arises in the magnetosphere because Earth's magnetic field is stronger near the poles, and artificially in the laboratory in magnetic bottle machines. To understand this motion we first we need to define the concept of pitch angle  $\alpha$  as the angle between  $\vec{B}$  and  $\vec{v}$  which is schematically shown in Fig. 1.2a. The pitch angle relates  $v$  with  $v_{\perp}$ , and  $v_{||}$  (the component of the particles velocity parallel to  $\vec{B}$ ). As shown in 1.2b and c, a larger  $\alpha$  will tighten the

<sup>442</sup> particle's helical trajectory and vice versa.

Assuming the particle's kinetic energy is concerned, the conservation of  $J_1$  implies that given a particle's  $v_{\perp}(0)$  and  $B(0)$  at the magnetic equator (where Earth's magnetic field is usually at a minimum), we can calculate its  $v_{\perp}(s)$  along the particle's path  $s$  by calculating  $B(s)$  from magnetic field models. The particle's perpendicular velocity is then related via

$$\frac{v_{\perp}^2(0)}{B(0)} = \frac{v_{\perp}^2(s)}{B(s)} \quad (1.5)$$

<sup>443</sup> which can be rewritten as

$$\frac{v^2 \sin^2 \alpha(0)}{B(0)} = \frac{v^2 - v_{\parallel}^2(s)}{B(s)} \quad (1.6)$$

<sup>444</sup> and re-arranged to solve for  $v_{\parallel}(s)$

$$v_{\parallel}(s) = v \sqrt{1 - \frac{B(s)}{B(0)} \sin^2 \alpha(0)} \quad (1.7)$$

<sup>445</sup> which will tend towards 0 when the second term in the radical approaches 1.

<sup>446</sup> The location where  $v_{\parallel}(s) = 0$  is called the mirror point and is where a particle  
<sup>447</sup> stops and reverses direction. Since Earth's magnetic field is stronger towards the  
<sup>448</sup> poles, the mirroring particle will execute periodic bounce motion between its two  
<sup>449</sup> mirror points in the northern and southern hemispheres. The corresponding adiabatic  
<sup>450</sup> invariant,  $J_2$  is

$$J_2 = \oint p_{\parallel} ds \quad (1.8)$$

where  $ds$  describes the particle path between the mirror points in the northern and southern hemispheres (see Fig. 1.1).  $J_2$  is found by substituting Eq. 1.7 into Eq. 1.8 and defining the magnetic field strength at the mirror points as  $B_m$  where  $\alpha(m) = 90^\circ$ .

The  $J_2$  integral can be written as

$$J_2 = 2p \int_{m_n}^{m_s} \sqrt{1 - \frac{B(s)}{B(m)}} ds \quad (1.9)$$

451 where  $m_n$  and  $m_s$  are the northern and southern mirror points, respectively. The  
452 bounce period can be estimated (e.g. Baumjohann and Treumann, 1997) to be

$$t_b \approx \frac{LR_e}{\sqrt{W/m}} (3.7 - 1.6 \sin \alpha(0)) \quad (1.10)$$

453 where  $L$  is the  $L$ -shell which describes the distance from the Earth's center to the  
454 location where a particular magnetic field line crosses the magnetic equator, in units  
455 of Earth radii,  $R_e$ .  $W$  is the particle's kinetic energy. As with gyration, a particle  
456 bounces as long as  $\omega \ll \Omega_b$ , where  $\Omega_b$  is the bounce frequency.

457 At this stage it is instructional to introduce the notion of the loss cone pitch  
458 angle,  $\alpha_L$ . A particle with  $\alpha \leq \alpha_L$  will mirror at or below  $\approx 100$  km altitude in the  
459 atmosphere. A particle at those altitudes will encounter Earth's atmosphere and has  
460 a significant probability of Coulomb scattering with atmospheric particles and be lost  
461 to the atmosphere.

462 The slowest periodic motion experienced by charged particles in Earth's mag-  
463 netic field is azimuthal drift around the Earth. This drift results from a combination of  
464 a radial gradient in  $\vec{B}$  and the curvature of the magnetic field. The radial gradient drift  
465 arises because Earth's magnetic field is stronger near the Earth where the particle's  
466 gyroradius radius of curvature is smaller as it gyrates towards stronger magnetic field,  
467 and larger when it gyrates outward. The overall effect is the particle gyro orbit does  
468 not close on itself and negatively charged particles drift East and positively charged  
469 particles drift West. The radial gradient drift is enhanced by the centrifugal force that  
470 a particle experiences as it bounces along the curved field lines. The drift adiabatic

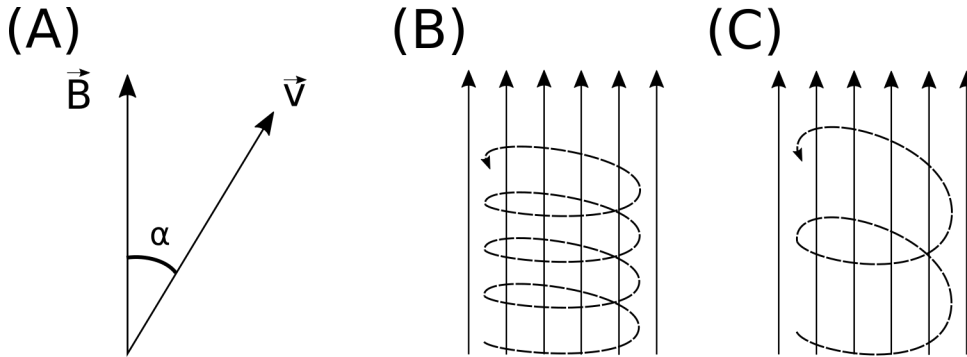


Figure 1.2: Charged particle motion in a uniform magnetic field  $\vec{B}$ . Panel (A) shows the geometry defining the pitch angle,  $\alpha$ . Panel (B) and (C) show two helical electron trajectories with dashed lines assuming a large and small  $\alpha$  (corresponding to a small and large parallel velocity  $v_{||}$ ), respectively.

<sup>471</sup> invariant,  $J_3$  is found by integrating Eq. 1.4 over the complete particle orbit around  
<sup>472</sup> the Earth. The shape of this drift orbit is otherwise known as a drift shell. For  $J_3$ ,  
<sup>473</sup> the first term is negligible and the second term is the magnetic flux enclosed by the  
<sup>474</sup> drift shell,  $\Phi_m$  i.e.  $J_3 \sim \Phi_m$ .

<sup>475</sup> Figure 1.3 from Schulz and Lanzerotti (1974) shows contours of the gyration,  
<sup>476</sup> bounce, and drift frequencies for electrons and protons in Earth's dipole magnetic  
<sup>477</sup> field.

Up until now we have considered the three periodic motions due Earth's magnetic field and the absence of electric fields. If  $\vec{E}$  is present, a particle's center of gyration i.e., averaged position of the particle over a gyration, will drift with a velocity perpendicular to both  $\vec{E}$  and  $\vec{B}$ . The drift velocity can be solved directly from Eq. 1.1 and is

$$\vec{v}_E = \frac{\vec{E} \times \vec{B}}{B^2}. \quad (1.11)$$

<sup>478</sup> Lastly, for more detailed derivations of these motions, see the following texts:  
<sup>479</sup> Baumjohann and Treumann (1997); Schulz and Lanzerotti (1974); Tsurutani and  
<sup>480</sup> Lakhina (1997).

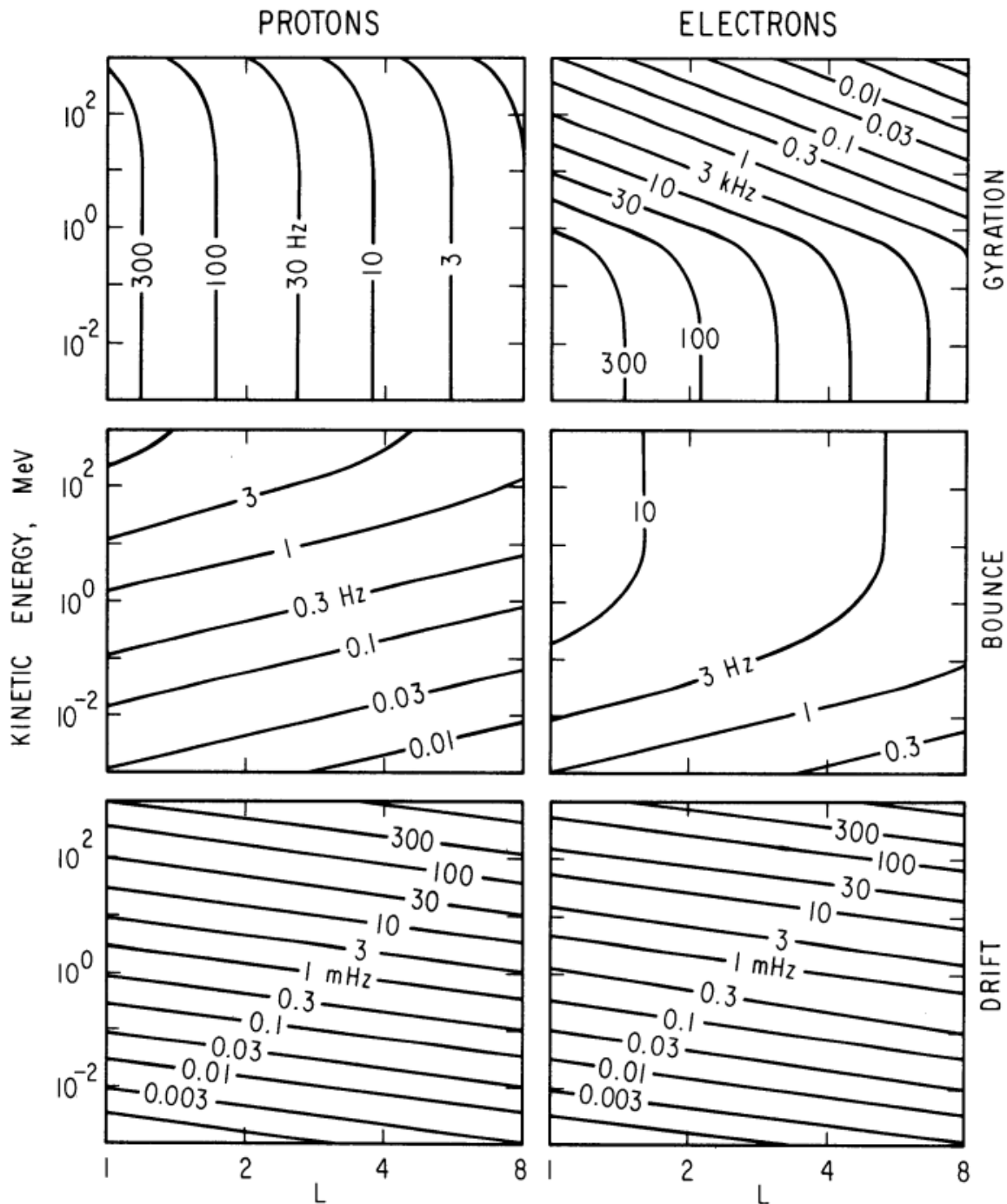


Figure 1.3: Contours of constant gyration, bounce, and drift frequencies for electrons and protons in a dipole field. Figure from Schulz and Lanzerotti (1974).

---

481        Particle Populations and Their Interractions in the Magnetosphere

482        The single-particle motion in Earth's magnetic field described in the previous  
483        section is a prerequisite to understanding how magnetospheric particles organize into  
484        macroscopic populations. The structure of the outer magnetosphere is shown in Fig.  
485        1.4 and inner magnetosphere in Fig. 1.5. In this section we will introduce the various  
486        particle populations in the magnetosphere and how they couple.

487        The sun and its solar wind are ultimately the source of energy input into the  
488        magnetosphere. The solar wind at Earth's orbit is a plasma traveling at supersonic  
489        speeds with an embedded interplanetary magnetic field (IMF). When the solar wind  
490        encounters Earth's magnetic field the plasma can not easily penetrate into the  
491        magnetosphere, rather it drapes around the magnetosphere forming a cavity in the  
492        solar wind that is roughly shaped as shown in Fig. 1.4. Because the solar wind is  
493        supersonic at 1 AU, a bow shock exists upstream of the magnetosphere. The solar  
494        wind plasma, after it is shocked by the bow shock, flows around the magnetosphere  
495        inside the magnetosheath. The surface where the solar wind ram pressure and Earth's  
496        magnetic pressure balance is termed the magnetopause, which can be thought of as  
497        a boundary between the solar wind's and Earth's plasma environments. This is  
498        a slightly naive description of the magnetopause, but is nonetheless an instructive  
499        conceptual picture. The shocked plasma then flows past the Earth where it shapes  
500        the magnetotail. In the magnetotail the solar wind magnetic pressure balances Earth's  
501        magnetic field pressure in the lobes. The magnetotail extends on the order of 100  
502         $R_E$  downstream of Earth [Add citation](#), and the tailward stretching of magnetic field  
503        lines creates the plasma sheet which exists in the region of low magnetic field strength  
504        near the magnetic equator [Add citation](#). The plasma sheet flows from dusk to dawn  
505        (out of the page in Figs. 1.4 and 1.5) and this current is connected to a zoo of other

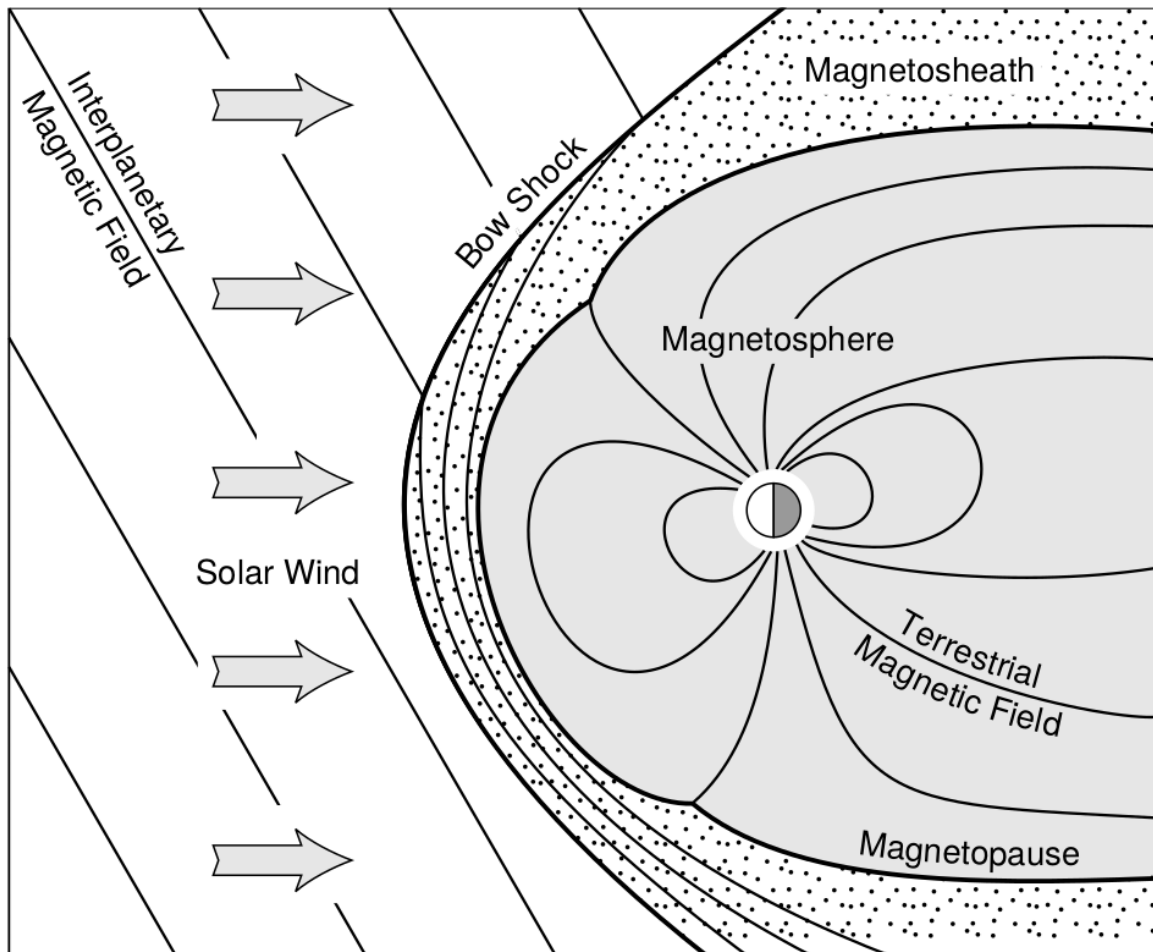


Figure 1.4: Macroscopic structures in the outer magnetosphere. The solar wind with its frozen-in interplanetary magnetic field is shown on the left and is traveling supersonically towards the right. The solar wind envelops Earth's magnetic field to create the magnetosphere cavity. Since the solar wind is traveling supersonically, it creates a bow shock up stream. Downstream of the bow shock the shocked solar wind plasma inside the magnetosheath flows around the magnetopause, a boundary between the solar wind and magnetosphere. Figure from Baumjohann and Treumann (1997).

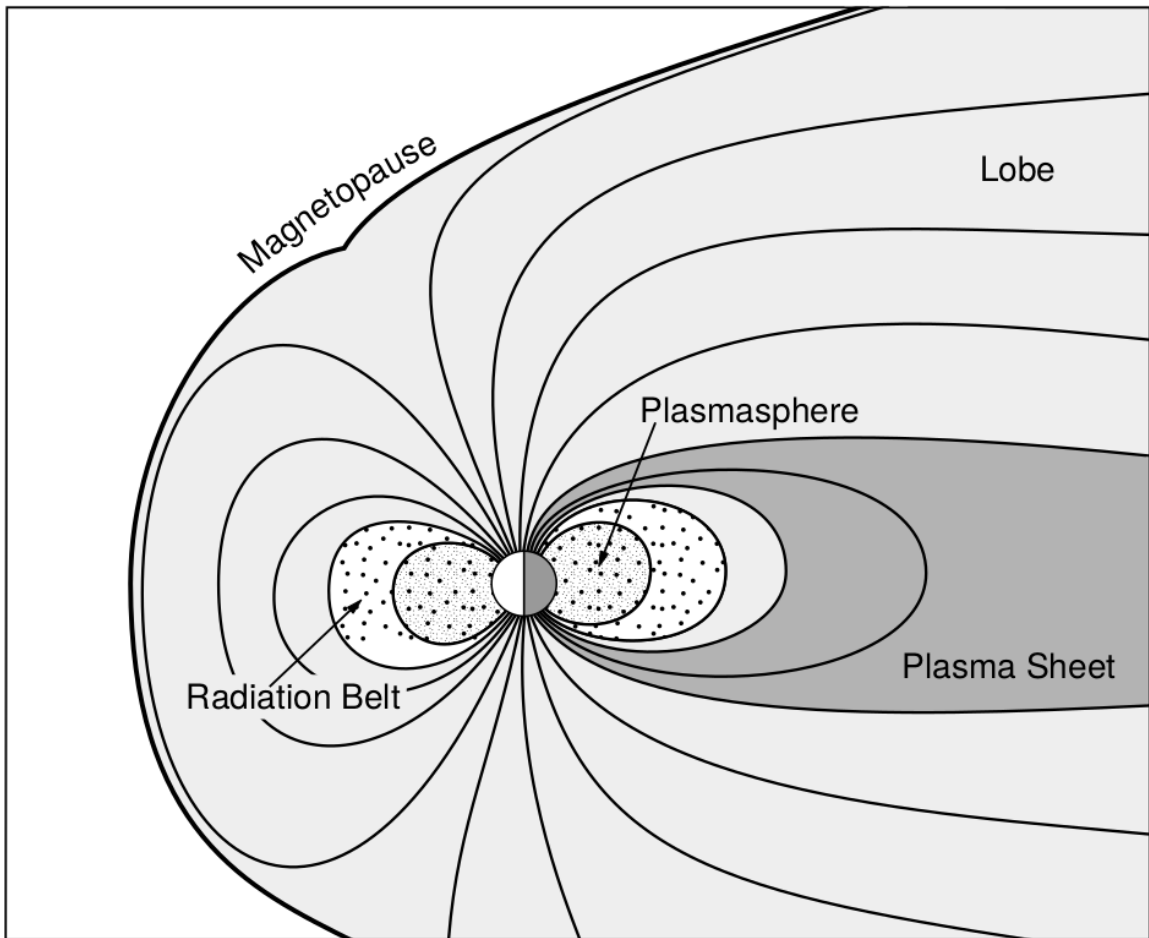


Figure 1.5: Macroscopic structures in the inner magnetosphere most relevant to this dissertation. The plasmasphere, and the radiation belts are shown and ring current is co-located there as well. Sun is to the left. Figure from Baumjohann and Treumann (1997).

506 currents in the magnetosphere which is beyond the scope of this dissertation.

507 The idea of the magnetopause as a barrier between the solar wind and  
 508 the magnetosphere is not entirely accurate due to the presence of reconnection.  
 509 Reconnection was first conceived by Dungey (1961) who described the convection of  
 510 Earth's magnetic field between the bow and tail regions of the magnetosphere. This  
 511 process is known as the Dungey cycle and is most effective when the IMF is pointing  
 512 southward as is shown in Fig. 1.6 part 1. As the IMF contacts Earth's magnetic  
 513 field it reconnects with it so that Earth's magnetic field is directly connected to the  
 514 IMF. Then as the solar wind flows tailward the IMF drags Earth's magnetic field  
 515 towards the magnetotail as shown in Fig. 1.6 parts 2-6. As more and more magnetic  
 516 field lines are draped in the magnetotail, magnetic pressure increases in the lobes  
 517 which squeezes the plasma sheet until Earth's magnetic field reconnects as is shown  
 518 in Fig. 1.6 part 7. Lastly, Fig. 1.6 part 8 shows the newly merged magnetic field  
 519 line and the plasma frozen on it moves Earthward under the magnetic tension force  
 520 to become more dipolar. This is called a dipolarization of the magnetic field, and the  
 521 plasma frozen on these field lines can be observed as injections (e.g. Turner et al.,  
 522 2015). Injection of plasma into the inner magnetosphere is one of the drivers of inner  
 523 magnetosphere dynamics. Should I talk about the K-H instability and how there  
 524 could be micro reconnection? i.e. cite a paper or two that support or refute that  
 525 idea.

526 Inner Magnetosphere Populations

527 Before we describe the inner magnetosphere particle populations, we first need to  
 528 describe the coordinate system used to organize the inner magnetosphere populations.  
 529 The first coordinate was defined in section 1 and is the L shell. L shell can be thought  
 530 of as an analogue to a radius but in a dipole geometry. The azimuthal coordinate

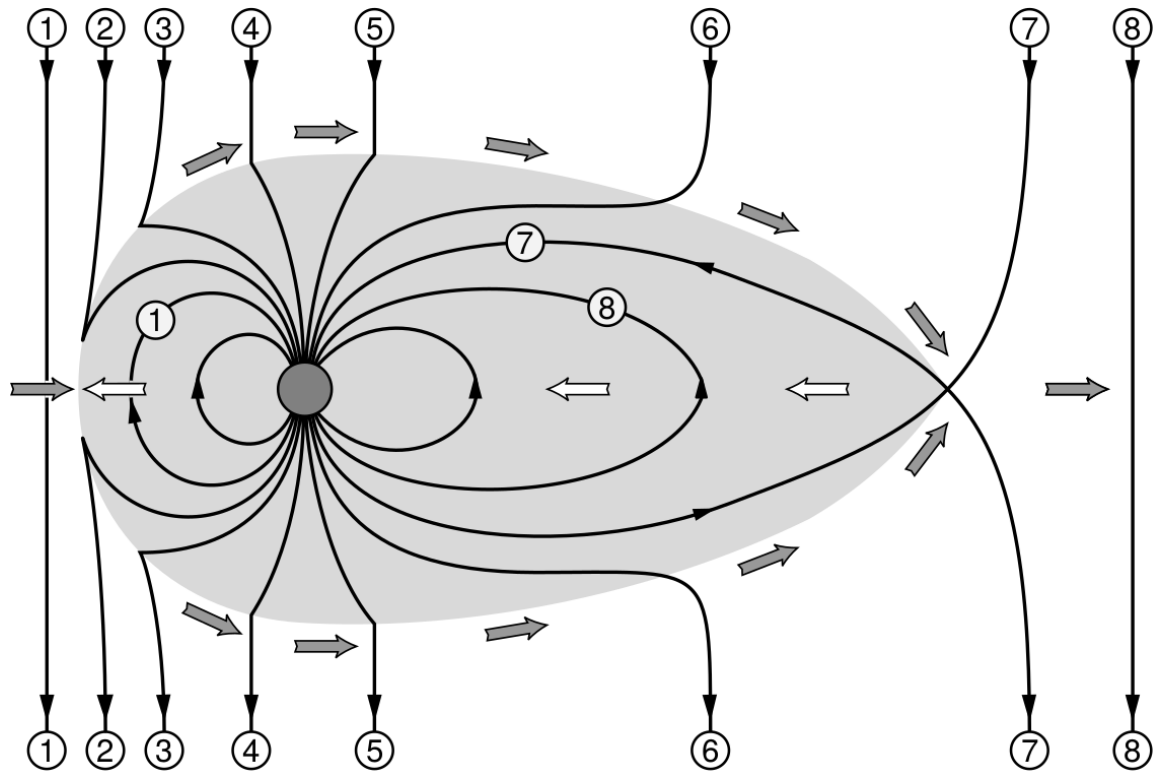


Figure 1.6: The series of steps involved in magnetic reconnection with a southward IMF. Figure from Baumjohann and Treumann (1997).

531 is the magnetic local time (MLT). For an observer above Earth's north pole looking  
 532 down, MLT is defined to be 0 (midnight) in the anti-sunward direction, and increases  
 533 in the counter-clockwise direction with 6 at dawn, 12 at noon (sunward direction),  
 534 and 18 in dusk. The last coordinate used in this dissertation is the magnetic latitude,  
 535  $\lambda$  which is analogous to the latitude coordinate and is defined to be 0 at the magnetic  
 536 equator.

537 The low energy particle dynamics in the inner magnetosphere are organized by  
 538 two electric fields: the co-rotation and the dawn-dusk electric fields. The co-rotation  
 539 electric field arises from the rotation of Earth's magnetic field. Since particles are  
 540 frozen on magnetic field lines and the plasma conductivity is effectively infinite, to  
 541 a non-rotating observer, Earth's rotation appears as a radial electric field that drops  
 542 off as  $\sim L^2$ . This electric field makes particles orbit around the Earth due to the  
 543  $\vec{E} \times \vec{B}$  drift. The other electric field, pointing from dawn to dusk is called the  
 544 convection electric field and is formed by the Earthward transport of particles from  
 545 the magnetotail that appears as an electric field to a stationary observer (with respect  
 546 to Earth). The superposition of the co-rotation and convection electric fields  
 547 results in a potential field shown in Fig. 1.7. The shaded area in Fig. 1.7 shows  
 548 the orbits on which low energy electrons are trapped, and outside are the untrapped  
 549 particles. The dynamic topology of the shaded region in Fig. 1.7 is controlled by only  
 550 the convection electric field which is dependent on the solar wind speed and the IMF.  
 551 The lowest energy particles, that are most effected by these electric fields, make up  
 552 the plasmasphere.

553 Plasmasphere The plasmasphere is a dense ( $n_e \sim 10^3/\text{cm}^3$ ), cool plasma  
 554 ( $\sim \text{eV}$ ) that extends to  $L \sim 4$  (extent is highly dependent on the solar wind and  
 555 magnetospheric conditions) and is sourced from the ionosphere. The two main

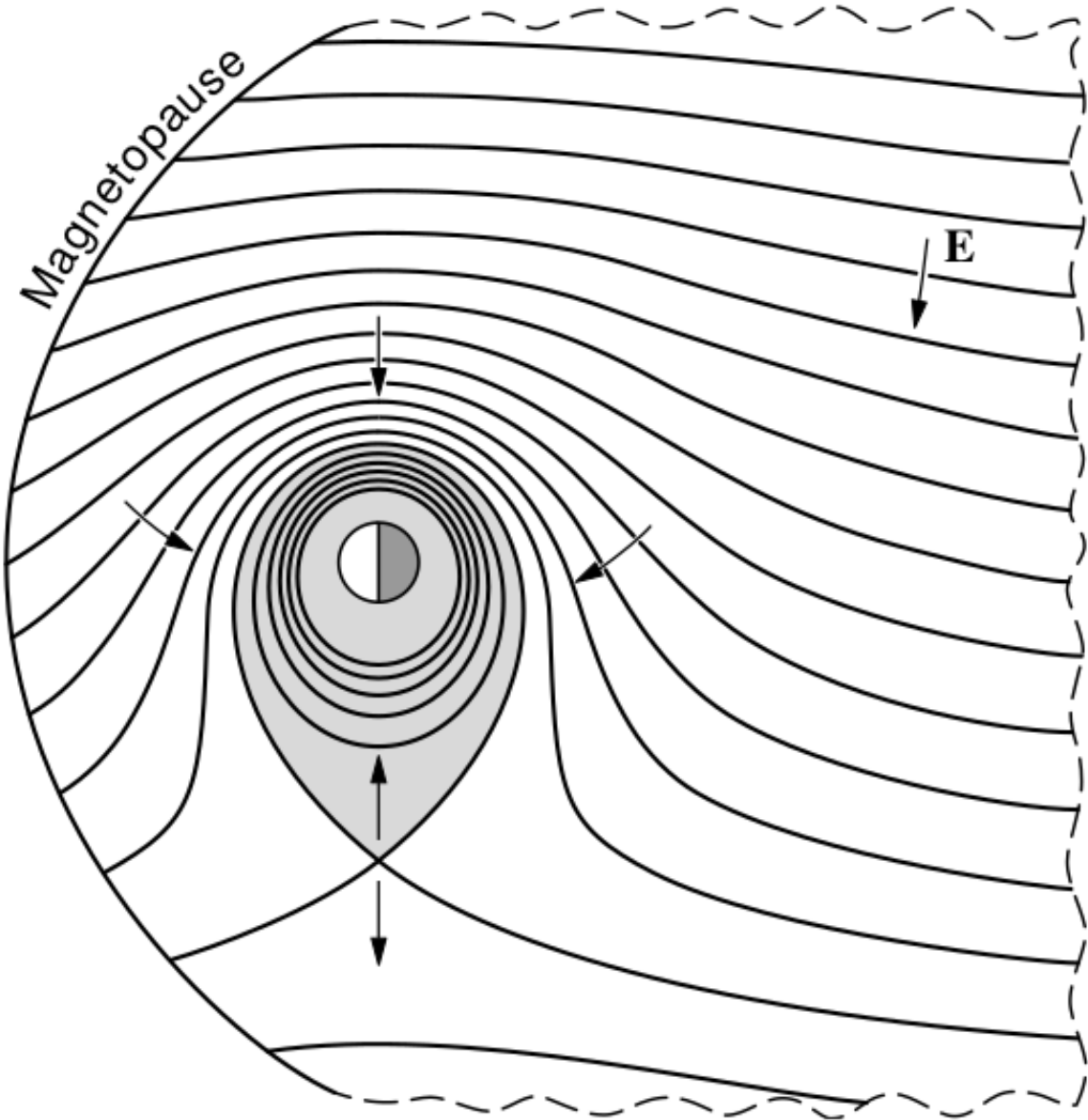


Figure 1.7: Equipotential lines and electric field arrows due to the superposition of the co-rotation and convection electric fields. Electrons in the shaded region execute closed orbits. Outside of the shaded regions the electrons are not trapped and will escape. The region separating the two regimes is called the Alfvén layer. Figure from Baumjohann and Treumann (1997).

556 mechanisms that source the cold plasma from the ionosphere are ultraviolet ionization  
 557 by sunlight and particle precipitation. The ultraviolet ionization by sunlight is  
 558 strongly dependent on the time of day (day vs night), latitude (more ionization near  
 559 the equator). The ionization due to particle precipitation, on the other hand, is highly  
 560 dependent on magnetospheric conditions, and mostly occurs at high latitudes.

561 The outer boundary of the plasmasphere is the plasmapause which is typically  
 562 identified as a steep radial gradient in plasma density from  $\sim 10^3/\text{cm}^3$  to  $\sim 1/\text{cm}^3$ . As  
 563 we will see throughout this dissertation, the location of the plasmapause is important  
 564 to model (e.g. O'Brien and Moldwin, 2003) and understand since the plasma density  
 565 strongly controls the efficiency of particle scattering (Horne et al., 2005).

566 Ring Current The next higher energy population is the ring current. This  
 567 population consists of protons and electrons between tens and a few hundred keV  
 568 that drift around the Earth. The orbits of higher energy particles are not as effected  
 569 by the convection and co-rotation electric field, rather they drift around the Earth  
 570 due to gradient and curvature drifts. Since the direction of the drift is dependent on  
 571 charge, protons drift west around the Earth and electrons drift East. This has the  
 572 effect of creating a current around the Earth.

573 The ring current generates a magnetic field which decreases the magnetic field  
 574 strength on Earth's surface and increases it outside of the ring current. The decrease  
 575 of Earth's magnetic field strength is readily observed by a system of ground-based  
 576 magnetometers and is merged into a Disturbance Storm Time (DST) index. An  
 577 example of a DST index time series from a coronal mass ejection (CME) driven 2015  
 578 St. Patrick's Day storm is shown in Fig. 1.8. The ring current is sometimes first  
 579 depleted and DST increases slightly (initial phase or sudden storm commencement).  
 580 Then the ring current is rapidly built up during which DST rapidly decreases (main

phase). Lastly the ring current gradually decays toward its equilibrium state over a period of a few days and DST increases towards 0 (recovery phase). The DST index along with other indicies are readily used by the space physics community to quantify the global state of the magnetosphere.

Radiation Belts The highest energy particle populations are in the Van Allen radiation belts. These belts were discovered by Van Allen (1959) and Vernov and Chudakov (1960) during the Cold War and are a pair of toroidally shaped populations of trapped electrons and protons usually within to  $L < 8$  and are shown in Fig. 1.9. Their quiescent toroidal shape is similar to the shape of the plasmasphere and ring current and is a result of Earth's dipole magnetic field and the conservation of the three adiabatic invariants discussed in section 1.

The inner radiation belt is extremely stable on time periods of years, extends to  $L \approx 2$ , and mainly consists of protons with energies between MeV and GeV and electrons with energies up to  $\approx 1$  MeV (Claudepierre et al., 2019). The source of inner radiation belt protons is believed to be due to cosmic-ray albedo neutron decay (e.g. Li et al., 2017) and inward radial diffusion for electrons (e.g. O'Brien et al., 2016a). The gap between the inner and outer radiation belt is called the slot, which is believed to be due to hiss waves inside the plasmasphere (described below) scattering particles into the atmosphere (e.g. Breneman et al., 2015; Lyons and Thorne, 1973).

The outer radiation belt, on the other hand is much more dynamic and consists of mainly electrons of energies up to a few MeV. The outer belt's spatial extent is highly variable e.g. see Fig. 1.10, and is typically observed at  $4 < L < 8$ . Since the outer radiation belt contains a dynamic population of energetic particles that pose a threat to human and technological presence in Earth's atmosphere and space, decades of research has been undertaken to understand and predict the outer radiation

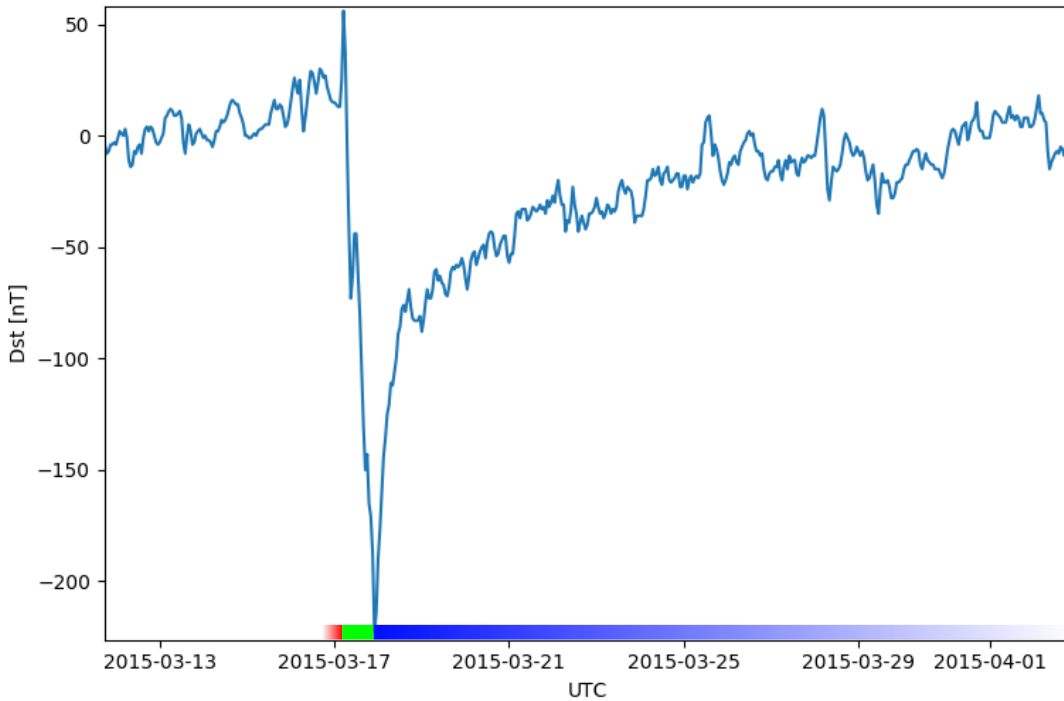


Figure 1.8: The DST index during the St. Patrick's Day 2015 storm. This storm was caused by a coronal mass ejection on March 15th, 2015. The storm phases are: initial phase, main phase, and recovery phase. The initial phase occurred when the Dst peaked at +50 nT on March 17th during which the ring current was eroded by the coronal mass ejection during the interval shown by the red bar. Then the rapid decrease to  $\approx -200$  nT was during the main phase where many injections from the magnetotail pumped up the ring current which reduced Earth's magnetic field strength at the ground and is shown with the green bar. Lastly, the recovery phase lasted from March 18th to approximately March 29th during which the ring current particles were lost and the ring current returned to its equilibrium state. The recovery phase is shown with the blue bar.

## The Earth's Electron Radiation Belts

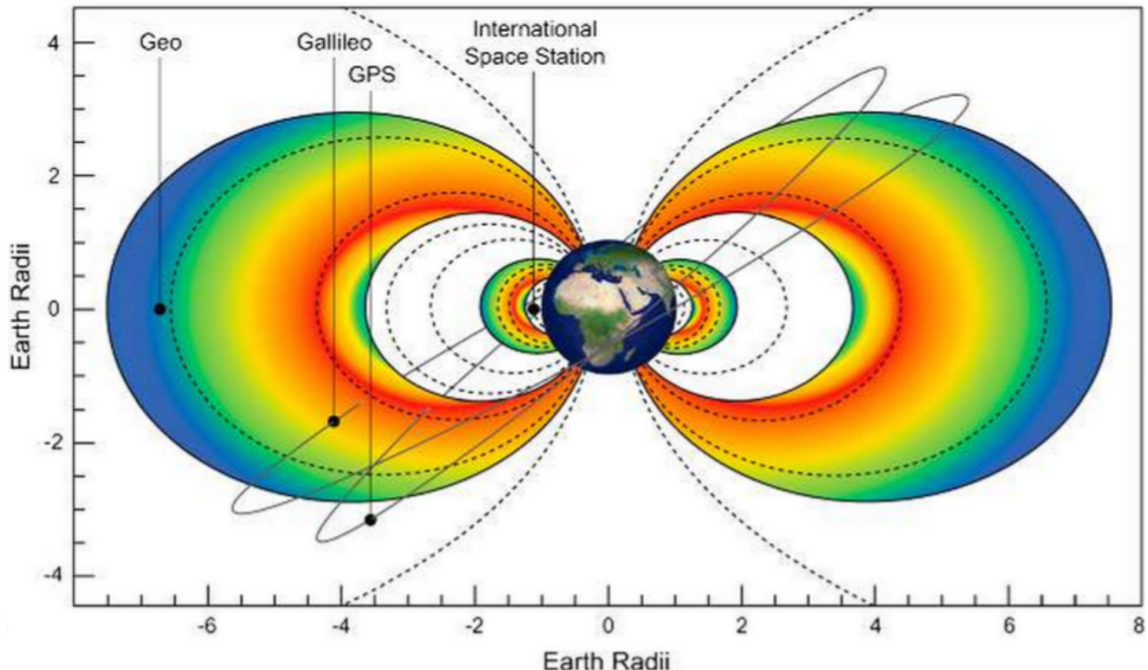


Figure 1.9: The two radiation belts with the locations of various satellites and orbits.  
Figure from (Horne et al., 2013).

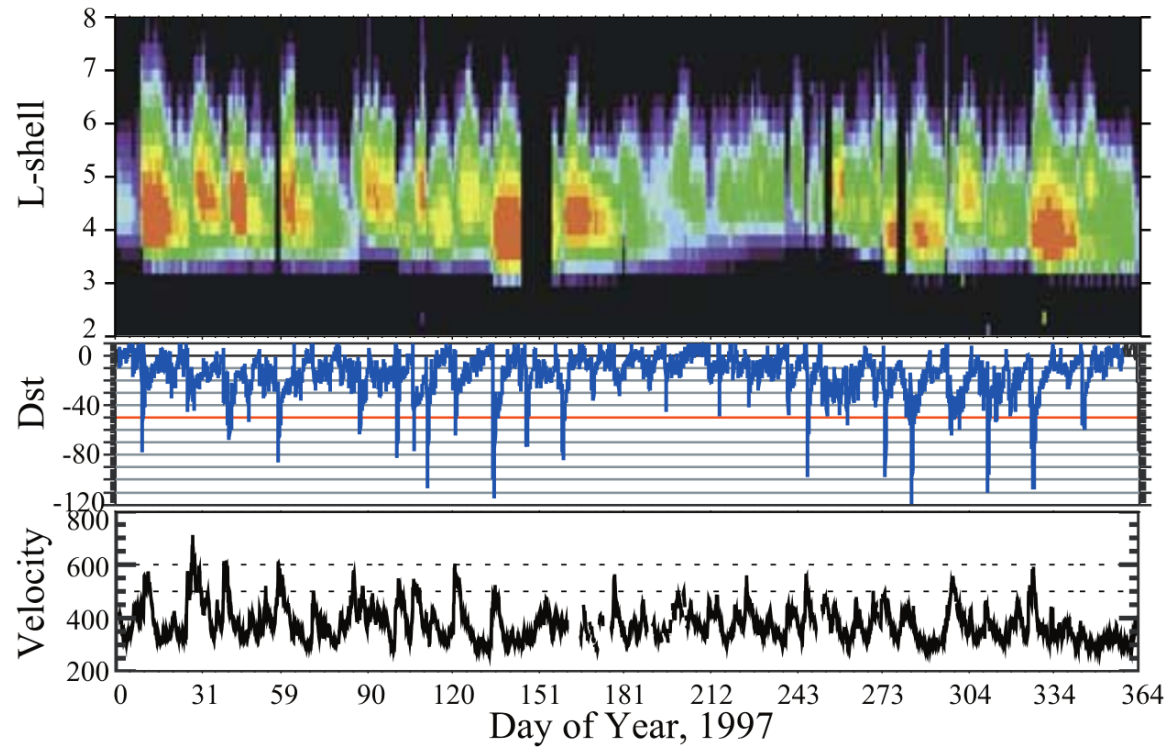


Figure 1.10: The dynamics of the outer radiation belt in 1997 from the POLAR satellite. Top panel shows the 1.2-2.4 MeV electron flux as a function of L and 1997 day of year. The middle panel shows the DST index, and bottom panel shows the solar wind velocity. Figure from (Reeves et al., 2003).

606 belt particles, waves, and wave-particle interactions. The dynamics of the outer  
 607 radiation belt can be understood by considering various competing acceleration and  
 608 loss mechanisms which will be described in the following sections.

609 Radiation Belt Particle Sources and Sinks

610 Adiabatic Heating

611 One of the particle heating and transport mechanisms arises from the Earthward  
 612 convection of particles. The conservation of  $J_1$  implies that the initial and final  $v_\perp$   
 613 depends on the change in the magnetic field amplitude

$$\frac{v_{\perp i}^2}{B_i} = \frac{v_{\perp f}^2}{B_f}. \quad (1.12)$$

614 As a particle convects Earthward,  $B_f > B_i$  thus  $v_\perp$  must increase. The dipole  
 615 magnetic field amplitude can be written as

$$B(L, \theta) = \frac{31.2 \text{ }\mu\text{T}}{L^3} \sqrt{1 + 3 \cos^2 \theta} \quad (1.13)$$

616 which implies that

$$\frac{v_{\perp f}^2}{v_{\perp i}^2} = \left( \frac{L_i}{L_f} \right)^3. \quad (1.14)$$

617 .

618 In addition, as the particle convects Earthward the distance between the  
 619 particle's mirror points decrease. If  $J_2$  is conserved, the shrinking bounce path implies  
 620 that  $v_{||}$  must increase by

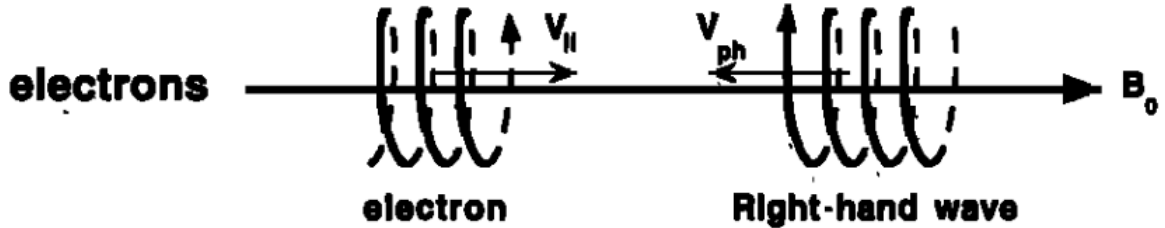
$$\frac{v_{||f}^2}{v_{||i}^2} = \left( \frac{L_i}{L_f} \right)^k \quad (1.15)$$

621 where  $k$  ranges from 2 for equatorial pitch angles,  $\alpha_{eq} = 0^\circ$ , to 2.5 for  $\alpha_{eq} = 90^\circ$   
 622 (Baumjohann and Treumann, 1997). Since the rate of adiabatic heating is greater in  
 623 the perpendicular direction than heating in the parallel direction, an initially isotropic  
 624 particle distribution will become anisotropic during its convection. These isotropic  
 625 particles can then become unstable to wave growth and generate waves in order to  
 626 reach equilibrium.

627 Wave Resonance Heating

628 Another mechanism that heats particles is due to particles resonating with  
 629 plasma waves. A few of the electromagnetic wave modes responsible for particle  
 630 acceleration (and deceleration) relevant to radiation belt dynamics are hiss, whistler  
 631 mode chorus (chorus), and electromagnetic ion cyclotron (EMIC) waves. These waves  
 632 are created by the loss cone instability that driven by an anisotropy of electrons  
 633 for chorus waves, and protons for EMIC waves. The level of anisotropy can be  
 634 quantified by the ratio of the perpendicular to parallel particle temperatures ( $T_\perp/T_{||}$ ).  
 635 A particle distribution is unstable when  $T_\perp/T_{||} > 1$  which facilitates wave growth.  
 636 Since electrons gyrate in a right-handed sense, the chorus waves also tend to be right  
 637 hand circularly polarized (Tsurutani and Lakhina, 1997). The same argument applies  
 638 to protons and left hand circularly polarized EMIC waves as well.

639 These circularly polarized waves can resonate with electrons and/or protons  
 640 when their combined motion results in a static  $\vec{E}$ . One example of a resonance  
 641 between a right hand circularly polarized wave and an electron is shown in Fig. 1.21  
 642 and is termed the cyclotron resonance. An electron's  $v_{||}$  and the wave's parallel wave  
 643 vector,  $k_{||}$  are in opposite directions such that the wave frequency  $\omega$  is Doppler shifted  
 644 to an integer multiple of the  $\Omega_e$  at which point the electron feels a static electric  
 645 field and is accelerated or decelerated. This acceleration happens when a resonance



$$\omega + \mathbf{k}_{\parallel} \mathbf{V}_{\parallel} = \Omega^-$$

Figure 1.11: The trajectories of an electron and a right-hand circularly polarized wave during a cyclotron resonance. The electron's  $v_{\parallel}$  and the wave's  $k_{\parallel}$  are in opposite directions such that the wave's frequency is Doppler shifted to an integer multiple of the electron cyclotron frequency. Figure from (Tsurutani and Lakhina, 1997).

646 condition is satisfied between a wave and a particle for which we will now derive an  
647 illustrative toy model.

648 Assume a uniform magnetic field  $\vec{B} = B_0 \hat{z}$  with a parallel propagating ( $k = k \hat{z}$ ),  
649 right-hand circularly polarized wave. The wave's electric field as a function of position  
650 and time can be written as

$$\vec{E} = E_0 (\cos(\omega t - kz) \hat{x} + \sin(\omega t - kz) \hat{y}) \quad (1.16)$$

which is more clearly expressed by taking the dot product to find  $\vec{E}$  in the  $\hat{\theta}$  direction

$$E_{\theta} = \vec{E} \times \hat{\theta} = E_0 \cos(\omega t - kz + \theta). \quad (1.17)$$

651 Now assume that the electron is traveling in the  $-\hat{z}$  direction with a velocity  $\vec{v} = -v_0 \hat{z}$   
652 so its time dependent position along  $\hat{z}$  is

$$z(t) = -v_0 t \quad (1.18)$$

653 and gyrophase is

$$\theta(t) = -\Omega t + \theta(0) \quad (1.19)$$

654 where the first negative sign comes from the electron's negative charge. Now we put  
655 this all together and express the electric field and the force that the electron will  
656 experience

$$m \frac{dv_\theta}{dt} = qE_\theta = qE_0 \sin((\omega + kv_0 - \Omega)t + \theta(0)). \quad (1.20)$$

657 This is a relatively complex expression, but when the time dependent component,

$$\omega + kv_0 - \Omega = 0, \quad (1.21)$$

658 the electron will be in a static electric field which will accelerate or decelerate the  
659 electron depending on  $\theta_0$ , the phase between the wave and the electron. **Show Bortnik**  
660 **2008 plot?** The expression in Eq. 1.21 is commonly referred to as the resonance  
661 condition and is more generally written as

$$\omega - k_{||}v_{||} = \frac{n\Omega_e}{\gamma} \quad (1.22)$$

662 where  $n$  is the resonance order, and  $\gamma$  is the relativistic correction (e.g. Millan and  
663 Thorne, 2007). In the case of the cyclotron resonance,  $\omega \approx \Omega_e$  thus  $J_1$  is violated.  
664 Since  $J_1$  is violated,  $J_2$  and  $J_3$  are also violated since the conditions required to  
665 violate  $J_2$  and  $J_3$  are less stringent than  $J_1$ . It is important to remember that along  
666 the particle's orbit it will encounter and experience the effects of many waves along  
667 its orbit. The typical MLT extent of a handful of waves that are capable of resonating  
668 with radiation belt electrons are shown in Fig. 1.12.

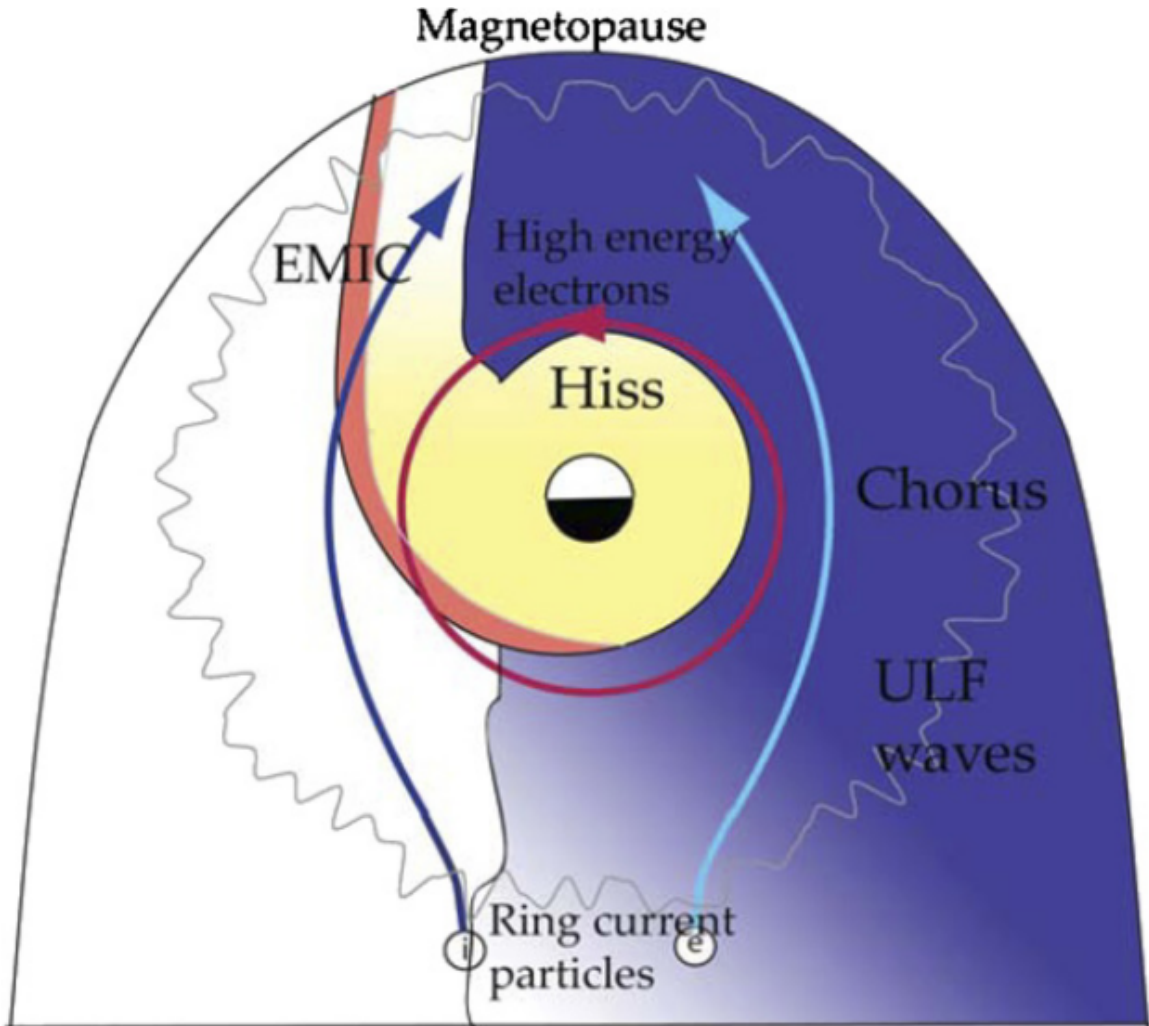


Figure 1.12: Various wave modes in the magnetosphere. Ultra low frequency waves occur through the magnetosphere. Chorus waves are typically observed in the 0-12 midnight-dawn region. EMIC waves are typically observed in the dusk MLT sector. Hiss waves are observed inside the plasmasphere. Figure from Millan and Thorne (2007).

669 Particle Losses

670 Now that we have seen two general mechanisms with which particles are  
671 accelerated and transported in the magnetosphere, we will now consider a few  
672 specific mechanisms with which particles are lost to the atmosphere or the solar  
673 wind. One particle loss mechanism into the solar wind is magnetopause shadowing  
674 (e.g. Ukhorskiy et al., 2006). Particles are sometimes lost when the ring current is  
675 strengthened and Earth's magnetic field strength is increased outside of the ring  
676 current (and reduced on Earth's surface). If the time scale of the ring current  
677 strengthening is slower than a particle drift,  $J_3$  is conserved. Then in order to  
678 conserve  $J_3$  while the magnetic field strength is increased, the particle's drift shell  
679 must move outward to conserve the magnetic flux contained by the drift shell. Then  
680 if the particle's drift shell expands to the point that it crosses the magnetopause, the  
681 particle will be lost to the solar wind.

682 **Move to acceleration?** Another particle loss and acceleration mechanism is driven  
683 by ultra low frequency (ULF) waves and is called radial diffusion. Radial diffusion is  
684 the transport of particles from high to low phase space density,  $f$ . If the transport is  
685 radially inward, particles will appear to be accelerated. On the other hand, radially  
686 outward radial diffusion can transport particles through the magnetopause where  
687 they will be lost to the solar wind. Reeves et al. (2013) investigated the driver of  
688 particle acceleration during the October 2012 storm and observationally found that  
689 inward radial diffusion was not dominant, rather local acceleration via wave-resonance  
690 heating (i.e. particle diffusion in pitch angle and energy which will be described below)  
691 appeared to be the dominant acceleration mechanism.

692 The loss mechanism central to this dissertation is pitch angle and energy  
693 scattering of electrons by waves. Some of the waves that scatter electrons in energy  
694 and pitch angle in the inner magnetosphere are: plasmaspheric hiss (e.g. Breneman

et al., 2015; O'Brien et al., 2014), EMIC waves (e.g. Capannolo et al., 2019; Hendry et al., 2017), and chorus waves (e.g. Breneman et al., 2017; Kasahara et al., 2018; Ozaki et al., 2019). These wave-particle interactions occur when the resonance condition in Eq. 1.22 is satisfied at which point the particle's energy and  $\alpha$  is modified by the wave. More details regarding the theory of pitch angle and energy diffusion is given in Chapter X. If the wave changes  $\alpha$  towards 0 such that  $\alpha < \alpha_{LC}$ , the particle's mirror point lowers to less than 100 km altitude where the particle can be lost due to collisions with air. One manifestation of pitch angle scattering of particles into the loss cone are microbursts: a sub-second durtaison impulse of electrons.

704

### Microbursts

Microbursts were first identified in high altitude balloon observations of bremsstrahlung X-rays emitted by microburst electrons impacting the atmosphere by Anderson and Milton (1964). Since then, other balloons have observed microburst X-ray signatures in the upper atmosphere (e.g. Anderson et al., 2017; Barcus et al., 1966; Parks, 1967; Trefall et al., 1966; Woodger et al., 2015; ?). In addition to their X-ray signature, microbursts electrons have been directly observed in LEO with spacecraft including the Solar Anomalous and Magnetospheric Particle Explorer (SAMPEX), Focused Investigation of Relativistic Electron Bursts: Intensity, Range, and Dynamics II (FIREBIRD-II), Science Technologies Satellite (STSAT-I) (e.g. Blake et al., 1996; Blum et al., 2015; Breneman et al., 2017; Crew et al., 2016; Lee et al., 2012, 2005; Lorentzen et al., 2001a,b; Nakamura et al., 1995, 2000; O'Brien et al., 2004, 2003). An example microburst time series is shown in Fig. 1.13 and was observed by Montana State University's (MSU) FIREBIRD-II CubeSats. The prominent features of microbursts in Fig. 1.13 are their  $\pm 1$  second duration, half order of magnitude increase in count rate above the falling background, and their approximately 200-800

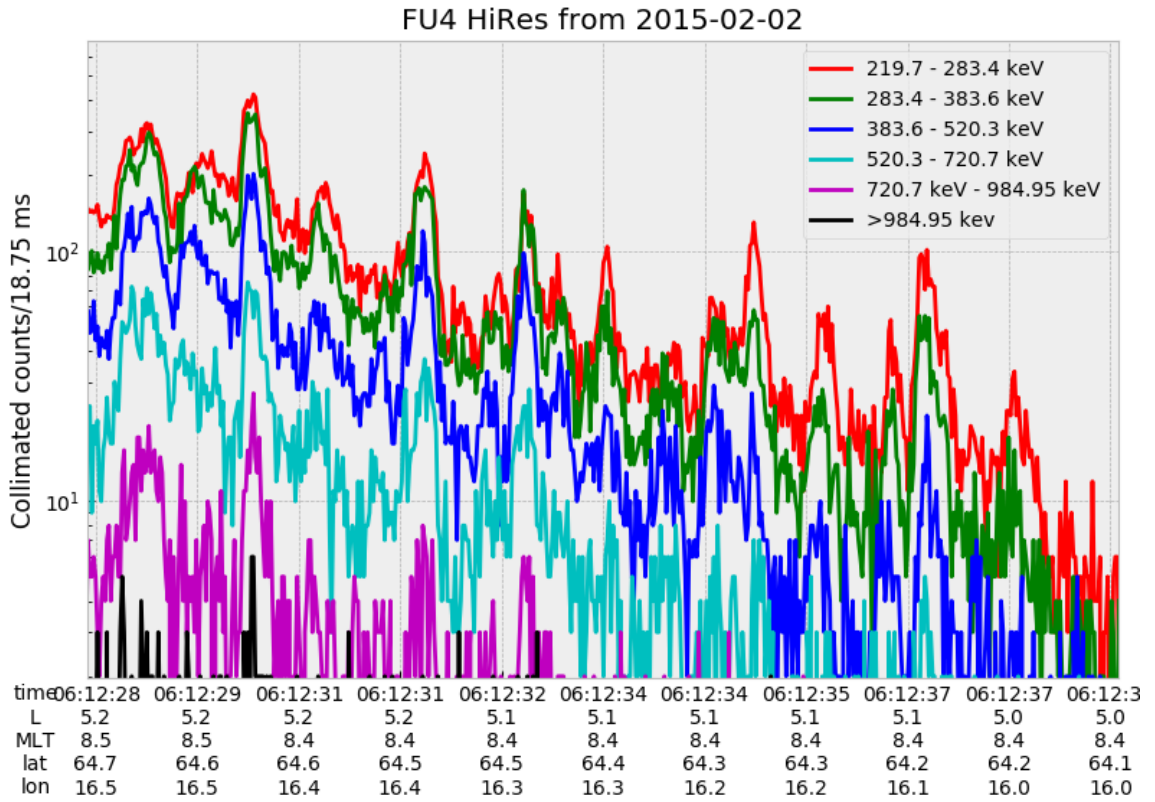


Figure 1.13: An example train of microbursts observed by FIREBIRD-II unit 4 on February 2nd, 2015. The colored curves show the differential energy channel count rates in six channels from  $\approx 200$  keV to greater than 1 MeV. The x-axis labels show auxiliary information such as time of observation and the spacecraft position in L, MLT, latitude and longitude coordinates.

<sub>720</sub> keV energy extent.

<sub>721</sub> Microbursts are observed on magnetic field footprints that are connected to the  
<sub>722</sub> outer radiation belt (approximately  $4 < L < 8$ ), and are predominately observed in  
<sub>723</sub> the 0-12 MLT sector with an elevated occurrence frequency during magnetospherically  
<sub>724</sub> disturbed times as shown in Fig. 1.14. Microbursts have been previously observed  
<sub>725</sub> over a wide energy range from a few tens of keV (Datta et al., 1997; Parks, 1967) to  
<sub>726</sub> greater than 1 MeV (e.g. Blake et al., 1996; Greeley et al., 2019). The microburst

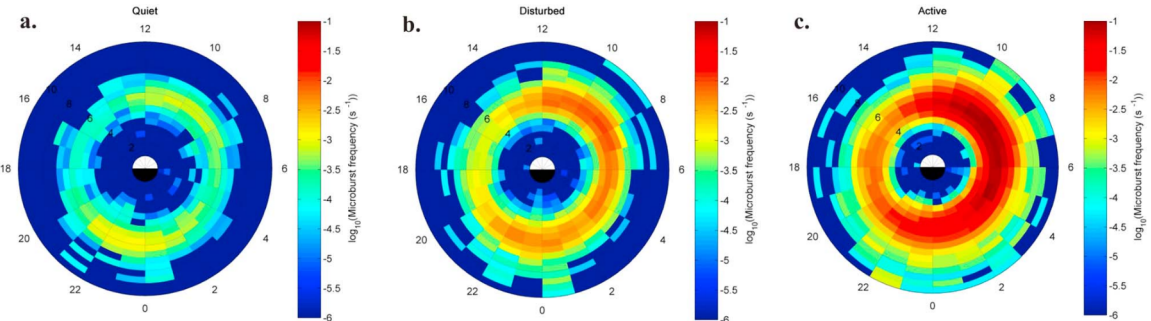


Figure 1.14: Relativistic ( $> 1\text{MeV}$ ) distribution of microburst occurrence rates as a function of  $L$  and MLT. The three panels show the microburst occurrence rate dependence on geomagnetic activity, parameterized by the auroral electrojet (AE) index for (a)  $\text{AE} < 100 \text{ nT}$ , (b)  $100 < \text{AE} < 300 \text{ nT}$  and (c)  $\text{AE} > 300 \text{ nT}$ . Figure from Douma et al. (2017).

727 electron flux ( $J$ ) falls off in energy, and the microburst energy spectra is typically  
 728 well fit to a decaying exponential

$$J(E) = J_0 e^{-E/E_0} \quad (1.23)$$

729 where  $J_0$  is the flux at 0 keV (unphysical free parameter) and  $E_0$  quantifies the  
 730 efficiency of the scattering mechanism in energy (.e.g Datta et al., 1997; Lee et al.,  
 731 2005; Parks, 1967). A small  $E_0$  suggests that mostly low energy particles are scattered  
 732 and a high  $E_0$  suggests that the scattering mechanism scatters low and high energy  
 733 electrons. Reality is a bit more messy and a high  $E_0$  may be a signature of a scattering  
 734 mechanism preferential to high energy electrons, but is hidden by the convolution of  
 735 the source particles available to be scattered (typically with a falling energy spectrum)  
 736 and the energy-dependent scattering efficiency.

737 The short duration of microbursts observed by a single LEO satellite has an  
 738 ambiguity when interpreting what is exactly a microburst. The two possible realities  
 739 are: a microburst is very small and spatially stationary so that the LEO spacecraft

740 passes through it in less than a second. Alternatively, microbursts are spatially large  
 741 with a short duration such that the microburst passes by the spacecraft in a fraction  
 742 of a second. There are a few ways to distinguish between the two possible realities,  
 743 and each one has a unique set of advantages.

744 A high altitude balloon provides essentially a stationary view of the precipitating  
 745 particles under the radiation belt footprints so a short-lived, temporal microburst  
 746 can be unambiguously identified. Spatial structures on the other hand are difficult  
 747 to identify because a balloon is essentially still on drift timescales thus a variation in  
 748 the X-rays can be due to the spatial structure or an increase of precipitating particles  
 749 over the whole area. Furthermore, if the stationary structure is drifting its particles  
 750 are not precipitating into the atmosphere so there is no X-ray signature.

751 Another solution is multi-spacecraft missions that can determine if a microburst  
 752 is spatial or temporal. As will be shown in this dissertation, if a microburst is  
 753 observed simultaneously by two spacecraft then it is temporally transient and has  
 754 a size greater than the spacecraft separation. On the other hand, if two spacecraft  
 755 observe a microburst-like feature in the same location and at different times, then it is  
 756 spatial may be a curtain (Blake and O'Brien, 2016). Both observational methods have  
 757 a unique set of strengths, and this dissertation takes the multi-spacecraft approach  
 758 to identify and study microbursts.

759

### Scope of Research

760 This dissertation furthers our understanding of the microburst scattering  
 761 mechanism by observing the scattering directly, and measuring the microburst sizes  
 762 and comparing them to the size of waves near the magnetic equator where those  
 763 electrons could have been scattered. Chapter X describes a microburst scattering  
 764 event observed by NASA's Van Allen Probes which was studied in the theoretic

765 framework of pitch angle and energy diffusion. The following two chapters will then  
766 study the size of microbursts. Chapter Y describes a bouncing packet microburst  
767 observation made by MSU's FIREBIRD-II mission where the microburst's lower  
768 bound longitudinal and latitudinal sizes were estimated. Then Chapter Z expands  
769 the case study from Ch. Y to a statistical study of microburst sizes using The  
770 Aerospace Corporation's AeroCube-6 (AC6) CubeSats. In this study, a Monte Carlo  
771 and analytic microburst size models were developed to account for the compounding  
772 effects of random microburst sizes and locations. Lastly, Ch. A will summarize the  
773 dissertation work and make concluding remarks regarding outstanding questions in  
774 microburst physics.

775

## CHAPTER TWO

776

EVIDENCE OF MICROBURSTS OBSERVED NEAR THE EQUATORIAL

777

PLANE IN THE OUTER VAN ALLEN RADIATION BELT

778

Contribution of Authors and Co-Authors

779 Manuscript(s) in Chapter(s) 1

780

781 Author: [type author name here]

782 Contributions: [list contributions here, single-spaced]

783 Co-Author: [type co-author name here]

784 Contributions: [list contributions here, single-spaced]

785 Co-Author: [type co-author name here]

786 Contributions: [list contributions here, single-spaced]

787

788

Manuscript Information

789 [Type Author and Co-author(s) Names Here]

790 Geophysical Research Letters

791 Status of Manuscript: Published in a peer-reviewed journal

792 Wiley

793 Volume 45, Issue 16

794

Key Points

795

- First report of direct observation of microbursts at high altitude, near the equatorial plane.
- Microbursts' duration, flux enhancement, and energy spectra are similar to prior observations in LEO.
- Microburst generation is not consistent with a single quasi-linear gyroresonant interaction with chorus waves.

801

Abstract

802

We present the first evidence of electron microbursts observed near the equatorial plane in Earth's outer radiation belt. We observed the microbursts on March 31st, 2017 with the Magnetic Electron Ion Spectrometer and RBSP Ion Composition Experiment on the Van Allen Probes. Microburst electrons with kinetic energies of 29-92 keV were scattered over a substantial range of pitch angles, and over time intervals of 150-500 ms. Furthermore, the microbursts arrived without dispersion in energy, indicating that they were recently scattered near the spacecraft. We have applied the relativistic theory of wave-particle resonant diffusion to the calculated phase space density, revealing that the observed transport of microburst electrons is not consistent with the hypothesized quasi-linear approximation.

812

Introduction

813

Since the Van Allen radiation belts were discovered by Van Allen (1959) and Vernov and Chudakov (1960), decades of work has focused on understanding their origins and effects on the near-Earth space environment and ionosphere-thermosphere

system. The energy content of the outer belt is dominated by energetic electrons, with dynamics controlled by a complex interplay between various source and loss mechanisms. One important loss and acceleration mechanism is gyroresonant diffusion in energy and pitch angle (PA) due to scattering of electrons by plasma waves (e.g. Bortnik et al., 2008; Horne and Thorne, 2003; Meredith et al., 2002; Millan and Thorne, 2007; Summers et al., 1998; Thorne and Andreoli, 1981; Thorne et al., 2005; Walker, 1993).

Chorus waves are commonly associated with PA and energy diffusion. These waves are typically generated by substorm injections into the inner magnetosphere, which lead to a temperature anisotropy of the source electrons with energies up to tens of keV (e.g. Horne et al., 2003; Li et al., 2009a). Since these source electrons drift eastward, chorus is most frequently observed in the dawn sector, but it has been observed at all magnetic local times (MLT) (Li et al., 2009b). Chorus waves are believed to generate electron microburst precipitation through wave-particle interactions.

Microbursts are typically defined as an increase of electron flux in or near the atmospheric loss cone that last < 1 s (e.g. Anderson and Milton, 1964; Blake et al., 1996; Lorentzen et al., 2001a). Empirical and theoretical analyses indicate that microbursts are an important loss process since they can substantially deplete the radiation belt electrons on the order of one day (e.g. Breneman et al., 2017; Lorentzen et al., 2001b; O'Brien et al., 2004; Thorne et al., 2005). Previously, microbursts have been observed in the upper atmosphere in the form of bremsstrahlung X-rays (e.g. Anderson et al., 2017; Parks, 1967; Woodger et al., 2015) and directly in low Earth orbit (LEO) (e.g. Blake et al., 1996; Blum et al., 2015; Breneman et al., 2017; Crew et al., 2016; Lee et al., 2012, 2005; Lorentzen et al., 2001a,b; Mozer et al., 2018; Nakamura et al., 1995, 2000; O'Brien et al., 2004, 2003).

We observed for the first time, microburst-like signatures near their hypothesized origin within the heart of the outer radiation belt. The unique microburst observations we report here were possible with the Van Allen Probe-A's (RBSP-A) Magnetic Electron Ion Spectrometer's (MagEIS) fast sampling rate ( $\sim 11$  ms), and RBSP Ion Composition Experiment's (RBSPICE) PA coverage. The observed microbursts' duration, energy spectra, and energy dispersion signature were similar to microbursts previously reported from LEO. Furthermore, we simultaneously observed structureless "hiss-like" whistler mode wave power in the lower band chorus frequency range (Li et al., 2012). From previous observations in LEO (e.g. Blake et al., 1996), it is believed that microbursts result from the impulsive scattering of electrons into or near the loss cone, which is on the order of a few tens of degrees in LEO. With this assumption, high altitude microburst observations near the magnetic equator should be very difficult to make since the atmospheric loss cone there is only a few degrees wide. Thus, the loss cone is smaller than the angular resolution of most particle detectors. Even when an instrument is observing the loss cone, the instrument's field of view will include some portion of the trapped population. The trapped electron flux is typically orders of magnitude higher than that in the loss cone, so that microbursts scattered into the loss cone will be obscured. We present observational evidence that suggests that the sudden impulse of electrons studied here is consistent with the creation of microbursts. Furthermore, these microbursts were scattered over a broad PA range outside of the loss cone, though the loss cone was not directly observed by MagEIS and RBSICE.

This paper explores the properties of the observed microbursts by utilizing in-situ RBSP measurements of waves and particles. This unique high altitude point of view enables us to test whether the observed microburst scattering is consistent with a quasi-linear diffusion process. We have tested this hypothesis with in-situ electron

868 phase space density (PSD) measurements and the relativistic theory of wave-particle  
 869 resonant diffusion (Summers et al., 1998; Walker, 1993) to determine if the microburst  
 870 electrons diffused in PA and energy.

871 Spacecraft Instrumentation

872 NASA's RBSP mission (Mauk et al., 2013), launched on August 30th, 2012,  
 873 consists of a pair of identically instrumented spacecraft. Their orbit and instru-  
 874 mentation are uniquely configured to enrich our understanding of the particles and  
 875 waves in the inner magnetosphere. The RBSP spacecraft are in highly elliptical, low-  
 876 inclination orbit, with perigee of  $\sim$ 600 km and apogee of  $\sim$ 30,000 km altitude. Their  
 877 attitude is maintained by spin-stabilization with a period of  $\sim$ 11 s and the spin axis is  
 878 roughly sun-pointing. In this analysis, energetic electron measurements from MagEIS  
 879 (Blake et al., 2013) and RBSPICE (Mitchell et al., 2013) were used, complemented by  
 880 magnetic field and wave measurements from Electric and Magnetic Field Instrument  
 881 and Integrated Science (EMFISIS) (Kletzing et al., 2013).

882 We observed these microbursts with RBSP-A's MagEIS low energy instrument  
 883 (MagEIS-A) which measures 20-240 keV electrons. It has an angular acceptance  
 884 of  $3^\circ - 10^\circ$  in the spacecraft spin plane, and  $20^\circ$  perpendicular to the spin plane.  
 885 MagEIS-A has a high rate data mode which samples at 1000 angular sectors per  
 886 spacecraft spin (11 ms cadence). MagEIS low on RBSP-B on the other hand samples  
 887 at 64 angular sectors per spacecraft spin (172 ms cadence), so it was only used for  
 888 context.

889 To expand the PA coverage of MagEIS-A, we used the RBSPICE-A time-of-  
 890 flight instrument. RBSPICE-A measures electron energies in the range of 19 keV -  
 891 1 MeV with a fan of six telescopes (the sixth telescope is used only for calibration  
 892 and was excluded from this analysis). These telescopes have an overall acceptance

893 angle of  $160^\circ$  by  $12^\circ$  which allows them to simultaneously sample a substantial part  
 894 of the Pitch Angle Distribution (PAD). RBSPICE-A gathers data over 32 sectors  
 895 per spacecraft spin ( $\approx 310$  ms cadence) and each sector is divided into three sub-  
 896 sectors corresponding to three measurement modes (Manweiler and Zwiener, 2018).  
 897 At the time of the observation, the sub-sector used for electron measurements had  
 898 an accumulation time of 77 ms. We used RBSPICE-A's Electron Basic Rate (EBR)  
 899 telemetry data in this analysis which is not averaged, though it is an integral energy  
 900 channel.

901 To understand the dynamics of the local magnetic field, we used the EMFISIS  
 902 instrument. EMFISIS provides measurements of the DC magnetic field with flux gate  
 903 magnetometers. In addition, it measures electromagnetic waves from 10 Hz to 500  
 904 kHz with search coil magnetometers. The spectral matrix and burst data products  
 905 used in this analysis were from the EMFISIS waveform receiver (WFR) (10 Hz - 12  
 906 kHz) and the high frequency receiver (10 kHz - 500 kHz). Burst data were selectively  
 907 captured at a 35 kHz sample rate, and the survey mode spectral matrix data was  
 908 captured every 6s.

909

### Observations

910 MagEIS-A and RBSPICE-A observed the microburst-like signatures on March  
 911 31st, 2017 at  $L^* \approx 6$  and  $MLT \approx 19$ , calculated with the Tsyganenko 2004 magnetic  
 912 field model (Tsyganenko and Sitnov, 2005). The magnetosphere was in the recovery  
 913 phase of a storm, with minimum Dst of -75 nT observed on March 27th. The local  
 914 electron number density was on the order of  $1 \text{ cm}^{-3}$  at this time, so both RBSP  
 915 spacecraft were located outside the plasmasphere. The two spacecraft were separated  
 916 by 1700 km, at magnetic latitudes  $\lambda \approx -19^\circ$  and  $\lambda \approx -18^\circ$  for RBSP-A and RBSP-B,  
 917 respectively.

918 MagEIS-A observed microburst electron flux ( $J$ ) at energies  $\geq 92$  keV around  
 919 11:17 UT as shown in panel (a) in Fig. 4.1. For directional information, panel (b)  
 920 in Fig. 4.1 shows flux as a function of local pitch angle ( $\alpha_L$ ) and time for 46-66 keV  
 921 electrons. Electrons that traveled towards the northern hemisphere had  $\alpha_L < 90^\circ$  and  
 922 southern hemisphere had  $\alpha_L > 90^\circ$ . The interval between the two vertical dashed  
 923 black lines contain the four microbursts examined in this study. We observed these  
 924 microbursts at  $\alpha_L < 50^\circ$ , but MagEIS-A did not sample into the  $0^\circ$  loss cone.

925 Figure 4.1 panel (c) shows the EMFISIS WFR data from RBSP-A. Between  
 926 11:17:05 and 11:17:10 UT, we observed an isolated burst of whistler mode wave power  
 927 in the frequency range  $0.1 < \omega < 0.3 \Omega_{ce0}$ , where  $\Omega_{ce0}$  is the equatorial electron  
 928 gyrofrequency. No individual rising or falling tone elements were observed during  
 929 this period, and the waves appeared more “hiss-like” (e.g. Li et al., 2012). This wave  
 930 was near-parallel propagating (evidence shown in Appendix A) and about 10 minutes  
 931 later, weak chorus rising tone elements were observed (not shown).

932 Panels (d)-(f) in Fig. 4.1 are in the same format as panels (a)-(c), but for RBSP-  
 933 B. An injection or boundary was observed with RBSP-B at 11:16:50 UT and RBSP-A  
 934 observed a similar feature soon after 11:18 UT (not shown).

935 A zoomed-in version of Fig. 4.1 panels (a) and (b) is shown in Fig. 4.2. Panel  
 936 (a) shows the four microburst-like signatures observed between 11:17:10 and 11:17:12  
 937 UT, at energies up to 92 keV. The observed duration of the microbursts was 150  
 938 - 500 ms, and they did not arrive dispersed in energy, which indicates that they  
 939 were recently scattered near the spacecraft location. We use IRBEM-Lib, a library  
 940 dedicated to radiation belt modeling (Boscher et al., 2012), to calculate the mirror  
 941 point altitudes, which were found to be above LEO. Panel (b) shows the RBSPICE-  
 942 A EBR time series with the group of microbursts observed at the same time as  
 943 in panel (a). To understand the timing relationship between the MagEIS-A and

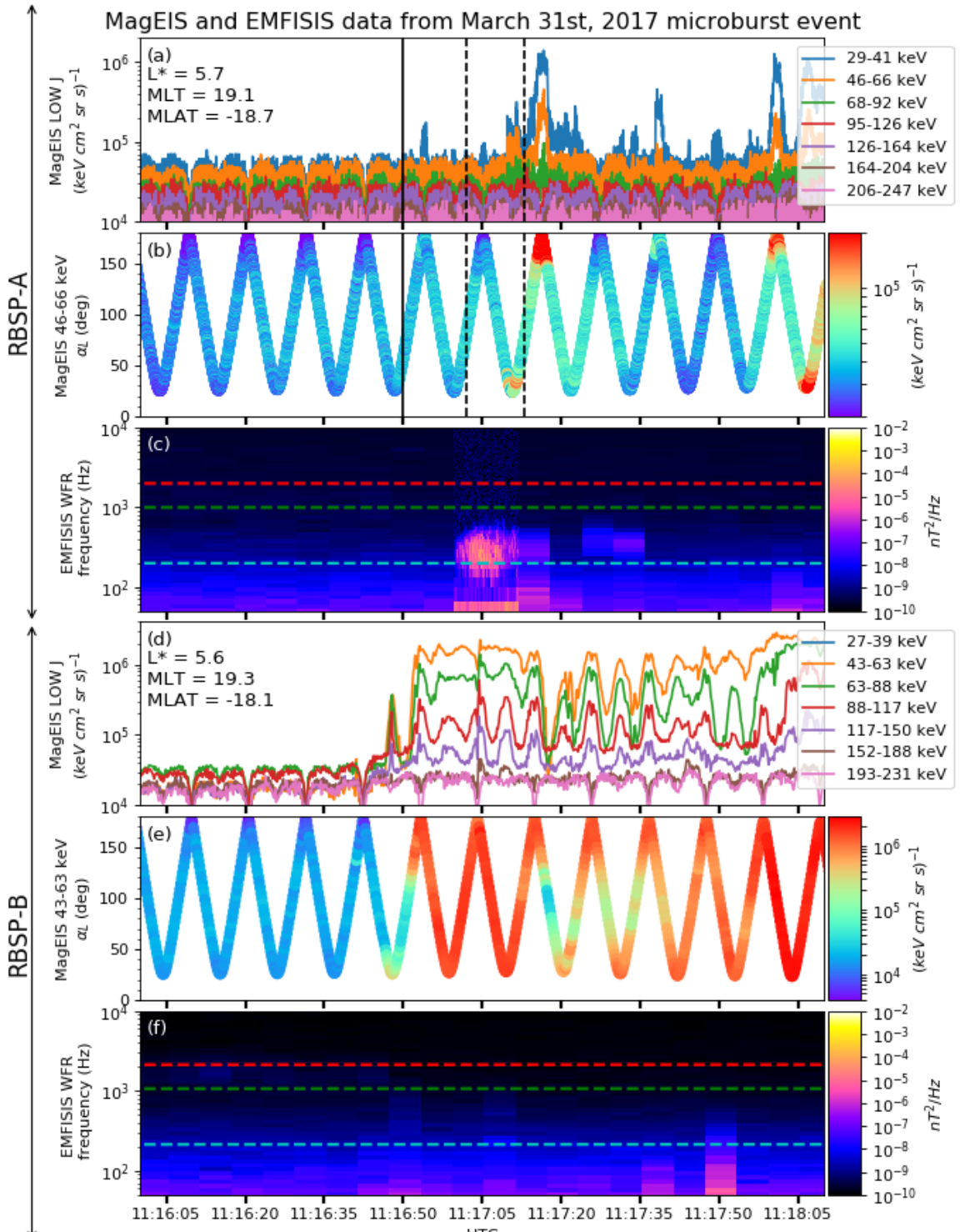


Figure 2.1: Electron and wave conditions from the MagEIS-A and EMFISIS WFR sensors for the microburst time interval. Panels (a), (b), and (c) are from RBSP-A with its position information annotated in panel (a). Panels (d), (e), and (f) are from RBSP-B with its position information annotated in panel (d). Panel (a) is the MagEIS-A high rate timeseries. Panels (b) and (e) show the evolution of the MagEIS-A  $J$  as a function of  $\alpha_L$  from the  $\sim 40$  to  $\sim 60$  keV channel. Every 10th point is shown in panel (b). The solid black line in panels (a) and (b) mark the end of the time period used for the PSD fit extrapolation analysis explained in section

944 RBSPICE-A observations, we marked the times when MagEIS-A observed the four  
 945 microbursts by vertical black arrows in panels (a) and (b). MagEIS-A observed the  
 946 first microburst  $\sim 0.5$  s before RBSPICE-A. The bounce period of locally mirroring,  
 947 100 keV electrons was  $\sim 0.8$  s, so this was unlikely to have been a returning bounce.  
 948 This evidence confirms that these microburst signatures are packets of electrons and  
 949 not a boundary moving back and forth at RBSP-A's location. To understand the  
 950 PA extent of these microbursts, panel (c) shows the 29-41 keV MagEIS-A  $J$  and  
 951 RBSPICE-A EBR as a function of  $\alpha_L$  and time. The microburst  $J$  was observed  
 952 by MagEIS-A between  $25^\circ < \alpha_L < 50^\circ$  and RBSPICE-A between  $100^\circ < \alpha_L < 160^\circ$ ,  
 953 with the highest intensities close to  $\alpha_L = 90^\circ$ . RBSPICE-A observed a 10-80%  
 954 enhancement in count rate over those PAs with the evidence presented in Appendix  
 955 A.

956

### Analysis

957 First, we estimated the microburst energy spectra. For each microburst shown in  
 958 Fig. 4.2, its flux was averaged and baseline subtracted using the method from O'Brien  
 959 et al. (2004) and then fit with an exponential function. The calculated exponential  
 960 E-folding energy was found to vary between 25 and 35 keV, which is consistent with  
 961 spectra derived from prior measurements (Datta et al., 1997; Lee et al., 2012, 2005).

962 We then tested the hypothesis that the microburst electrons were transported  
 963 in energy and PA by a single chorus wave. We used a procedure similar to sections  
 964 3.1 and 4.5 in Meredith et al. (2002) which we describe below.

965 Microburst and Source PSD

966 We estimated the electron PSD,  $f(p_\perp, p_\parallel)$  where  $p_\perp$  and  $p_\parallel$  are the perpendicular  
 967 and parallel components of the electron momentum relative to the local magnetic field,

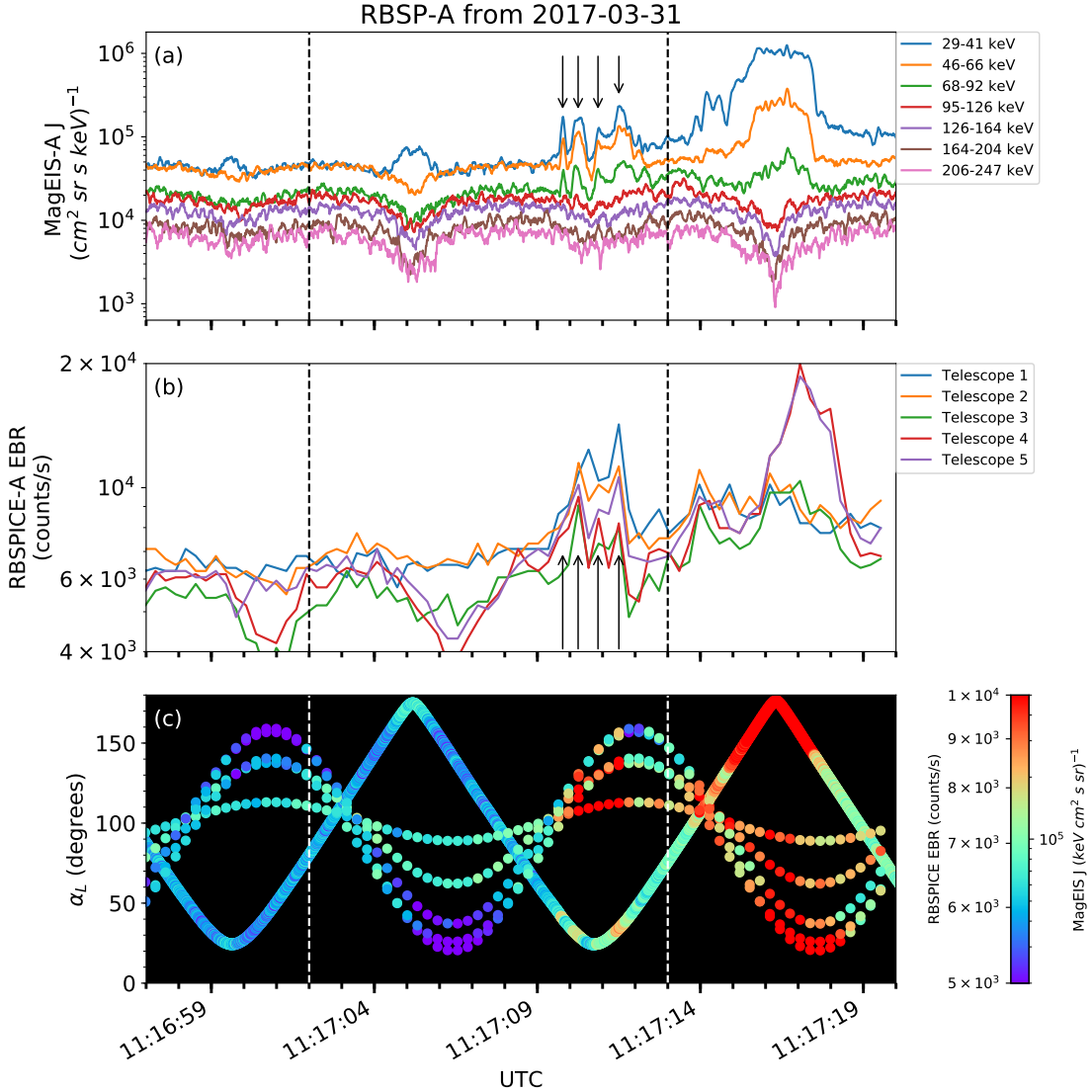


Figure 2.2: Panel (a) shows the MagEIS-A high rate timeseries. Panel (b) shows the RBSPIKE EBR count rate timeseries for  $\zeta$  19 keV electrons. The microbursts were observed between 11:17:10 - 11:17:12 UT and are indicated with the vertical black arrows in panels (a) and (b) for MagEIS-A times. Panel (c) shows the RBSPIKE EBR (family of relatively sparse sampled curves) and MagEIS-A  $J$  from the 29-41 keV energy channel (single curve) as a function of  $\alpha_L$ . The vertical dashed lines show the time interval for the PSD analysis.

for the microburst time period. MagEIS-A  $J(E, \alpha_L)$  was averaged between 11:17:02 and 11:17:13 UT and binned by  $\alpha_L$  into  $5^\circ$  bins. Then, we assumed the conservation of the first adiabatic invariant and mapped  $\alpha_L$  to equatorial PA,  $\alpha_{eq}$ . The binned  $J(E, \alpha_{eq})$  was then converted to  $f(p_\perp, p_\parallel)$  via

$$f(p_\perp, p_\parallel) = \frac{J(E, \alpha_{eq})}{p^2}, \quad (2.1)$$

where  $p = \sqrt{p_\perp^2 + p_\parallel^2}$ . Lastly,  $\alpha_{eq}$  was used to separate  $p$  into  $p_\perp$  and  $p_\parallel$  via

$$\frac{p_\parallel}{m_e c} = \frac{\sqrt{E(E + 2E_0)} \cos(\alpha_{eq})}{E_0} \quad (2.2)$$

$$\frac{p_\perp}{m_e c} = \frac{\sqrt{E(E + 2E_0)} \sin(\alpha_{eq})}{E_0} \quad (2.3)$$

where  $c$  is the speed of light,  $E$  is the kinetic energy,  $m_e$  is the electron mass, and  $E_0$  is the electron rest energy. The observed  $f(p_\perp, p_\parallel)$  in dimensionless momentum space is shown in Fig. 4.3 in all panels between the  $p_\parallel$  axis and the white dotted lines. The bright spot in  $f(p_\perp, p_\parallel)$  in the upper  $p_\parallel$  plane represents the four microbursts. Along with the observed PSD, we use Fig. 4.3 to explore the various PSD extrapolation and diffusion model assumptions which are described below.

We proceed under the assumption that the source of the microburst electrons is not likely to be at the latitude of the observation, and is closer to the magnetic equator. To look for a source of microburst electrons, we extrapolate the unobserved  $f(p_\perp, p_\parallel)$  of electrons with  $|\lambda_m| < 19^\circ$  using two cases with a  $90^\circ$ -peaked PAD of the form

$$f(E, \alpha_{eq}) = f_0(E) \sin^n(\alpha_{eq}) \quad (2.4)$$

where  $f_0(E)$  is a scaling parameter and  $n$  is a power parameter. Similarly to the

980 in-situ  $f(p_{\perp}, p_{\parallel})$ , the  $f(E, \alpha_{eq}) \mapsto f(p_{\perp}, p_{\parallel})$  conversion was applied.

981 In the first case, we fitted Eq. 2.4 to the quiet time  $J(E, \alpha_{eq})$  from 11:15:00 to  
 982 11:16:50 UT (end time shown as the black vertical line in Fig. 4.1). The fitted  
 983 PAD was relatively flat with  $0.4 < n < 0.5$  and highest magnitude of  $f_0$  was  
 984  $0.05 c^3/(cm MeV)^3$ . This extrapolated  $f(p_{\perp}, p_{\parallel})$  is shown in Fig. 4.3 panels (A) and  
 985 (E), between the dotted white lines for scattering at  $\lambda = 0^\circ$  and  $20^\circ$ , respectively.  
 986 To confirm the relatively low  $n$  parameter, we found times where RBSP-A was in  
 987 a similar L-MLT location, but closer to the magnetic equator. At 2 and 19 UT on  
 988 the same day, we fit the  $J(E, \alpha_{eq})$ , and the fit parameters were very similar to the  
 989 pre-microburst  $f(p_{\perp}, p_{\parallel})$  at 11 UT. Thus it is a reasonable assumption that  $f(p_{\perp}, p_{\parallel})$   
 990 was relatively flat near the equator.

991 In the other case, we estimate how large  $n$  would have to be in order to find  
 992 sufficient PSD in MagEIS-A's energy range to be a source of the microburst electrons.  
 993 We used  $n \in \{1, 2, 4\}$  and we forced the  $f_0(E)$  parameter to match the observed  
 994  $f(p_{\perp}, p_{\parallel})$  at the most equatorial PAs observed by MagEIS-A. These extrapolations  
 995 are shown in columns 2-4 in Fig. 4.3. There was enough source PSD anywhere in  
 996 MagEIS-A's energy range only if  $n \geq 2$ .

997 Motion of resonant electrons in phase space

To calculate the motion of resonant electrons in momentum space, we used the relativistic theory of wave-particle resonant diffusion developed by Walker (1993) and Summers et al. (1998) and applied in Meredith et al. (2002). The chorus wave can modify  $f(p_{\perp}, p_{\parallel})$  when a resonance condition is satisfied. The cyclotron resonance condition between an electron with velocity  $v = \sqrt{v_{\parallel}^2 + v_{\perp}^2}$  and a parallel propagating

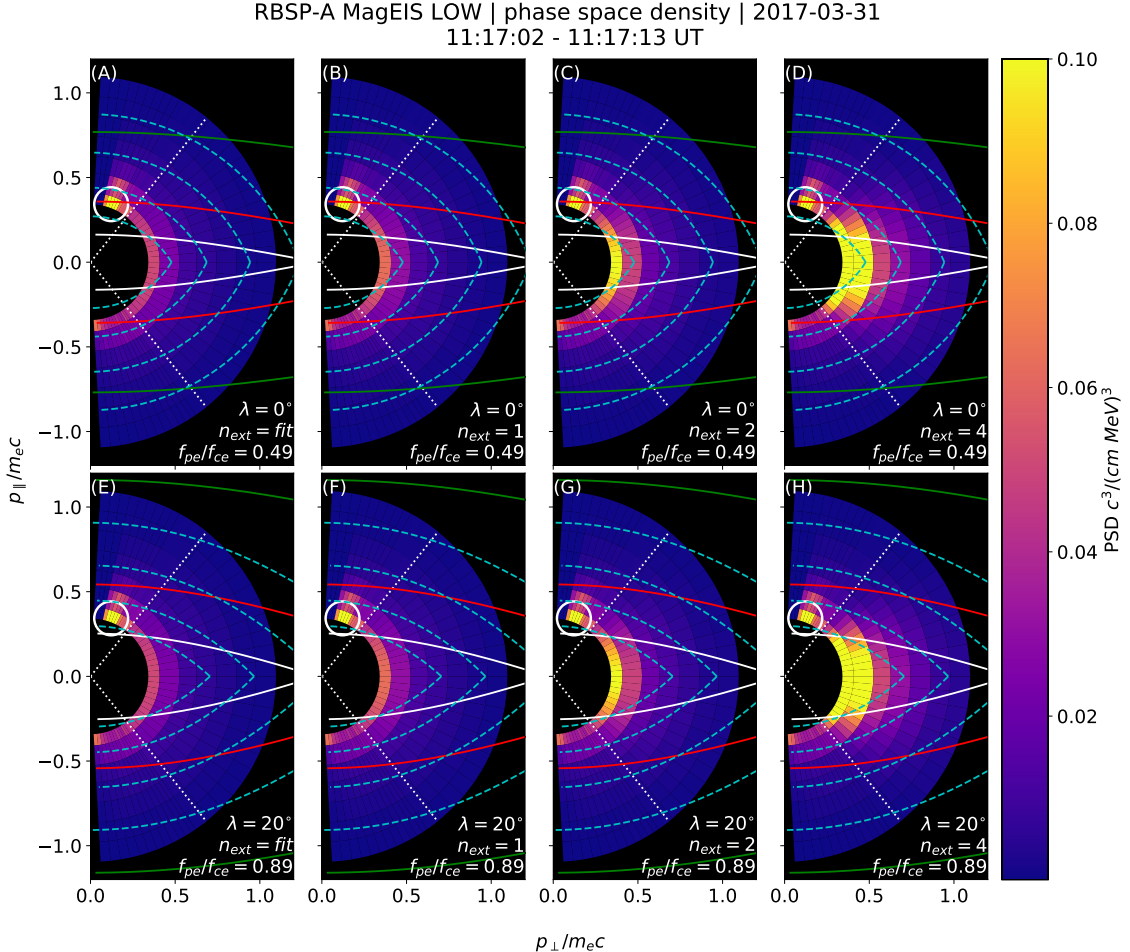


Figure 2.3: The colored annulus represents  $f(p_{\perp}, p_{\parallel})$  in normalized momentum space, parallel and perpendicular to the background magnetic field. The microburst  $f(p_{\perp}, p_{\parallel})$  is highlighted with the white circle. The columns show different powers of the sine extrapolation, and rows show the different magnetic latitudes of the scattering. The white dotted traces represent the boundary between the data and extrapolation. The green, red, and white solid traces are the resonance curves for  $\omega = 0.2\Omega_{ce}$ ,  $0.4\Omega_{ce}$ ,  $0.6\Omega_{ce}$ , respectively. The cyan dashed traces are the diffusion curves for a  $\omega = 0.4\Omega_{ce}$  wave (waves of other frequency have similar diffusion curves). The magnetic latitude of the scattering, the ratio of the plasma to the cyclotron frequency, and the power of the sine extrapolation is annotated in each panel. For the resonance and diffusion curves, the density model assumed a  $n_L = 1 e^-/cm^3$  and  $\psi = -1$ .

wave of frequency  $\omega$  and wave number  $k_{\parallel}$  is given by

$$\omega - v_{\parallel} k_{\parallel} = \frac{\Omega_{ce}}{\gamma}, \quad (2.5)$$

where  $\Omega_{ce}$  is the electron gyrofrequency at the scattering location, and  $\gamma$  is the relativistic correction. Assuming the cold plasma approximation,

$$k_{\parallel} = \frac{\omega}{c} \sqrt{1 - \frac{\omega_{pe}^2}{\omega(\omega - |\Omega_{ce}|)}}, \quad (2.6)$$

where  $\omega_{pe}$  is the plasma frequency. For a particular set of parameters, Eq. 2.5 defines a curve in momentum space that describes which electrons will resonate with a monochromatic wave.

To calculate  $k_{\parallel}$ , we approximated the electron number density,  $n_e(\lambda)$  locally and at the magnetic equator. Locally, the plasma density was approximately  $n_e(\lambda = -20^\circ) = n_L \approx 1 \text{ cm}^{-3}$ . We used magnetospheric seismology techniques (e.g. Takahashi and Denton, 2007) to parameterize  $n_e(\lambda)$  elsewhere along the field line with

$$n_e(\lambda) = n_e(0) \left( \frac{LR_e}{R(\lambda)} \right)^{\psi} \quad (2.7)$$

where  $R_e$  is the Earth's radius,  $R(\lambda)$  is the radial distance from the Earth to the spacecraft, and  $\psi$  is the exponent parameter. Assuming a dipole magnetic field for which  $R(\lambda) = LR_e \cos^2 \lambda$  (e.g. Schulz and Lanzerotti, 1974), we can express Eq. 2.7 in terms of  $n_L$  via

$$n_e(\lambda) = n_L \left( \frac{\cos \lambda_L}{\cos \lambda} \right)^{2\psi} \quad (2.8)$$

where we used  $\psi = -1$  (higher density at the magnetic equator) in this analysis. We chose this exponent parameter because it is a realistic best case scenario for the

1008 electrons to be transported along the diffusion curves (described below).

Walker (1993) and Summers et al. (1998) argued that a resonant electron will move along diffusion curves in momentum space. A diffusion curve is derived as follows. In the reference frame moving with a monochromatic chorus wave's phase velocity (wave frame), the chorus wave is stationary and there is no electric field. Thus in the wave frame, the electron's kinetic energy is conserved, and the electron's velocity in the wave frame can be expressed in differential form as

$$v_{\parallel}dv_{\parallel} + v_{\perp}dv_{\perp} = 0. \quad (2.9)$$

After a Lorentz transformation of Eq. 2.9 into the magnetospheric frame, kinetic energy will no longer be conserved. After integration and manipulation of Eq. 2.9, we obtain:

$$\left(1 - \frac{u_0^2 v_0^2}{c^4}\right)v_{\parallel}^2 - 2u_0\left(1 - \frac{v_0^2}{c^2}\right)v_{\parallel} + \left(1 - \frac{u_0^2}{c^2}\right)v_{\perp}^2 = v_0^2 - u_0^2 \quad (2.10)$$

1009 where  $u_0 = \omega/k_{\parallel}$  is the phase velocity, and  $v_0$  is a constant of integration (Summers  
 1010 et al., 1998; Walker, 1993). Equation 2.10 defines a family of diffusion curves in  
 1011 momentum space on which resonant electrons will move. The distance that an  
 1012 electron moves along a diffusion curve is a function of wave and plasma parameters,  
 1013 and is estimated from the magnitude of the diffusion coefficients and the resonance  
 1014 time.

1015 Comparing the microburst PSD to diffusion theory

1016 Superposed on the PSD plots in Fig. 4.3 are resonance curves for chorus waves  
 1017 of  $\omega = 0.2\Omega_{ce}$ ,  $0.4\Omega_{ce}$ ,  $0.6\Omega_{ce}$  and a few diffusion curves for a  $\omega = 0.4\Omega_{ce}$  wave.  
 1018 These curves were parameterized by  $\lambda$  using a dipole magnetic field for  $\lambda = 0^\circ$

(Fig. 4.3, panels A-D) and  $\lambda = 20^\circ$  (Fig. 4.3, panels E-H). If the transport of microburst electrons is consistent with gyro-resonant diffusion, a diffusion curve that passes through the microburst  $f(p_\perp, p_\parallel)$  must also pass through another region with at least the same magnitude PSD ( $f(p_\perp, p_\parallel) \geq 0.1 \text{ c}^3/(\text{cm MeV})^3$ ) e.g. Fig. 4.3, panel (D). With this constraint, an artificially high extrapolated  $f(p_\perp, p_\parallel)$  with  $n > 2$  (5 times larger than calculated from the fits) must be assumed for there to have been a sufficient source of PSD anywhere in MagEIS-A's energy range.

We now show that by comparing MagEIS observations with theory, that the minimum wave amplitude necessary to scatter these electrons is much higher than was observed by EMFISIS-A. If we assume a unrealistic PAD with enough PSD just equatorward of RBSP-A, we can use MagEIS-A observations to calculate the minimum  $\Delta\alpha_{eq}$  that the electrons were transported. We then used diffusion theory to calculate the necessary wave amplitude. For microbursts with larger PAs, MagEIS-A observed a transport of  $\Delta\alpha_{eq} = 9^\circ$  and for microbursts with smaller PAs, the observed transport was  $\Delta\alpha_{eq} = 24^\circ$ . The required wave amplitude was calculated with Eq. 3 from Thorne and Andreoli (1981) assuming a maximum resonance period of a quarter bounce. The observed change in PA requires a wave amplitude  $0.2 < |B_w| < 0.5 \text{ nT}$ . For a few brief moments, the EMFISIS-A WFR waveform data showed  $0.1 < |B_w| < 0.15 \text{ nT}$ , so a transport of  $9^\circ$  is plausible, but not likely for  $24^\circ$ .

Another source of microburst electrons may be from energies below MagEIS-A's range. The Helium, Oxygen, Proton, and Electron mass spectrometer (Funsten et al., 2013) on RBSP-A observed  $f(p_\perp, p_\parallel) \geq 0.1 \text{ c}^3/(\text{cm MeV})^3$  for  $\gtrsim 23 \text{ keV}$  electrons at this time. We then assumed the wave amplitude derived above to predict the transport in energy. We used the fact that the momentum and pitch angle diffusion coefficients,  $D_{pp}$  and  $D_{\alpha\alpha}$  are related via  $D_{pp}/p^2 \sim D_{\alpha\alpha}$  or equivalently,  $\Delta p/p \sim \Delta\alpha$ . The observed PA transport corresponds to an energy transport of  $6 < \Delta E < 16$

1045 keV. Therefore, this wave can transport 23 keV electrons from smaller pitch angles  
 1046 to larger pitch angles and would be observed in the 29 – 41 keV MagEIS-A channel.  
 1047 However, this wave is insufficient to transport electrons to the 68 – 92 keV channel  
 1048 in one interaction. Therefore we conclude that quasi-linear diffusion cannot explain  
 1049 the observed microbursts.

1050

### Discussion and Conclusions

1051 These novel observations of impulsive electron signatures reported here fall  
 1052 well within the broad definition of a microburst as described in section 3. Their  
 1053 properties were similar to microbursts observed in LEO, with an E-folding energy of  
 1054  $25 < E_0 < 35$  keV (Datta et al., 1997; Lee et al., 2012, 2005), duration of 150-500  
 1055 ms (Lorentzen et al., 2001a), observed upper energy limit of 92 keV, and a lack of  
 1056 clear energy dispersion (Breneman et al., 2017). With MagEIS-A’s high time and  
 1057 energy resolution, we conclude that these dispersionless microbursts were recently  
 1058 scattered near the spacecraft. Furthermore, RBSPICE-A’s PA coverage suggests  
 1059 that these electrons were scattered over a substantial range of PAs, with the highest  
 1060 intensities near  $\alpha_L = 90^\circ$ . Overall, our observational evidence suggests that on time  
 1061 scales shorter than one bounce period, the chorus wave effectively accelerated trapped  
 1062 electrons over a broad PA range.

1063 In the theoretical framework of wave-particle resonant diffusion applied to the  
 1064 observed PSD in section 3, we determine that the observed scattering is not consistent  
 1065 with the quasi-linear approximation. The nearest source of sufficient PSD is too  
 1066 far away in phase space to have been transported by the hypothesized quasi-linear  
 1067 process over a timescale shorter than one bounce period (one interaction). A similar  
 1068 conclusion was made by Mozer et al. (2018) who used quasi-linear theory constrained  
 1069 by RBSP wave measurements. They successfully modeled the one second average

1070 precipitating flux observed with AeroCube-6 (AC-6) CubeSats during a conjunction,  
 1071 but they were unable to model the AC-6 fluxes on smaller time scales.

1072 To put these microburst observations into a wider magnetospheric perspective,  
 1073 we observed them during the recovery phase of a minimum Dst of -75 nT storm, a  
 1074 statistically favorable time period for microbursts (O'Brien et al., 2003). Furthermore,  
 1075 during the same storm on March 27th, the Arase spacecraft observed highly correlated  
 1076 lower band chorus with 10-50 keV electron precipitation inside the loss cone. At  
 1077 that time, Arase's magnetic field footprint was near The Pas All-Sky Imager (part  
 1078 of the THEMIS mission) which simultaneously observed pulsating auroral patches  
 1079 (Kasahara et al., 2018). While microbursts and pulsating auroral patches have not  
 1080 been clearly connected, they are both believed to be a product of electron scattering  
 1081 by whistler mode waves (e.g. Lorentzen et al., 2001a; Nishimura et al., 2011; O'Brien  
 1082 et al., 2003; Ozaki et al., 2012).

1083 The combined capabilities of the various RBSP wave and particle instruments  
 1084 enable comprehensive studies of wave-particle scattering and the resulting microburst  
 1085 precipitation. From a preliminary search by the authors, other microburst-like  
 1086 signatures have been found with RBSP. Similar to previous studies (e.g. Blum et al.,  
 1087 2015; O'Brien et al., 2003), a statistical study of high-altitude microbursts in L-MLT  
 1088 space needs to be conducted before we can verify that these microbursts are the  
 1089 counterpart of the microbursts observed in LEO and the upper atmosphere.

1090

### Acknowledgments

1091 The authors acknowledge the technicians, engineers, and scientists who made the  
 1092 RBSP and AC-6 missions possible. One author (Shumko) would like to acknowledge  
 1093 Dana Longcope for his help in understanding the quasi-linear diffusion theory. Dr.  
 1094 Gkioulidou was supported by JHU/APL subcontract 131803 to the NJIT under NASA

1095 Prime contract NNN06AA01C. EMFISIS work was supported by JHU/APL contract  
1096 no. 921647 under NASA Prime contract No. NAS5-01072. The MagEIS instrument  
1097 was funded by NASA's Prime contract no. NAS5-01072. The level 3 MagEIS-A  
1098 "high rate" data is available in the Supporting Information, level 1 RBSPICE EBR  
1099 data is archived at <http://rbspicea.ftecs.com/>, and the EMFISIS level 2 spectral  
1100 matrix and burst data as well as the level 3 magnetometer data is archived at  
1101 <http://emfisis.physics.uiowa.edu/data/index>. The IRBEM Library can be obtained  
1102 at [irbem.sf.net](http://irbem.sf.net).

1103

## CHAPTER THREE

1104

MICROBURST SCALE SIZE DERIVED FROM MULTIPLE BOUNCES OF A

1105

MICROBURST SIMULTANEOUSLY OBSERVED WITH THE FIREBIRD-II

1106

CUBESATS

1107

Contribution of Authors and Co-Authors

1108

Manuscript(s) in Chapter(s) 1

1109

1110 Author: [type author name here]

1111 Contributions: [list contributions here, single-spaced]

1112 Co-Author: [type co-author name here]

1113 Contributions: [list contributions here, single-spaced]

1114 Co-Author: [type co-author name here]

1115 Contributions: [list contributions here, single-spaced]

1116

1117

Manuscript Information

1118 [Type Author and Co-author(s) Names Here]

1119 Geophysical Research Letters

1120 Status of Manuscript: Published in a peer-reviewed journal

1121 Wiley

1122 Volume 45, Issue 17

1123

1124 This article is available under the terms of the Creative Commons Attribution  
1125 Non-Commercial No Derivatives License CC BY-NC-ND (which may be updated  
1126 from time to time) and permits non-commercial use, distribution, and reproduction  
1127 in any medium, without alteration, provided the original work is properly cited and  
1128 it is reproduced verbatim.

1129

Key Points

1130

- Multiple bounces from a microburst were observed by the two FIREBIRD-II CubeSats at LEO.
- The lower bounds on the microburst scale size at LEO were  $29 \pm 1$  km (latitudinal) and  $51 \pm 11$  km (longitudinal).
- Deduced lower bound equatorial scale size was similar to the whistler-mode chorus source scale.

1136

Abstract

1137

We present the observation of a spatially large microburst with multiple bounces made simultaneously by the FIREBIRD-II CubeSats on February 2nd, 2015. This is the first observation of a microburst with a subsequent decay made by two co-orbiting but spatially separated spacecraft. From these unique measurements, we place estimates on the lower bounds of the spatial scales as well as quantify the electron bounce periods. The microburst's lower bound latitudinal scale size was  $29 \pm 1$  km and the longitudinal scale size was  $51 \pm 1$  km in low earth orbit. We mapped these scale sizes to the magnetic equator and found that the radial and azimuthal scale sizes were at least  $500 \pm 10$  km and  $530 \pm 10$  km, respectively. These lower bound equatorial scale sizes are similar to whistler-mode chorus wave source scale sizes, which supports the hypothesis that microbursts are a product of electron scattering by chorus waves. Lastly, we estimated the bounce periods for 200-800 keV electrons and found good agreement with four common magnetic field models.

1150

Introduction

1151       The dynamics of radiation belt electrons are complex, and are driven by  
 1152 competition between source and loss processes. A few possible loss processes are  
 1153 radial diffusion (Shprits and Thorne, 2004), magnetopause shadowing (Ukhorskiy  
 1154 et al., 2006), and pitch angle and energy diffusion due to scattering of electrons by  
 1155 plasma waves (e.g. Abel and Thorne, 1998; Horne and Thorne, 2003; Meredith et al.,  
 1156 2002; Mozer et al., 2018; Selesnick et al., 2003; Summers et al., 1998; Thorne et al.,  
 1157 2005). There are a variety of waves that cause pitch angle scattering, including  
 1158 electromagnetic ion cyclotron waves, plasmaspheric hiss, and chorus (Millan and  
 1159 Thorne, 2007; Thorne, 2010). Chorus predominantly occurs in the dawn sector (6-12  
 1160 magnetic local times (MLT)) (Li et al., 2009b) where it accelerates electrons with  
 1161 large equatorial pitch angles and scatters electrons with small equatorial pitch angles  
 1162 (Horne and Thorne, 2003). Some of these electrons may be impulsively scattered  
 1163 into the loss cone, where they result in short-duration ( $\sim 100$  ms) enhancements in  
 1164 precipitating flux called microbursts.

1165       Anderson and Milton (1964) coined the term microburst to describe high altitude  
 1166 balloon observations of  $\sim 100$  ms duration enhancements of bremsstrahlung X-  
 1167 rays emitted from scattered microburst electrons impacting the atmosphere. Since  
 1168 then, non-relativistic (less than a few hundred keV) microbursts have been routinely  
 1169 observed with other balloon missions (e.g. Anderson et al., 2017; Parks, 1967; Woodger  
 1170 et al., 2015). A review of the literature shows no reports of microbursts above a few  
 1171 hundred keV observed by balloons (Millan et al., 2002; Woodger et al., 2015). This  
 1172 lack of observation may be explained by relatively weaker pitch angle scattering of  
 1173 relativistic electrons by chorus (Lee et al., 2012).

1174       In addition to the X-ray signature for bursts of electron precipitation, the

1175 precipitating relativistic and non-relativistic electrons have been measured in situ by  
 1176 spacecraft orbiting in low earth orbit (LEO). Hereinafter, we refer to these electron  
 1177 signatures observed by LEO spacecraft also as microbursts. Microbursts have been  
 1178 observed with, e.g. the Solar Anomalous and Magnetospheric Particle Explorer's  
 1179 (SAMPEX)  $\gtrsim$  150 keV and  $\gtrsim$  1 MeV channels (Blake et al., 1996; Blum et al., 2015;  
 1180 Lorentzen et al., 2001a,b; Nakamura et al., 1995, 2000; O'Brien et al., 2004, 2003) and  
 1181 Focused Investigation of Relativistic Electron Bursts: Intensity, Range, and Dynamics  
 1182 (FIREBIRD-II) with its  $\gtrsim$  200 keV energy channels (Anderson et al., 2017; Breneman  
 1183 et al., 2017; Crew et al., 2016).

1184 Understanding microburst precipitation and its scattering mechanism is impor-  
 1185 tant to radiation belt dynamics. The scattering mechanism has been observationally  
 1186 studied by e.g. Lorentzen et al. (2001b) who found that microbursts and chorus  
 1187 waves predominantly occur in the dawn sector and Breneman et al. (2017) made  
 1188 a direct observational link between individual microbursts and chorus elements.  
 1189 Microbursts have been modeled and empirically estimated to be capable of depleting  
 1190 the relativistic electron population in the outer radiation belt on the order of a day  
 1191 (Breneman et al., 2017; O'Brien et al., 2004; Shprits et al., 2007; Thorne et al., 2005).  
 1192 An important parameter in this estimation of instantaneous radiation belt electron  
 1193 losses due to microbursts is their scale size. Parks (1967) used balloon measurements  
 1194 of bremsstrahlung X-rays to estimate the high altitude scale size of predominantly low  
 1195 energy microbursts to be  $40 \pm 14$  km. In Blake et al. (1996) a microburst with multiple  
 1196 bounces was observed by SAMPEX, and the microburst's latitudinal scale size in LEO  
 1197 was estimated to have been "at least a few tens of kilometers". Blake et al. (1996)  
 1198 concluded that typically microbursts are less than a few tens of electron gyroradii in  
 1199 size (at  $L = 5$  at LEO, the gyroradii of 1 MeV electrons is on the order of 100 m).  
 1200 Dietrich et al. (2010) used SAMPEX along with ground-based very low frequency

1201 stations to conclude that during one SAMPEX pass, the observed microbursts had  
 1202 scale sizes less than 4 km.

1203 Since February 1st, 2015, microbursts have been observed by FIREBIRD-II, a  
 1204 pair of CubeSats in LEO. Soon after launch, when the two FIREBIRD-II spacecraft  
 1205 were at close range, a microburst with a scale size greater than 11 km was observed  
 1206 (Crew et al., 2016). On the same day, FIREBIRD-II simultaneously observed a  
 1207 microburst with multiple bounces. The microburst decay was observed over a period  
 1208 of a few seconds, while the spacecraft were traveling predominantly in latitude. Here  
 1209 we present the analysis and results of the latitude and longitude scale sizes and  
 1210 bounce periods of the first microburst with multiple bounces observed with the two  
 1211 FIREBIRD-II spacecraft.

1212 Spacecraft and Observation

1213 The FIREBIRD missions are comprised of a pair of identically-instrumented  
 1214 1.5U CubeSats (15 x 10 x 10 cm) that are designed to measure electron precipitation  
 1215 in LEO (Klumpar et al., 2015; Spence et al., 2012). The second mission, termed  
 1216 FIREBIRD-II, was launched on January 31st 2015. The two FIREBIRD-II CubeSats,  
 1217 identified as Flight Unit 3 (FU3) and Flight Unit 4 (FU4), were placed in a 632 km  
 1218 apogee, 433 km perigee, and 99° inclination orbit (Crew et al., 2016). FU3 and FU4  
 1219 are orbiting in a string of pearls configuration with FU4 ahead, to resolve the space-  
 1220 time ambiguity of microbursts. Each FIREBIRD-II unit has two solid state detectors:  
 1221 one is mounted essentially at the spacecraft surface, covered only by a thin foil acting  
 1222 as a sun shade, with a field of view of 90° (surface detector), and the other is beneath  
 1223 a collimator which restricts the field of view to 54° (collimated detector). Only FU3  
 1224 has a functioning surface detector, so this analysis utilizes the collimated detectors.  
 1225 FU3's surface and collimated detectors, as well as FU4's collimated detector observe

1226 electron fluxes in six energy channels from  $\sim 230$  keV to  $> 1$  MeV. FIREBIRD-II's  
 1227 High Resolution (HiRes) electron flux data is gathered with an adjustable sampling  
 1228 period of 18.75 ms by default and can be as fast as 12.5 ms.

1229 On February 2nd, 2015 at 06:12 UT, both FIREBIRD-II spacecraft simulta-  
 1230 neously observed an initial microburst, followed by subsequent periodic electron  
 1231 enhancements of diminishing amplitude shown in Fig. 3.1. This is thought to be  
 1232 the signature of a single burst of electrons, some of which precipitate, but the rest  
 1233 mirror near the spacecraft then bounce to the conjugate hemisphere where they mirror  
 1234 again and the subsequent bounces produce a train of decaying peaks (Blake et al.,  
 1235 1996; Thorne et al., 2005). This bounce signature occurred during the transition  
 1236 between the main and recovery phases of a storm with a minimum Dst of -44 nT  
 1237 ( $K_p = 4$ , and  $AE \approx 400$  nT). At this time, the HiRes data was sampled at 18.75 ms.  
 1238 Five peaks were observed by both spacecraft. The fifth peak observed by FU4 was  
 1239 comparable to the Poisson noise and was not used in this analysis. This microburst  
 1240 was observed from the first energy channel ( $\approx 200 - 300$  keV), to the fourth energy  
 1241 channel ( $\approx 500 - 700$  keV), and FU3's surface detector observed the microburst up  
 1242 to the fifth energy channel (683 - 950 keV).

1243 The HiRes data in Fig. 3.1 shows signs of energy dispersion, characterized by  
 1244 higher energy electrons arriving earlier than the lower energies. This time of flight  
 1245 energy dispersion tends to smear out the initial sharp burst upon each subsequent  
 1246 bounce. The first peak does not appear to be dispersed, and subsequent peaks show  
 1247 a dispersion trend consistent across energy channels. The black vertical bars have  
 1248 been added to Fig. 3.1 to highlight this energy dispersion. This dispersion signature  
 1249 and amplitude decay implies that the first peak was observed soon after the electrons  
 1250 were scattered, followed by decaying bounces.

1251 At this time, in magnetic coordinates, FIREBIRD-II was at McIlwain  $L = 4.7$

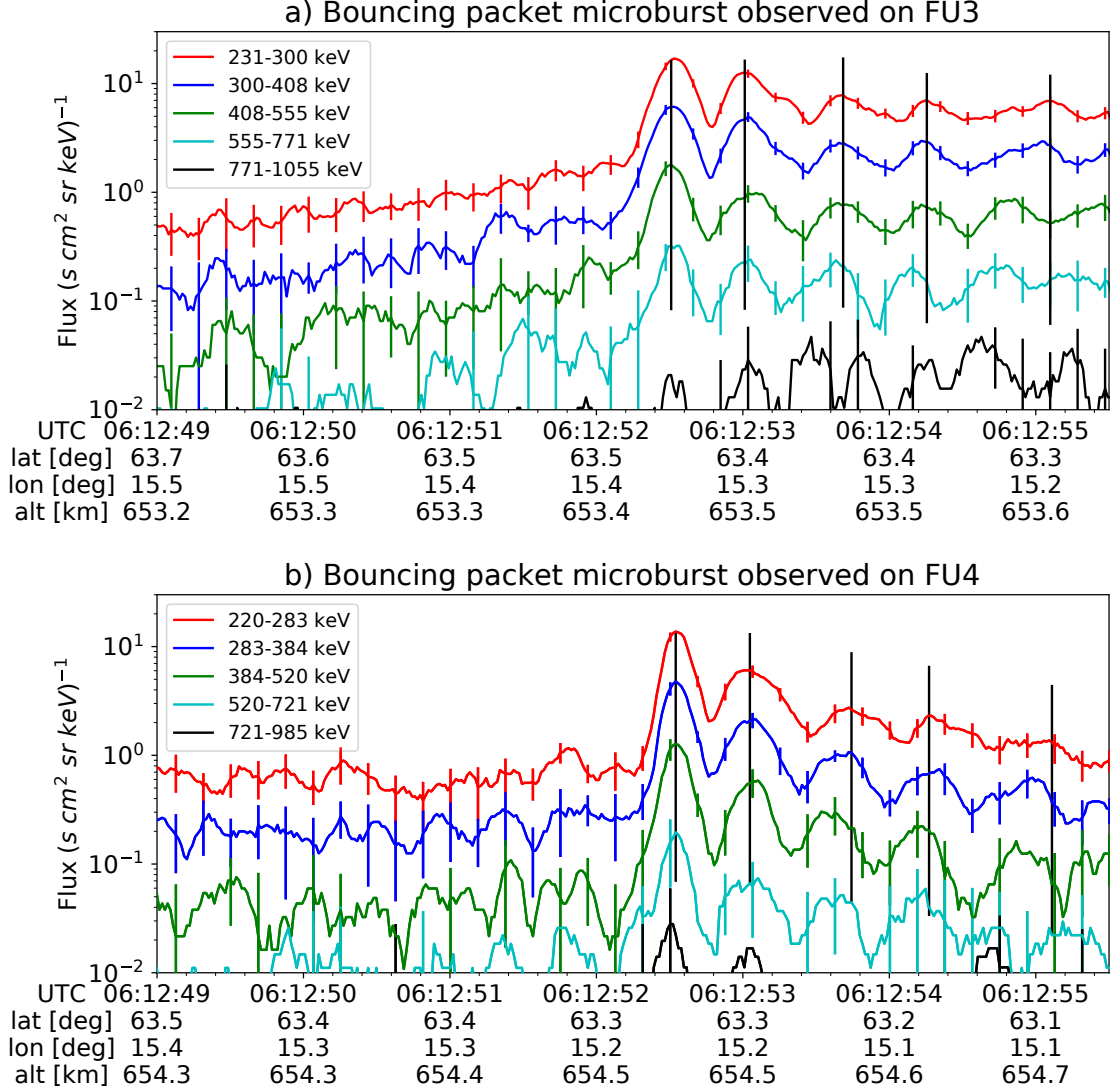


Figure 3.1: HiRes data of the microburst observed at February 2nd, 2015 at 06:12:53 UT, smoothed with a 150 ms rolling average. The subsequent bounces showed some energy dispersion. As discussed in Appendix B, a time correction of -2.28 s was applied to FU3. While the flux from five energy channels is shown, only channels with reasonable counting statistics were used for the spatial scale analysis. Vertical colored bars show the  $\sqrt{N}$  error every 10th data point and vertical black bars are lined up with the peaks in the 220-283 keV energy channel to help identify dispersion.

and MLT = 8.3, calculated with the Tsyganenko 1989 (T89) magnetic field model (Tsyganenko, 1989) using IRBEM-Lib (Boscher et al., 2012). Geographically, they were above Sweden, latitude = 63°N, longitude = 15°E, altitude = 650 km. This geographic location is magnetically conjugate to the east of the so-called South Atlantic Anomaly (SAA). The SAA is the location where the mirror points of electrons tend to occur at locations deeper in the atmosphere owing to the offset of the dipole magnetic field from the Earth's center. Electrons with pitch angles within the drift loss cone (DLC) will encounter the SAA and be removed from their eastward longitudinal drift paths (Comess et al., 2013; Dietrich et al., 2010). FU3 and FU4 are therefore both in regions where the particles in the DLC have recently precipitated, leaving only particles that were recently scattered. At the spacecraft location, locally mirroring electrons would have mirrored at 95 km in the opposite hemisphere, with more field aligned electrons mirroring at even lower altitudes. From the analysis done by Fang et al. (2010), the peak in the total ionization rate in the atmosphere for 100 keV electrons is around 80 km altitude, while the total ionization rate from 1 MeV electrons peaks around 60 km altitude. It is, therefore, expected that a fraction of the microburst electrons will survive each encounter with the atmosphere. By plotting the peak flux as a function of bounce (not shown), it was found that 40 - 60 % of the microburst electrons were lost on the first bounce, similar to the 33% loss per bounce observed for a bouncing microburst observed by SAMPEX (Thorne et al., 2005).

1272

## Analysis

At the beginning of the FIREBIRD-II mission, two issues prevented the proper analysis of the microburst's spatial scale size: the spacecraft clocks were not synchronized, and their relative positions were not accurately known. We addressed these issues with a cross-correlation time lag analysis described in detail in Appendix

1277 B. From this analysis, the time correction was  $2.28 \pm 0.12$  s (applied to Fig. 3.1) and  
 1278 the separation was  $19.9 \pm 0.9$  km at the time of the microburst observation.

1279 Electron Bounce Period

1280 We used this unique observation of bouncing electrons to calculate the bounce  
 1281 period,  $t_b$  as a function of energy and compare it to the energy-dependent  $t_b$  curves  
 1282 derived from four magnetic field models, the results of which are shown in Fig. 3.2.  
 1283 The observed  $t_b$  and uncertainties were calculated by fitting the baseline-subtracted  
 1284 HiRes flux. The baseline flux used in this analysis is given in O'Brien et al. (2004)  
 1285 as the flux at the 10th percentile over a specified time interval, which in this analysis  
 1286 was taken to be 0.5 seconds. The flux was fitted with a superposition of Gaussians  
 1287 for each energy channel, and the uncertainty in flux was calculated using the Poisson  
 1288 error from the microburst and baseline fluxes summed in quadrature. Using the fit  
 1289 parameters, the mean  $t_b$  for the lowest four energy channels is shown in Fig. 3.2. The  
 1290 trend of decreasing  $t_b$  as a function of energy is evident in Fig. 3.2, which further  
 1291 supports the assumption that the subsequent peaks are bounces, and not a train of  
 1292 microbursts scattered by bouncing chorus.

1293 The decaying peaks in the 231-408 keV electron flux observed by FU3's lowest  
 1294 two energy channels (see Fig. 3.1) were right-skewed. One explanation is that there  
 1295 was in-channel energy dispersion within those channels. Since  $t_b$  of higher energy  
 1296 electrons is shorter, a right-skewed peak implies that higher energy electrons were  
 1297 more abundant within that channel e.g. in FU3's 231-300 keV channel, the 300 keV  
 1298 electrons will arrive sooner than the 231 keV electrons, but will they will be binned  
 1299 in the same channel. A Gaussian fit cannot account for this in-channel dispersion,  
 1300 and as a first order correction, minima between peaks was used to calculate  $t_b$ , and  
 1301 is shown in Fig. 3.2. The observed energy-dependent dispersion shown in Fig. 3.2

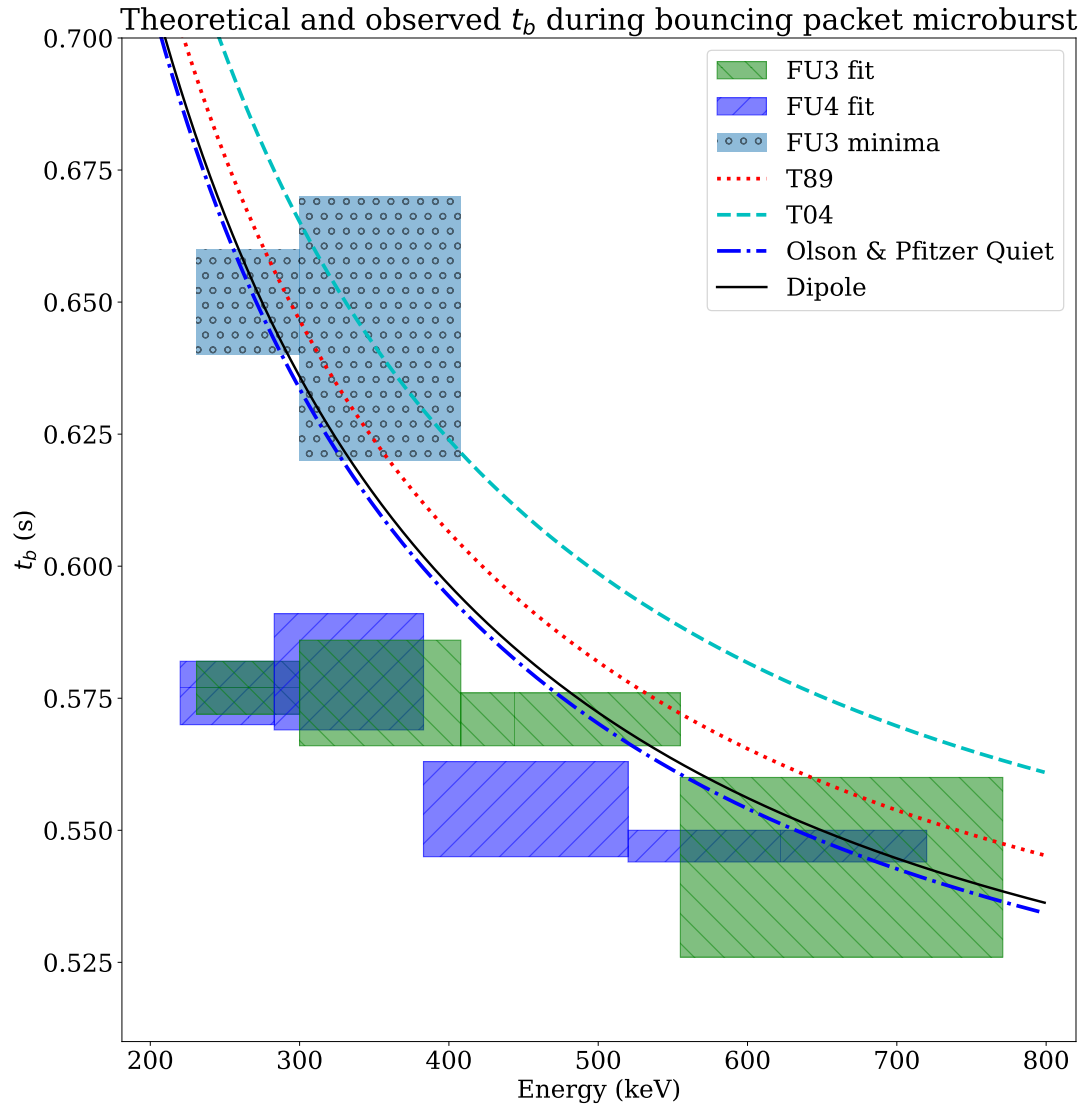


Figure 3.2: Observed and theoretical  $t_b$  for electrons of energies from 200 to 770 keV. The solid black line is  $t_b$  in a dipole magnetic field, derived in Schulz and Lanzerotti (1974). The red dotted and cyan dashed lines are the  $t_b$  derived using the T89, and T04 magnetic field models with IRBEM-Lib. Lastly, the blue dot-dash curve is the  $t_b$  derived using the Olson & Pfitzer Quiet model. The green and purple rectangles represent the observed  $t_b$  for FU3 and FU4 using a Gaussian fit, respectively. The blue rectangles represent the observed  $t_b$  calculated with the minima between the bounces. The width of the boxes represent the width of those energy channels, and the height represents the uncertainty from the fit.

1302 is consistent with higher energy peaks returning sooner. This dispersion consistency  
 1303 further supports the assumption that the subsequent peaks are bounces, and not a  
 1304 train of microbursts scattered by bouncing chorus.

1305 To compare the observed and modeled  $t_b$ , we superposed  $t_b$  curves for various  
 1306 models including an analytical solution in a dipole (Schulz and Lanzerotti, 1974), and  
 1307 numerical models: T89, Tsyganenko 2004 (T04) (Tsyganenko and Sitnov, 2005), and  
 1308 Olson & Pfitzer Quiet (Olson and Pfitzer, 1982) in Fig. 3.2. The numerical  $t_b$  curves  
 1309 were calculated using a wrapper for IRBEM-Lib. This code traces the magnetic field  
 1310 line between mirror points, and calculates  $t_b$  assuming conservation of energy and the  
 1311 first adiabatic invariant for electrons mirroring at FIREBIRD-II. With the empirical  
 1312  $t_b$ , the models agree within FIREBIRD-II's uncertainties, but the T04 model has the  
 1313 largest discrepancy compared to the other models.

1314 Microburst Energy Spectra

1315 Next, we investigated the energy spectra of this microburst. The energy spectra  
 1316 was modeled with an exponential that was fit to the peak flux derived from the  
 1317 Gaussian fit parameters in section 3 to all but the highest energy channel. We found  
 1318 that the E-folding energy,  $E_0 \sim 100$  keV. This spectra is similar to spectra show  
 1319 by Lee et al. (2005) from STSAT-1 and Datta et al. (1997) from sounding rocket  
 1320 measurements. The energy spectra is soft for a typical microburst observed with  
 1321 FIREBIRD-II and there was no statistically significant change in  $E_0$  for subsequent  
 1322 bounces.

1323 Microburst Scale Sizes

1324 Lastly, after we applied the time and separation corrections detailed in Appendix  
 1325 B, we mapped the locations of FU3 and FU4 in Fig. 3.3. The locations where FU3 saw  
 1326 peaks 1-5 and where FU4 saw peaks 1-4 are shown as P1-5 and P1-4, respectively.

1327 The lower bound on the latitudinal extent of the microburst was the difference in  
 1328 latitude between P1 on FU3 and P4 on FU4 and was found to be  $29 \pm 1$  km. The  
 1329 uncertainty was estimated from the spacecraft separation uncertainty described in  
 1330 Appendix B. This scale size is the largest reported by FIREBIRD-II.

1331 In section 3, we showed that the observed decaying peaks were likely due to  
 1332 bouncing, so we assume that the observed electrons in subsequent bounces were the  
 1333 drifted electrons from the initial microburst. Under this assumption, the scattered  
 1334 electrons observed in the last bounce by FIREBIRD-II, must have drifted east from  
 1335 their initial scattering longitude, allowing us to calculate the minimum longitudinal  
 1336 scale size. Following geometrical arguments, the distance that electrons drift east in  
 1337 a single bounce is a product of the circumference of the drift shell foot print, and the  
 1338 fraction of the total drift orbit traversed in a single bounce and is given by,

$$d_{az} = 2\pi(R_E + A) \cos(\lambda) \frac{t_b}{\langle T_d \rangle} \quad (3.1)$$

where  $R_E$  is the Earth's radius,  $A$  is the spacecraft altitude,  $\lambda$  is the magnetic latitude,  
 $t_b$  is the electron bounce period, and  $\langle T_d \rangle$  is the electron drift period. Parks (2003)  
derived  $\langle T_d \rangle$  to be,

$$\langle T_d \rangle \approx \begin{cases} 43.8/(L \cdot E) & \text{if } \alpha_0 = 90^\circ \\ 62.7/(L \cdot E) & \text{if } \alpha_0 = 0^\circ \end{cases} \quad (3.2)$$

1339 where  $E$  is the electron energy in MeV,  $L$  is the L shell, and  $\alpha_0$  is the equatorial pitch  
 1340 angle. Electrons mirroring at FIREBIRD-II have  $\alpha_0 \approx 3.7^\circ$  and so the  $\alpha_0 = 0^\circ$  limit  
 1341 was used.

1342 The microburst's longitudinal scale size is defined as the distance the highest  
 1343 energy electrons drifted in the time between the observations of the first and last  
 1344 peaks. This scale size is given by  $D_{az} = n d_{az}$  where  $n$  is the number of bounces

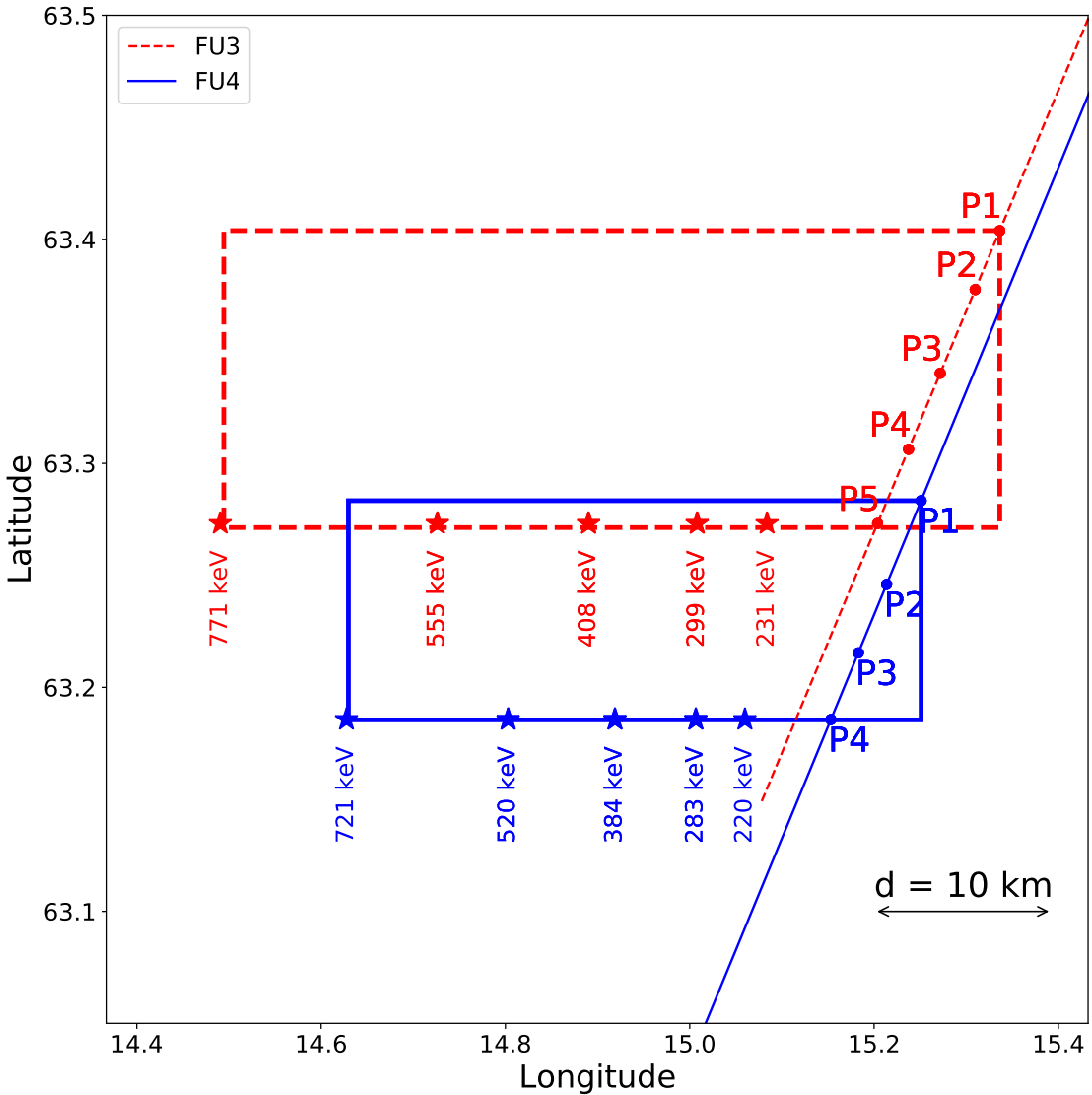


Figure 3.3: The topology of the FIREBIRD-II orbit and the multiple bounces of the microburst projected onto latitude and longitude with axis scaled to equal distance. Attributes relating to FU3 shown in red dashed lines, and FU4 with blue solid lines. The spacecraft path is shown with the diagonal lines, starting at the upper right corner. The labels P1-4 for FU4 and P1-5 for FU3 indicate where the spacecraft were when the  $N^{\text{th}}$  peak was seen in the lowest energy channel in the HiRes data. The stars with the accompanying energy labels represent the locations of the electrons with that energy that started at time of P1, and were seen at the last peak on each spacecraft. The rectangles represent the lower bound of the microburst scale size, assuming that the majority of the electrons were in the upper boundary of energy channel 4.

1345 observed. The stars in Fig. 3.3 (with labels corresponding to energy channel  
 1346 boundaries) represent the locations when the microburst was observed at P1, such  
 1347 that an electron of that energy would drift eastward to be seen at P5 for FU3 and P4  
 1348 for FU4. Since FU3 observed more peaks it observed the larger longitudinal scale size  
 1349 which is shown with the red dashed box in Fig. 3.3. FU3's fourth energy channel's  
 1350 bounds are 555 keV and 771 keV, which correspond to longitudinal distances of  $39 \pm 1$   
 1351 km and  $51 \pm 1$ , respectively. The uncertainty was estimated by propagating the  
 1352 uncertainty in the bounce time Eq. 3.1. While the observed minimum longitudinal  
 1353 scale size is dependent on FIREBIRD-II's energy channels, the true scale size may  
 1354 not be.

1355 To investigate how the microburst scale size compares to the scale sizes of chorus  
 1356 waves near the magnetic equator, the microburst's longitudinal and latitudinal scale  
 1357 sizes and their uncertainties in LEO were mapped to the magnetic equator with T89.  
 1358 The radial scale size (latitudinal scale mapped from LEO) was greater than  $500 \pm 10$   
 1359 km. The azimuthal scale size (longitudinal scale mapped from LEO) of 555 keV  
 1360 electrons was greater than  $450 \pm 10$  km and for the 771 keV electrons it was greater  
 1361 than  $530 \pm 10$  km. The lower bound microburst scale size is similar to the chorus  
 1362 scale sizes derived by Agapitov et al. (2017, 2011), and is discussed below.

1363

### Discussion and Conclusions

1364 We presented the first observation of a large microburst with multiple bounces  
 1365 made possible by the twin FIREBIRD-II CubeSats. The microburst's lower bound  
 1366 LEO latitudinal and longitudinal scale sizes of  $29 \pm 1$  km and  $51 \pm 1$  km make  
 1367 it one of the largest observed. The microburst's LEO scale size was larger than  
 1368 the latitudinal scale sizes of typical  $> 1$  MeV microbursts reported in Blake et al.  
 1369 (1996), approximately 10 times larger than reported in Dietrich et al. (2010), and

1370 approximately 2.6 times larger than other simultaneous microbursts observed by  
 1371 FIREBIRD-II (Crew et al., 2016). Lastly, the scale sizes derived here were similar to  
 1372 the scale sizes of  $\sim$  15 keV microbursts observed with a high altitude balloon (Parks,  
 1373 1967). No energy dependence on the minimum latitudinal scale size was observed,  
 1374 while the observed energy dependence of the minimum longitudinal scale size is an  
 1375 artifact of the technique we used to estimate their drift motion.

1376 The microburst scale size obtained in Section 3 and scaled to the geomagnetic  
 1377 equator can be compared with the scales of chorus waves presumably responsible for  
 1378 the rapid burst electron precipitation. Early direct estimates of the chorus source  
 1379 scales were made by the coordinated measurement by ISEE-1, 2. The wave power  
 1380 correlation scale was estimated to be about several hundred kilometers across the  
 1381 background magnetic field (Gurnett et al., 1979). Furthermore, Santolik et al. (2003)  
 1382 determined the correlation lengths of chorus-type whistler waves to be around 100  
 1383 km based on multipoint CLUSTER Wide Band Data measurements near the chorus  
 1384 source region at  $L \approx 4$ , during the magnetic storm of 18 April 2002. Agapitov et al.  
 1385 (2017, 2011, 2010) recently showed that the spatial extent of chorus source region can  
 1386 be larger, ranging from 600 km in the outer radiation belt to more than 1000 km in  
 1387 the outer magnetosphere. The lower bound azimuthal and latitudinal scales obtained  
 1388 in Section 3 and scaled to the magnetic equator, are similar to the whistler-mode  
 1389 chorus source scale sizes reported in Agapitov et al. (2017, 2011).

1390 No wave measurements from nearby spacecraft were available at this time.  
 1391 Nevertheless, during the hours before and after this observation, the Van Allen Probes'  
 1392 (Mauk et al., 2013) Electric and Magnetic Field Instrument and Integrated Science  
 1393 (Kletzing et al., 2013) observed strong wave power in the lower band chorus frequency  
 1394 range, inside the outer radiation belt between 22 and 2 MLT. Furthermore, AE  $\sim 400$   
 1395 nT at this time, and relatively strong chorus waves were statistically more likely to

<sup>1396</sup> be present at FIREBIRD-II's MLT (Li et al., 2009b).

<sup>1397</sup> The empirically estimated and modeled  $t_b$  in this study agree within FIREBIRD-II's uncertainties, confirming that the energy-dependent dispersion was due to <sup>1398</sup> bouncing. The  $t_b$  curves are a proxy for field line length, and this agreement implies <sup>1399</sup> that they are comparable. This is expected since the magnetosphere is not drastically <sup>1400</sup> compressed at 8 MLT, but we expect a larger discrepancy near midnight, where the <sup>1401</sup> magnetosphere is more stretched and difficult to accurately model. In future studies, <sup>1402</sup> this analysis can be used as a diagnostic tool to validate field line lengths, and improve <sup>1403</sup> magnetic field models.

<sup>1405</sup> The similarity of the microburst and chorus source region scale sizes, as well <sup>1406</sup> as magnetospheric location and conditions, further support the causal relationship <sup>1407</sup> between microbursts and chorus.

<sup>1408</sup>

### Acknowledgments

<sup>1409</sup> This work was made possible with help from the FIREBIRD team, and the <sup>1410</sup> members of the Space Sciences and Engineering Laboratory at Montana State <sup>1411</sup> University for their hard work to make this mission a success. In addition, M. <sup>1412</sup> Shumko acknowledges Drew Turner for his suggestions regarding the bounce period <sup>1413</sup> calculations, and Dana Longcope for his proofreading feedback. The FIREBIRD-II <sup>1414</sup> data are available at [http://solar.physics.montana.edu/FIREBIRD\\_II/](http://solar.physics.montana.edu/FIREBIRD_II/). This analysis <sup>1415</sup> is supported by the National Science Foundation under Grant Numbers 0838034 and <sup>1416</sup> 1339414. Furthermore, the work of O. Agapitov was supported by the NASA grant <sup>1417</sup> NNX16AF85G.

1418

## CHAPTER FOUR

1419

## MICROBURST SIZE DISTRIBUTION DERIVED WITH AEROCUBE-6

1420

Contribution of Authors and Co-Authors

1421 Manuscript(s) in Chapter(s) 1

1422

1423 Author: [type author name here]

1424 Contributions: [list contributions here, single-spaced]

1425 Co-Author: [type co-author name here]

1426 Contributions: [list contributions here, single-spaced]

1427 Co-Author: [type co-author name here]

1428 Contributions: [list contributions here, single-spaced]

1429

1430

Manuscript Information

1431 [Type Author and Co-author(s) Names Here]

1432 Journal of Geophysical Research

1433 Status of Manuscript: **Officially submitted to a peer-reviewed journal**

1434 Wiley

1435

1436

Key Points

- 1437     ● The dual AeroCube-6 CubeSats simultaneously observed  $> 35$  keV microbursts  
 1438       at a variety of spatial separations ranging from 2 to  $\approx 100$  km.
- 1439     ● In low Earth orbit the majority of microbursts have a size on the order of a few  
 1440       tens of km.
- 1441     ● At the magnetic equator, the size of most microbursts corresponds to the size  
 1442       of whistler-mode chorus wave packets.

1443

Abstract

1444     Microbursts are an impulsive increase of electrons from the radiation belts  
 1445     into the atmosphere and have been directly observed in low Earth orbit and the  
 1446     upper atmosphere. Prior work has estimated that microbursts are capable of rapidly  
 1447     depleting the radiation belt electrons on the order of a day, hence their role to  
 1448     radiation belt electron losses must be considered. Losses due to microbursts are not  
 1449     well constrained, and more work is necessary to accurately quantify their contribution  
 1450     as a loss process. To address this question we present a statistical study of  $> 35$   
 1451     keV microburst sizes using the pair of AeroCube-6 CubeSats. The microburst size  
 1452     distribution in low Earth orbit and the magnetic equator was derived using both  
 1453     spacecraft. In low Earth orbit, the majority of microbursts were observed while the  
 1454     AeroCube-6 separation was less than a few tens of km, mostly in latitude. To account  
 1455     for the statistical effects of random microburst locations and sizes, a Monte Carlo and  
 1456     analytic models were developed to test hypothesized microburst size distributions. A  
 1457     family of microburst size distributions were tested and a Markov Chain Monte Carlo  
 1458     sampler was used to estimate the optimal distribution of the microburst size model

parameters. Finally, a majority of observed microbursts map to sizes less than 200 km at the magnetic equator. Since microburst are widely believed to be generated by scattering of radiation belt electrons by whistler mode waves, the observed microburst size correlates to coherent whistler mode chorus sizes derived in prior literature.

1463

## Introduction

Since the discovery of the Van Allen radiation belts in the 1960s by Van Allen (1959) and Vernov and Chudakov (1960), decades of research has made headway in understanding the various particle acceleration and loss mechanisms. One of the extensively studied mechanisms responsible for both acceleration and loss is wave-particle scattering between whistler-mode chorus waves and electrons (Abel and Thorne, 1998; Bortnik et al., 2008; Horne and Thorne, 2003; Meredith et al., 2002; Millan and Thorne, 2007; Thorne et al., 2005). Whistler-mode chorus waves are typically generated by a temperature anisotropy of low energy electrons up to tens of kiloelectronvolts (keV) and are typically found in the  $\sim 0 - 12$  magnetic local times (MLT) (Li et al., 2009a,b). Whistler-mode chorus waves interact with radiation belt electrons, and are widely believed to cause electron precipitation termed microbursts (e.g. Millan and Thorne, 2007).

Microbursts are a subsecond impulse of electrons that are observed by high altitude balloons and satellites in low Earth orbit (LEO) on radiation belt magnetic footprints  $\sim 4 - 8$  L-shell (L) (e.g. Anderson and Milton, 1964; Breneman et al., 2017; Crew et al., 2016; Greeley et al., 2019; Lorentzen et al., 2001a; Mozer et al., 2018; O'Brien et al., 2003; Tsurutani et al., 2013; Woodger et al., 2015), mostly in the dawn MLTs, and with an enhanced occurrence rate during disturbed magnetospheric times (Douma et al., 2017; O'Brien et al., 2003). Microburst's role as a radiation belt electron loss mechanism has been estimated to be significant, with total radiation belt

1484 electron depletion due to microbursts estimated to be on the order of a day (Breneman  
 1485 et al., 2017; Lorentzen et al., 2001b; O'Brien et al., 2004; Thorne et al., 2005). These  
 1486 average microburst loss estimates are not well constrained due to assumptions made  
 1487 regarding the microburst precipitation region.

1488 One of the unconstrained microburst parameters that is critical to better  
 1489 quantify the role of microbursts as an instantaneous loss mechanism (the number  
 1490 of electrons lost per microburst) is their physical size. Historically, after the  
 1491 bremsstrahlung X-ray signatures of microbursts were discovered by Anderson and  
 1492 Milton (1964), numerous microburst size studies were done using other balloon flights  
 1493 in the mid 1960s. Brown et al. (1965) used data from a pair of balloons separated  
 1494 by 150 km, mainly in longitude, and found that one third of all microbursts observed  
 1495 were temporally coincident. Trefall et al. (1966) then used the results from Brown  
 1496 et al. (1965) to model the probability that a microburst will be observed by two  
 1497 balloons as a function of the radius of the microburst, radius of the precipitating area  
 1498 a balloon is sensitive to, and the balloon separation. Trefall et al. (1966) concluded  
 1499 that the microbursts reported by Brown et al. (1965) must have had a diameter of  
 1500 230 km assuming a balloon has a circular field of view with a 140 km diameter (for  
 1501 electrons stopped at 100 km altitudes). Soon after, Barcus et al. (1966) used a pair of  
 1502 balloons and concluded that a microburst must have a  $< 200$  km longitudinal extent.  
 1503 Then Parks (1967) used data from a single balloon with four collimated scintillators  
 1504 oriented in different directions and found that the size of some mostly low energy  
 1505 microbursts to have a diameter of  $80 \pm 28$  km, and others were less than 40 km.

1506 Direct observations of microburst electrons are made by LEO spacecraft. Blake  
 1507 et al. (1996) found a microburst with a size of a few tens of km using the the Solar  
 1508 Anomalous and Magnetospheric Particle Explorer (SAMPEX) and concluded that  
 1509 typically microbursts are less than a few tens of electron gyroradii in size (order of

1510 a few km in LEO). Recently, Dietrich et al. (2010) used SAMPEX observations in  
1511 another case study and concluded that the observed microbursts were smaller than 4  
1512 km. Crew et al. (2016) used the Focused Investigation of Relativistic Electron Bursts:  
1513 Intensity, Range, and Dynamics (FIREBIRD-II) CubeSats and found an example of  
1514 a microburst larger than 11 km. Lastly, Shumko et al. (2018) also used FIREBIRD-II  
1515 to identify a microburst with a size greater than  $51 \pm 1$  km. If anything, the large  
1516 variance in prior results imply that there is a distribution of microburst scale sizes  
1517 which this study aims to estimate.

1518 Besides addressing the instantaneous radiation belt electron losses due to  
1519 individual microbursts, the microburst size distribution is useful to identify the wave  
1520 mode(s) responsible for scattering microbursts. By mapping the microburst size  
1521 distribution in LEO to the magnetic equator it can be compared to the wave sizes  
1522 estimated in prior literature. This comparison can be used to identify the waves and  
1523 their properties (e.g. amplitude or coherence) responsible for scattering microburst  
1524 electrons.

1525 This paper addresses these two questions by expanding the prior microburst  
1526 size case studies by analyzing microburst observations over a three year time period  
1527 to estimate the microburst size distribution in LEO and the magnetic equator. The  
1528 twin AeroCube-6 (AC6) CubeSats are utilized for this study because they were ideally  
1529 equipped to observe microbursts simultaneously over a span of three years while their  
1530 total separation varied between 2 and 800 km, mostly in latitude (in-track in orbit).  
1531 This paper first describes the AC-6 mission, including their orbit and instrumentation  
1532 in section 4. Section 4 develops the methodology used to identify microbursts observed  
1533 by each spacecraft and how they were combined to make a list of simultaneously  
1534 observed microbursts. Section 4 describes the methodology used to estimate the  
1535 microburst size distributions in LEO and the magnetic equator as a function of AC6

1536 separation. Then a model is developed to shed light on how the compounding effects of  
 1537 a hypothesized microburst shape, size distribution, and random microburst locations  
 1538 will be observed by AC6, a two-point measurement platform. Lastly, in section 4  
 1539 we discuss these results and compare the microburst sizes estimated here to the size  
 1540 distribution of the whistler-mode chorus waves that are believed to cause microbursts.

1541

### Instrumentation

1542 The AC6 mission consists of a pair of 0.5U (10x10x5 cm) CubeSats built by  
 1543 The Aerospace Corporation and launched on June 19th, 2014 into a 620 x 700 km,  
 1544 98° inclination orbit. The two satellites, designated as AC6-A and AC6-B, separated  
 1545 after launch and drifted apart. Both AC6 units have an active attitude control system  
 1546 which allows them to adjust the atmospheric drag experienced by each AC6 unit by  
 1547 orienting their solar panel “wings” with respect to the ram direction. By changing  
 1548 their orientation, AC6 was able to achieve fine separation control and maintain a  
 1549 separation between 2-800 km. Figure 4.1a shows the AC6 separation for the duration  
 1550 of the mission. Figure 4.1b shows where AC6 was taking 10 Hz data simultaneously  
 1551 as a function of L and MLT which highlights that most data was taken at 8-12 MLT,  
 1552 an ideal local time for observing microbursts. Lastly Fig. 4.1b shows that the AC6  
 1553 orbit was roughly dawn-dusk, sun-synchronous and precessed only a few hours in  
 1554 MLT over a three year period.

1555 Each AC6 unit is equipped with three Aerospace microdosimeters (licensed to  
 1556 Teledyne Microelectronics, Inc). The dosimeter used for this study is dos1 and is  
 1557 identical on both AC6 units. Dos1 has a 35 keV electron threshold and all dosimeters  
 1558 sample at 1 Hz in survey mode, and 10 Hz in burst mode in the radiation belts. More  
 1559 detailed technical information on AC6 is described in O’Brien et al. (2016b).

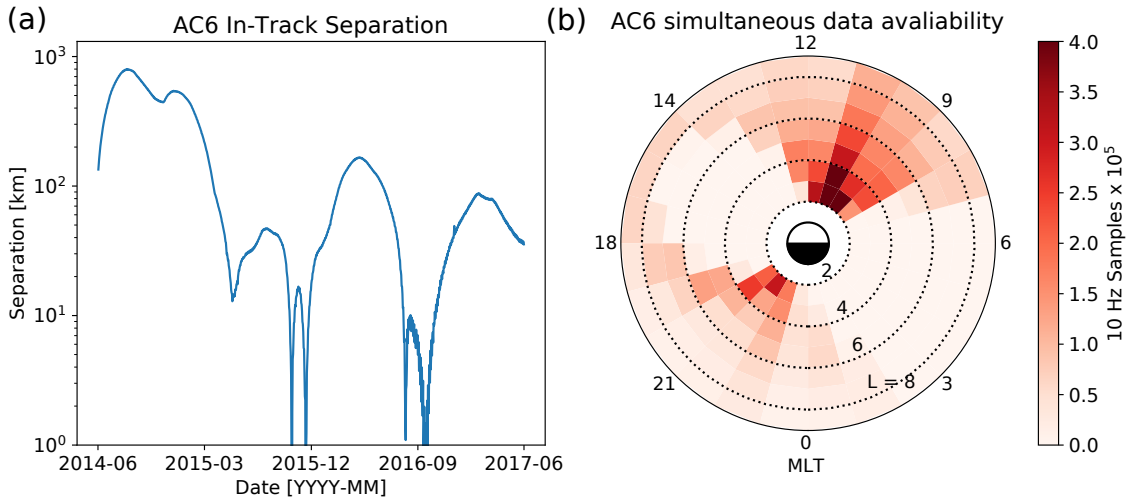


Figure 4.1: AC6 mission properties for (a) spacecraft separation and (b) number of simultaneous quality 10 Hz samples as a function of L and MLT.

1560

## Methodology

### 1561 Microburst Detection

1562 The first step to find microbursts observed simultaneously by AC6 is to identify  
 1563 them on each individual spacecraft. Microbursts were detected with two different  
 1564 methods that yielded quantitatively similar results. The first method is the burst  
 1565 parameter (O'Brien et al., 2003). This algorithm has been successfully used in other  
 1566 microburst studies, mainly with the microbursts observed by SAMPEX (e.g. Blum  
 1567 et al., 2015; Douma et al., 2017; O'Brien et al., 2003). For AC6, a burst parameter  
 1568 threshold of 5 was determined to be a good trade-off between false positive and false  
 1569 negative microburst detections. Another microburst detection algorithm based on  
 1570 wavelet spectra frequency filtering was developed and the resulting list of microbursts  
 1571 is similar to the list from the burst parameter.

1572 With the two microburst detection lists in hand, data cleaning to remove  
 1573 microburst-like transmitter noise was necessary. The transmitters on AC6 can

cause unphysical count impulses in the dosimeters that resembles periodic trains of microbursts. One source of transmitter noise was observed at times when AC6 was in contact with the ground stations above the US for data downloads and commanding, thus the microburst detections made above the US that were mostly at low L were discarded.

Another source of noise is crosslink transmissions between AC6-A and AC6-B. These transmissions occurred when either spacecraft transitioned from the survey mode to 10 Hz mode. This noise is sometimes not caught by the data quality flag, so the following empirically-derived criteria were developed to remove those detections. The dosimeter with a 250 keV nominal electron threshold, dos2, was used because it had a nearly identical response to noise while rarely responded to microbursts. Since the transmitter noise is very periodic with a  $\approx 0.2$  s period, cross-correlation (CC) and autocorrelation (AC) methods were applied to the dos1 and dos2 time series. Detections were discarded if the following two criteria were met: either dos1 or dos2 time series had a AC peak at a 0.2 or 0.4 s lag and the dos1-dos2 CC was greater than 0.9. The AC lag criteria alone sometimes falsely removed legitimate trains of microbursts, so the second criteria insured that the detection was removed if there was also an unphysically high correlation across an order of magnitude in energy.

The lists of microbursts observed individually by AC6 were then merged into a list of temporally correlated microbursts, i.e. microbursts that were observed simultaneously by both AC6 units, with the following procedure. The general idea is that a microburst detected by one spacecraft will cross-correlate well with the time series from the other spacecraft if it observed a similar microburst, and poorly if there was no microburst observed by the other spacecraft. Each microburst detection made by either spacecraft was cross-correlated with the time series from the other spacecraft whether or not a microburst was observed by the other spacecraft. Cross-

1600 correlation windows with 1 and 1.2 s widths were chosen with slightly different  
 1601 window sizes to account for random count variation due to Poisson noise. Microbursts  
 1602 detections that had a cross-correlation greater than 0.8 were considered temporally  
 1603 coincident. This CC threshold was chosen as it is low enough to accept user-identified  
 1604 temporally coincident microbursts superposed with noise, and high enough to reject  
 1605 most non-coincident events. Figure 4.2, panels (a), (c), (e), and (g) show examples  
 1606 of microbursts observed by both AC6 units when they were separated by 5, 16, 37,  
 1607 and 69 km, respectively.

1608 The last criteria requires that the temporal CC must be greater than the spatial  
 1609 CC + 0.3. The spatial CC was calculated by shifting one spacecraft's time series  
 1610 by the in-track lag to cross-correlate in the same spatial location, i.e. latitude.  
 1611 This criteria was applied to remove curtains, stationary structures observed by AC6  
 1612 that are narrow in latitude (Blake and O'Brien, 2016) that can be misidentified as  
 1613 microbursts. Figure 4.2, panels (b), (d), (f), and (h) show the shifted time series to  
 1614 confirm that there were no spatially correlated, non-microburst structures present.  
 1615 Lastly the merged microburst list was spot checked by two authors to remove poorly  
 1616 correlated and any duplicate events. After filtering out transmitter noise and applying  
 1617 the CC criteria, 662 simultaneous microburst detections were found and used in this  
 1618 study.

1619 Microburst Size Distribution in LEO and Magnetic Equator

1620 The temporally coincident microbursts, which from now on will be referred to  
 1621 as microbursts, are now used to estimate the fraction of microbursts observed above  
 1622 AC6 separation,  $s$ . When AC6 observes a microburst at  $s$ , the microburst's size  
 1623 must be greater than  $s$ . This fact, along with the arguments presented in Section 4  
 1624 in Joy et al. (2002) who studied the most probable Jovian magnetopause and bow

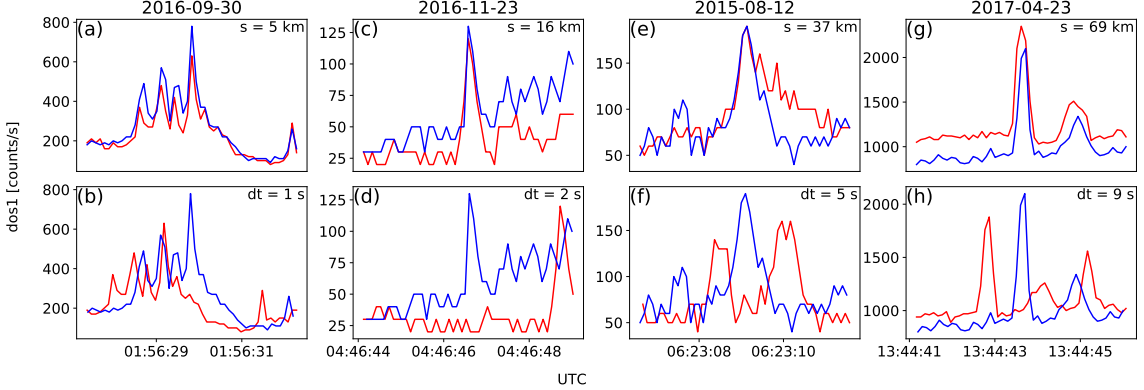


Figure 4.2: Examples of  $> 35$  keV microbursts observed simultaneously by AC6-A in red and AC6-B in blue. Panels (a), (c), (e), and (g) show the temporally-aligned time series when AC6 were separated by  $s = 5, 16, 37$ , and  $69$  km, respectively. The corresponding panels (b), (d), (f), and (h) show the spatially-aligned time series which is made by shifting the AC6-A time series in the above panels by the in-track lag (annotated with  $dt$ ) that show any spatially correlated structures. The clear temporal correlation and lack of spatial correlation demonstrates that these events are microbursts.

shock stand off distances, are used to investigate the dependence of the number of microbursts observed above  $s$ , as a function of  $s$ . This dependence is the microburst complementary cumulative distribution function  $\bar{F}(s)$ .

The cumulative fraction of microbursts observed above  $s$  is the ratio of  $N(s)$ , the normalized number of microbursts observed above  $s$ , to  $N(0)$ , the total number of microbursts observed

$$\bar{F}(s) = \frac{N(s)}{N(0)} \quad (4.1)$$

where  $N(s)$  is defined by

$$N(s) = \sum_{i=s}^{\infty} n_i \left( \frac{S_{max}}{S_i} \right) \quad (4.2)$$

where  $n_i$  is the number of microbursts observed by AC6 in  $i$ th separation bin. The normalization term  $S_{max}/S_i$  is a ratio of the number of 10 Hz samples in

1631 the most sampled separation bin to the number of samples in the ith bin. This  
 1632 normalization factor corrects AC6's non-uniform sampling in separation, thus  $\bar{F}(s)$   
 1633 can be interpreted as the fraction of microbursts observed above  $s$  assuming AC6  
 1634 sampled evenly in separation. Microburst  $\bar{F}(s)$  in LEO is shown by the black curve  
 1635 in Fig. 4.3a for  $4 < L < 8$  and split into one L-wide bins with the colored curves. The  
 1636 separation bin width used in Fig. 4.3 is 5 km. To check for bias in  $\bar{F}(s)$  due to the  
 1637 choice of separation bins,  $\bar{F}(s)$  was resampled using other bin widths and offsets. Bin  
 1638 widths as large as 20 – 30 km and bin offsets did not qualitatively effect the curves  
 1639 in Fig. 4.3a. The normalization i.e., the number of 10 Hz samples in each separation  
 1640 bin, is shown in 4.3c.

1641 The overall trend in Fig. 4.3a shows a sudden cumulative probability drop off,  
 1642 followed by a shoulder up to  $s \approx 70$  km where  $\bar{F}(s)$  drops to nearly zero. A large  
 1643 negative gradient of  $\bar{F}(s)$  at some separation implies that microbursts must be smaller  
 1644 than that separation. To quantify this, Fig. 4.3b shows the microburst probability  
 1645 density function (PDF), calculated by differentiating  $\bar{F}(s)$ . The microburst PDF  
 1646 shows a peak at  $s < 30$  km as well as a peak between 70 – 80 km separation. These  
 1647 PDF peaks are evidence of a sub 30 km microburst population and larger microbursts  
 1648 observed up 70–80 km separations. The shaded region around the black curves in Fig.  
 1649 4.3a-b shows the standard error due to counting statistics. The uncertainty due to  
 1650 false coincidence events i.e. two unrelated microbursts lining up in time by random  
 1651 chance was also considered. The microburst duty cycle in a one minute window  
 1652 ( $\approx 1 L$ ) around each microburst was calculated. The false coincidence probability is  
 1653 the square of the duty cycle and was found to be less than 5% for the majority of  
 1654 microbursts. The false coincidence probability for each microburst was then used to  
 1655 randomly remove microbursts and  $\bar{F}(s)$  was recalculated in  $10^4$  trials. The spread in  
 1656 the  $\bar{F}(s)$  trial curves with microbursts randomly removed was much smaller than the

1657 uncertainty due to counting statistics alone.

1658 To compare the microburst size to the size of their hypothesized progenitor  
1659 waves, the spacecraft locations during observed microbursts were mapped to the  
1660 magnetic equator using the Olson-Pfitzer magnetic field model (Olson and Pfitzer,  
1661 1982) which is implemented with a Python wrapper for IRBEM-Lib (Boscher et al.,  
1662 2012). As previously stated, a microburst observed in LEO has a size larger than  
1663 the spacecraft separation, hence that microburst would also have a size larger than  
1664 the spacecraft separation after it was mapped to the magnetic equator. Thus  
1665 the procedure to estimate  $\bar{F}(s)$  is identical to the LEO size distribution but with  
1666 a different normalization. The normalization factors were calculated by mapping  
1667 every quality AC6 sample to the magnetic equator and binning them by equatorial  
1668 separation into 100 km wide bins. Figure 4.4 shows the equatorial microburst size  
1669 distribution in the same format as Fig. 4.3. The equatorial PDF trend is similar to  
1670 LEO and most of the microbursts were observed when the AC6 equatorial separation  
1671 was less than 200 km.

1672 The results in Figs. 4.3 and 4.4 show the fraction of microbursts observed above a  
1673 spacecraft separation and do not fully represent the microbursts size distribution due  
1674 to the compounding effects from the range of microburst sizes and random locations  
1675 of microbursts with respect to AC6 i.e. even if the microburst size is much larger than  
1676 the AC6 separation, some fraction of those microbursts will be only observed by one  
1677 AC6 spacecraft. Thus modeling is necessary to capture the compounding influence  
1678 of these statistical effects on AC6.

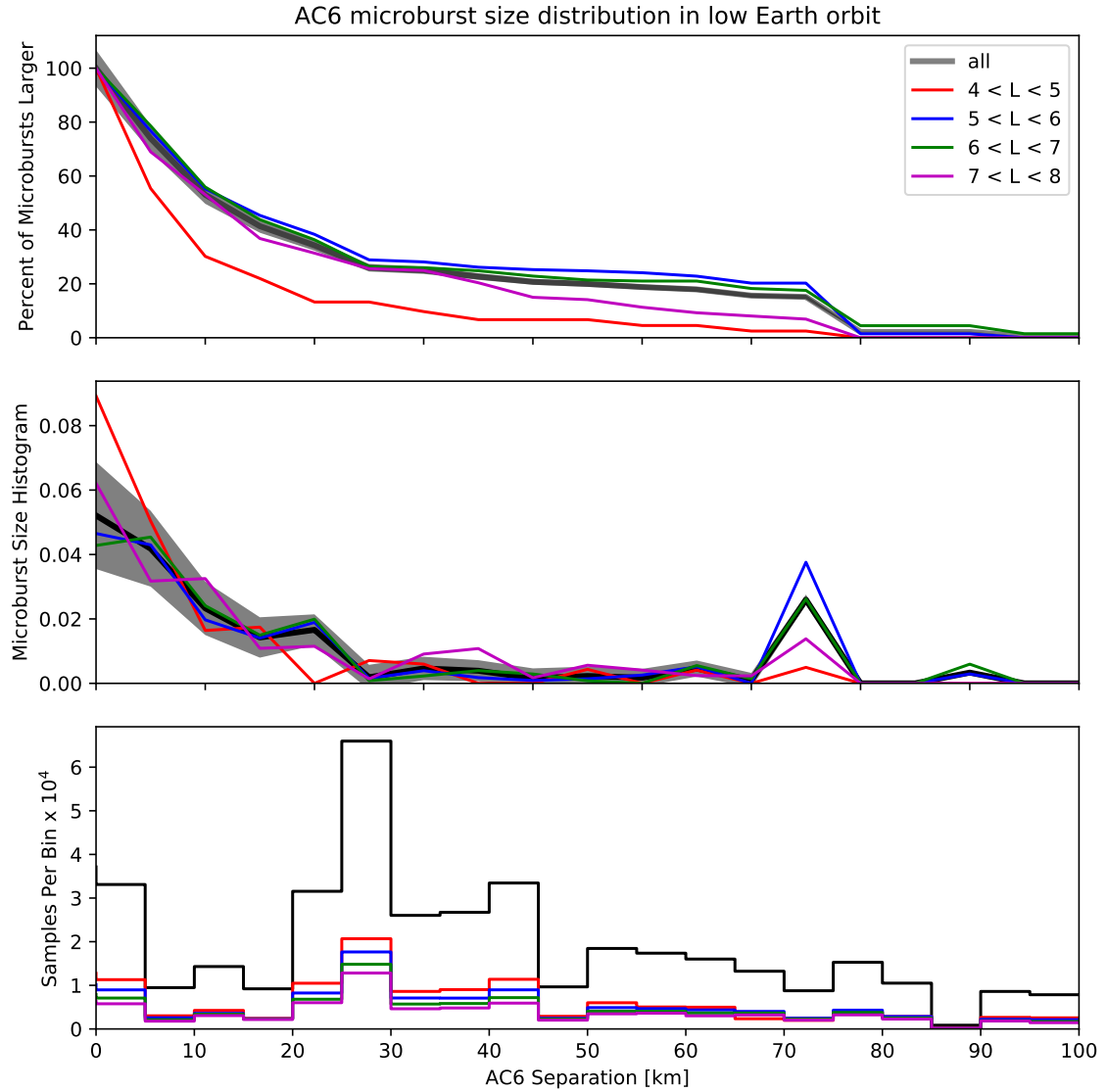


Figure 4.3: Microburst size distribution in low Earth orbit. Panel (a) shows the percent of microbursts observed above that separation after normalizing for the uneven AC6 sampling in separation. Panel (b) shows the microburst probability density (size histogram) as a function of separation. Lastly, panel (c) shows the normalization, i.e. number of simultaneous samples AC6 observed as a function of separation. The colored lines show the distributions binned by  $L$ , and the thick black curve for the entire radiation belt ( $4 < L < 8$ ). The gray shading around the black curve shows the uncertainty due to counting statistics.

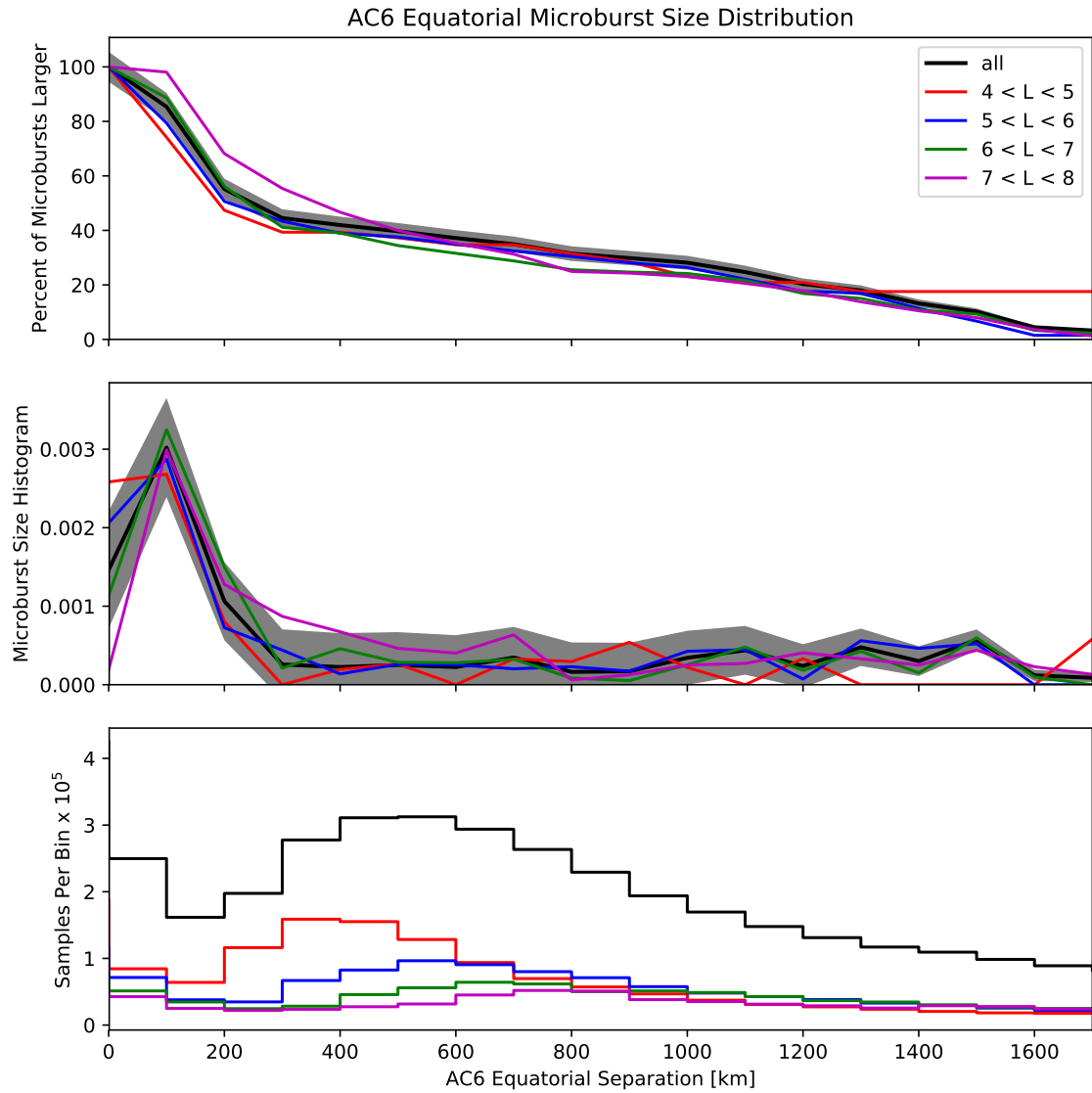


Figure 4.4: Microburst size distribution mapped to the magnetic equator in the same format as Fig. 4.3.

1679 Modeling the Distribution of Microburst Sizes

1680 Monte Carlo and Analytic Models to Calculate  $\bar{F}(s)$

1681 To account for the effects due to microbursts randomly occurring around  
 1682 AC6 with an unknown distribution of microburst sizes, Monte Carlo (MC) and  
 1683 analytic models were developed. These models assume a hypothesized distribution  
 1684 of microburst sizes expressed with a probability density function  $p(d|\theta)$  where  $\theta$  are  
 1685 the dependent variables, and a microburst footprint shape to estimate  $\bar{F}(s)$ . The  
 1686 microburst footprint is assumed to be circular with a diameter  $d$ .  $p(d|\theta)$  can be  
 1687 understood as “the probability of observing a microburst of diameter  $d$ , given the  
 1688 parameters  $\theta$ ”. Various microburst size distributions were considered: a one-size and  
 1689 two-size microburst populations, and continuous  $p(d|\theta)$  such as Maxwell, Weibull,  
 1690 and log-normal.

1691 The Monte Carlo model is the most intuitive. It first randomly scatters  $10^5$   
 1692 microburst centers in a  $400 \times 400$  km grid around AC6. Then each microburst  
 1693 center was assigned a diameter, randomly picked from a  $p(d|\theta)$  distribution after  
 1694  $\theta$  parameters were specified. Spacecraft A is placed at the origin, and spacecraft B  
 1695 is placed along the positive y-axis at distances from spacecraft A corresponding to  
 1696 the AC6 separation bins used in Section 4. Then for each spacecraft B location, the  
 1697 number of microbursts that encompass both spacecraft was counted. The modeled  
 1698 fraction of microbursts observed above  $s$  is then

$$\bar{F}(s) = \frac{\sum_{i>s}^{\infty} n_i}{\sum_{i>0}^{\infty} n_i}. \quad (4.3)$$

1699 where as before the number of microbursts observed by both spacecraft in the  $i$ th bin

1700 is  $n_i$ .

The analytic model, while identical to the MC model, highlights the geometrical concepts connecting  $p(d|\theta)$  and  $\bar{F}(s)$  with geometry arguments similar to Trefall et al. (1966). For a microburst with  $d = 2r \geq s$ , there is an area between AC6 where that microburst will be observed by both spacecraft if the microburst's center lands there. Figure 4.5a-c shows this geometry with the two spacecraft indicated with black dots with varying relations between  $r$  and  $s$ . All microbursts whose center lies inside the circular area of radius  $r$  surrounding either spacecraft will be observed by that spacecraft. If it exists, the intersection of the two circular areas around both spacecraft defines another area,  $A(r, s)$  where a microburst will be observed by both spacecraft if the microburst center lands there. This area can be calculated using the circle-circle intersection area equation,

$$A(r, s) = 2r^2 \cos^{-1} \left( \frac{s}{2r} \right) - \frac{s}{2} \sqrt{4r^2 - s^2}. \quad (4.4)$$

1701 Example geometries where  $A(r, s) > 0$  are shown in Fig. 4.5b and c. With this  
 1702 conceptual model and  $A(r, s)$ , the analytic form of  $\bar{F}(s)$  can be found and is derived  
 1703 in the Supporting Information (SI) Text S1. To demonstrate the effects of random  
 1704 microburst locations near AC6, examples of the analytic and Monte Carlo  $\bar{F}(s)$  curves  
 1705 are shown in Fig. 4.5d for a one-size,  $d = 40$  km microburst population.

1706 Methods for estimating optimal  $\theta$  parameters

1707 At this stage we have all of the ingredients to calculate  $\bar{F}(s)$  given a prescribed  
 1708  $p(d|\theta)$ . For each  $p(d|\theta)$  tested, the optimal  $\theta$  parameters are estimated in this study  
 1709 using the traditional least squares regression and Bayesian inference. While we  
 1710 report the  $\theta$  parameters that minimize least squares, this section focuses on Bayesian  
 1711 inference because it seamlessly incorporates statistical uncertainty in the data. The

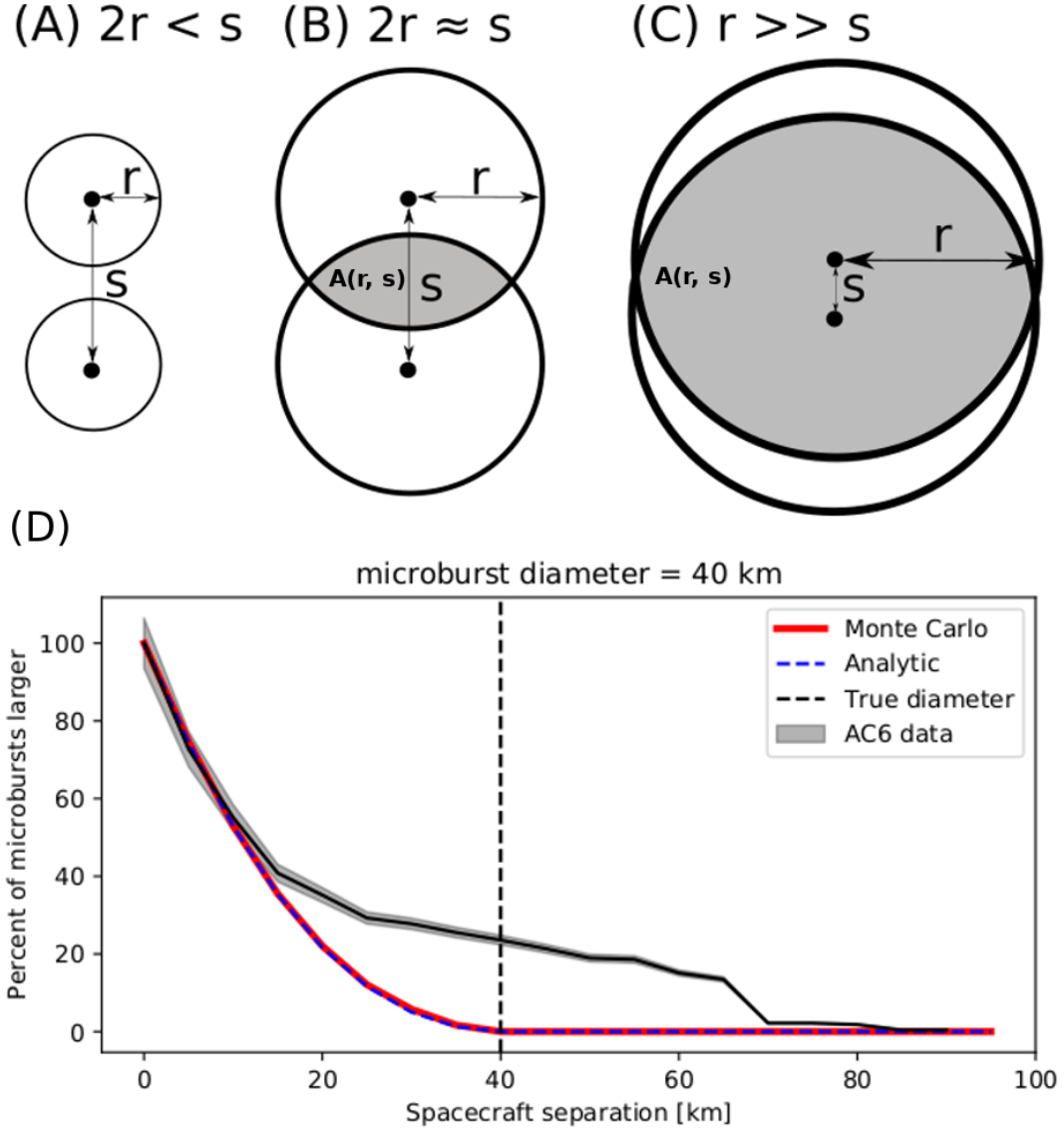


Figure 4.5: Panels A-C show the varying geometries of the analytic model. The two spacecraft are shown as black dots. The enclosing black circle around each spacecraft bounds the area where a microburst will be observed by one or both AC6 units if the microburst's center lies inside the circle. Panel (A) shows the case where microburst diameter is smaller than the AC6 separation and all microbursts will be observed by either unit A or B and never simultaneously. Panel (B) shows the intermediate case where the microburst diameter is comparable to the AC6 separation and some fraction of microbursts will be observed simultaneously. The fraction of the microbursts simultaneously observed is proportional to the circle intersection area  $A(r, s)$  and is shown with grey shading. Panel (C) shows the case where the microburst diameter is much larger than the spacecraft separation and nearly all microbursts will be observed by both spacecraft. Lastly panel (D) shows  $\bar{F}(s)$  from the AC6 data with a solid black line, and modeled MC and analytic  $\bar{F}(s)$  curves for a single-sized microburst distribution with  $d = 40$  km.

1712 uncertainty in the data is then propagated to  $\theta$  which is then no longer an optimal  
 1713 value, rather a distribution of values that is consistent with the observations and its  
 1714 uncertainty.

1715 Bayesian inference is rooted in Bayes theorem of conditional probability. Given  
 1716 the observed  $\bar{F}(s)$  as  $y$ , and model's dependent variables as  $\theta$ , Bayes theorem can be  
 1717 written as

$$p(\theta|y) = \frac{p(y|\theta)p(\theta)}{p(y)}. \quad (4.5)$$

1718  $p(\theta)$  is the distribution of  $\theta$  that describe our prior level of knowledge about that  
 1719 parameter e.g. from earlier microburst size studies, a microburst size must less than  
 1720 500 km in LEO. This is called the prior which is quantified by a PDF such as normal,  
 1721 uniform, etc. Next term is the likelihood,  $p(y|\theta)$ , the conditional probability of  
 1722 obtaining  $y$  given a particular  $\theta$ . The likelihood probability is a probabilistic penalty  
 1723 function that quantifies the discrepancy between the modeled and observed  $\bar{F}(s)$  in  
 1724 terms of the standard error. The resulting PDF of  $\theta$ s consistent with the observations  
 1725 is  $p(\theta|y)$  known as the posterior distribution. The posterior is an update to our prior  
 1726 distributions, modified by the likelihood i.e. the data and its uncertainties. Here, the  
 1727 posterior is used to make inferences regarding the range of  $\theta$  parameters that generate  
 1728 a  $\bar{F}(s)$  that is consistent with the observations. The last parameter in Bayes theorem  
 1729 is  $p(y)$ .  $p(y)$  is the marginal likelihood (evidence) that describes the probability of  
 1730 obtaining  $y$  after marginalizing over all prior variables. Calculation of  $p(y)$  is difficult,  
 1731 and often not necessary for model parameter estimation.

1732 With all of the above terminology, the important takeaway is that the posterior  
 1733 distribution for each model parameter is interpreted as the range of our model's  
 1734 dependent parameters that are consistent with the observations. A 95% credible

1735 interval (CI) for each model parameter is reported here that is interpreted as:  
 1736 assuming a hypothesized  $p(d|\theta)$ , there is a 95% probability that the true  $\theta$  is inside  
 1737 the CI. To sample the posterior distribution, the  $\theta$  parameter space is explored with  
 1738 a Markov Chain Monte Carlo (MCMC) sampler. In a nutshell a Markov Chain is a  
 1739 process that samples random variables that depend on only the previous state of those  
 1740 random variables. Hence a MCMC sampler is a Monte Carlo sampler that samples  
 1741 the  $\theta$  parameter space by picking random  $\theta$  values based on the previous state of  $\theta$ .

1742 The first and one of the most popular MCMC is the Metropolis-Hastings  
 1743 sampler (Hastings, 1970; Metropolis et al., 1953). While the Metropolis-Hastings  
 1744 sampler is explained in detail in Metropolis et al. (1953) and Hastings (1970) and  
 1745 a good introduction given in Sambridge et al. (2006) as well as Sharma (2017), a  
 1746 brief overview is warranted. The Metropolis-Hastings sampler samples the posterior  
 1747 distribution in  $N$  trials. Once an initial set of  $\theta$  is randomly picked from the prior,  
 1748 the  $i^{th}$  trial involves the following steps. First calculate the posterior probability for  
 1749  $\theta_i$ . Then pick a proposal  $\theta_{i+1}$  to jump to, randomly picked near  $\theta_i$  in parameter space.  
 1750 If the  $\theta_{i+1}$  posterior probability is higher than  $\theta_i$ , the MCMC accepts the proposal  
 1751 and moves to  $\theta_{i+1}$ . If the posterior probability of  $\theta_{i+1}$  is smaller than  $\theta_i$ , there is a  
 1752 random chance that  $\theta_{i+1}$  will be accepted or rejected (if rejected,  $\theta_{i+1} = \theta_i$  and a  
 1753 new proposal is generated). This accept/reject criteria allows the sampler to trend  
 1754 to more probable  $\theta$  while also exploring the neighboring regions. After the  $N$  trials,  
 1755 a histogram is made using the accepted  $\theta$ s to produce the posterior distribution for  
 1756 each model parameter.

1757 Estimating optimal parameters for various microburst size models

The MCMC sampler is first used to test the simplest microburst size model where  
 all microbursts are one size and the MCMC will estimate that size. The microburst

size PDF for this model can be expressed as

$$p(d|d_0) = \delta(d - d_0) \quad (4.6)$$

where  $\delta$  is the Dirac Delta function and  $d_0$  is the diameter of all microbursts according to this model. The range of  $d$  that are consistent with the observed  $\bar{F}(s)$  is shown in Fig. 4.6. Assuming this model, there is a 95% probability that the microburst diameter is between 38 and 129 km. As a sanity check the optimal size that minimizes least squares is 73 km.

A slight generalization of the one-size model is a two-size microburst population model that assumes the following microburst PDF

$$p(d|d_0, d_1, a) = a\delta(d - d_0) + (1 - a)\delta(d - d_1) \quad (4.7)$$

where the diameters of the two microburst populations are given by  $d_0$  and  $d_1$  and  $a$  is the parameter that quantifies the relative fractions of the two populations. The result of this model is shown in Fig. 4.7. The fit is slightly better than the one-size model, although that is to be expected given two more free model parameters. A majority, 98 %, of microbursts, have a diameter between 12 and 47 km with a rare population with a diameter between 76 and 234 km. The set of parameters that minimize least squares is 99.5 % of microbursts are small with a size of 21 km and the remaining 0.5 % of microbursts have a 140 km size.

Other, continuous PDFs were tested including: Maxwellian (Maxwell – Boltzmann), log-normal, and Weibull. The range of model parameters that are consistent with the observed  $\bar{F}(s)$  are presented in the SI text S2. These distributions were chosen because they have the following properties that are most realistic: they are continuous, approach 0 in the limit as  $r \rightarrow 0$  (lower bound microburst

1776 size is ultimately limited by the electron gyroradius), and can be symmetrical or  
 1777 asymmetrical.

1778

## Discussion

1779 The LEO microburst  $\bar{F}(s)$  estimated in section 4 shows that a majority of  
 1780 coincident microbursts were observed by AC6 when they were separated by less than  
 1781 a few tens of km. This conclusion is consistent with prior literature and most similar  
 1782 to Parks (1967) who reported that many  $> 15$  keV microbursts are less than 40 km  
 1783 in diameter while others were on average  $80 \pm 28$  km in diameter. Furthermore, these  
 1784 results are similar to the bouncing packet example shown in Blake et al. (1996) with  
 1785 a size of “at least a few tens of kilometers”. The relatively small number of large  
 1786  $> 70$  km microbursts observed by AC6 fit in well with the results from Barcus et al.  
 1787 (1966) and Brown et al. (1965), although the AC6 separation is mostly latitudinal  
 1788 while Barcus et al. (1966) and Brown et al. (1965) used data from pairs of balloons  
 1789 separated predominantly in longitude.

1790 Without knowledge of the microburst shape, a direct comparison between the  
 1791 AC6 and balloon observations is difficult. Trefall et al. (1966) discussed how a  
 1792 hypothetical circular microburst at the scattering location near the magnetic equator  
 1793 will be stretched into an ellipse with a semi-major axis in the longitudinal direction.  
 1794 This stretching effect should be explored further as it introduces an ambiguity from  
 1795 the eccentricity of the ellipse that prevents a direct latitudinal and longitudinal  
 1796 comparison.

1797 When comparing our results to more recent studies, the AC6 microburst size  
 1798 distribution is much larger than the sizes reported in Dietrich et al. (2010) who  
 1799 used very low (VLF) frequency transmission paths and SAMPEX to conclude that  
 1800 microbursts must be smaller than 4 km from a small number of microbursts observed

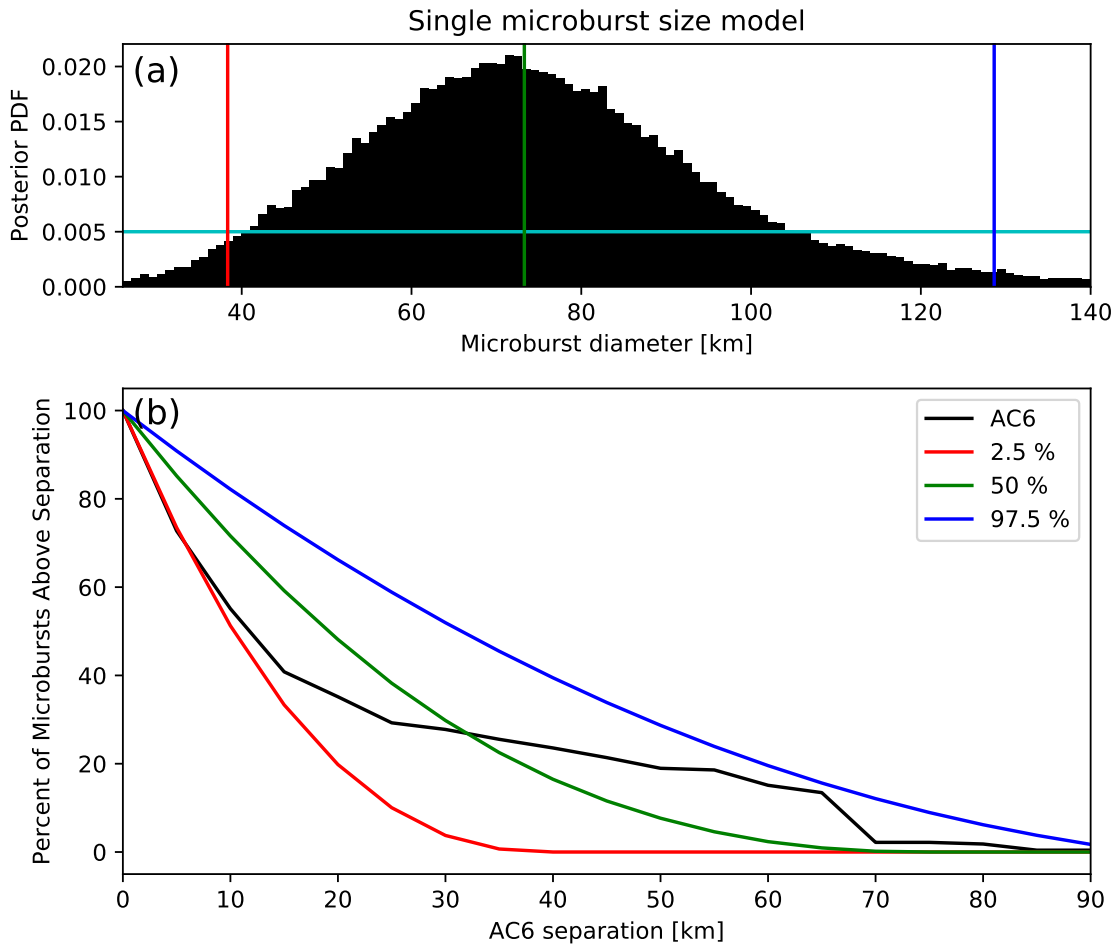


Figure 4.6: Range of plausible microburst sizes assuming all microbursts are one fixed size. Panel (a) shows the posterior probability density function of microburst diameters in black. The red, green, and blue vertical lines at 38, 73, and 129 km represent the 2.5, 50, and 97.5 posterior percentiles, respectively. A uniform prior between 0 and 200 km was assumed for this MCMC run and is shown in cyan. Panel (b) shows the percent of microbursts observed above an AC6 separation for  $4 < L < 8$  in black. The 2.5, 50 and 97.5 size percentiles were estimated from the posterior and plotted in red, green, and blue curves, respectively.

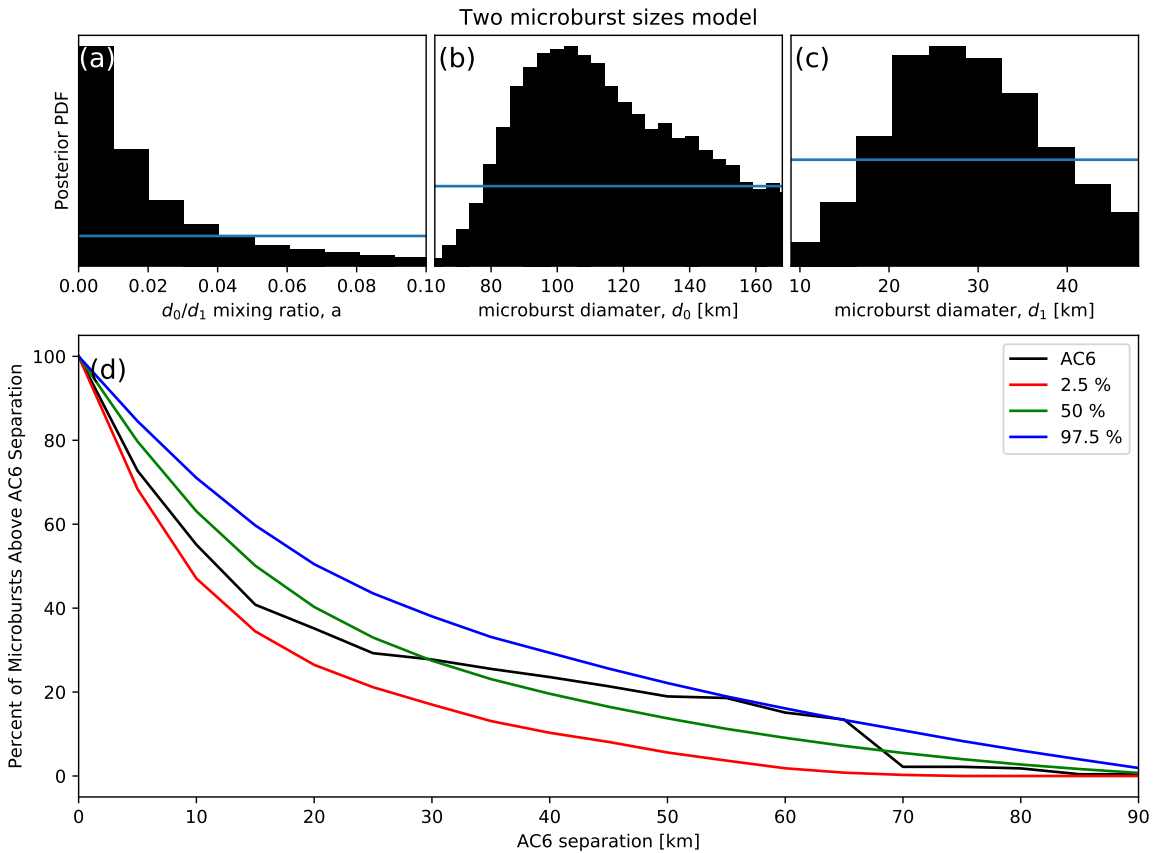


Figure 4.7: Plausible microburst percent curves assuming microburst size distribution is bimodal consisting of two sizes  $d_0$  and  $d_1$  with a mixing term that quantifies the relative occurrence of the  $d_0$  to  $d_1$  microburst populations. Panel (a) shows the posterior distribution for the microburst population mixing term,  $a$  with a median value of 0.02. The  $a$  prior was uniform between 0 and 0.2. Panel (b) shows the posterior distribution for  $d_0$ , the larger microburst population estimated with a uniform prior between 50 and 200 km and the posterior median diameter of 122 km. Panel (c) shows the posterior distribution for  $d_1$ , the smaller microburst population, estimated using a uniform prior between 0 and 50 km with a median diameter of 28 km. Panel (d) is similar to Fig. 4.6b and shows the AC6 microburst fraction for  $4 < L < 8$  in black. A set of 1000 random parameter triples ( $a$ ,  $d_0$ , and  $d_1$ ) were drawn from the posterior and used to generate a family of  $\bar{F}(s)$  curves. At each  $s$  the range of consistent  $\bar{F}(s)$  were quantified by the 2.5, 50 and 97.5 percentiles and shown with the red, green, and blue curves, respectively.

1801 during one SAMPEX radiation belt pass. Dietrich et al. (2010) arrived at their  
 1802 conclusion by looking for temporal coincidence of microbursts and FAST events,  
 1803 subsecond VLF transmission perturbations, but the connection between FAST events  
 1804 and microbursts is not well understood. Lastly, our results are consistent with  
 1805 FIREBIRD-II observations of a  $> 11$  km microburst reported by Crew et al. (2016),  
 1806 and the minority of microbursts observed by AC6 up to  $s \approx 70$  km are consistent  
 1807 with the  $> 51$  km bouncing packet microburst reported in Shumko et al. (2018).

1808 The microburst PDF shown in Fig. 4.3b suggests that the microburst size  
 1809 distribution is bimodal. This has been suggested before by Blake et al. (1996) who  
 1810 noted that the  $> 150$  keV and  $> 1$  MeV microbursts are not always well correlated  
 1811 e.g. Fig. 10 in Blake et al. (1996). The quality of the AC6 data is insufficient to  
 1812 definitively conclude that there are two distinct microburst populations. The different  
 1813 microburst population hypothesis can be better tested with an AC6-like mission with  
 1814 better energy resolution and homogeneous MLT coverage.

1815 The model results from section 4 emphasize that care must be taken when  
 1816 comparing the  $\bar{F}(s)$  curves observed by AC6 and the true microburst size distribution  
 1817 due to the compounding effect of an unknown microburst size distribution, unknown  
 1818 microburst shape, and random microburst locations near AC6. By assuming there is  
 1819 only one microburst size, the results in Fig. 4.6 suggest that there is a 95% probability  
 1820 that the microburst diameter is somewhere between 38 and 129 km, a relatively wide  
 1821 range of values. On the other hand, the two-size model has a smaller variance around  
 1822 the AC6  $\bar{F}(s)$ , which is expected with the addition of two more free parameters. The  
 1823 two size model is interpreted as 98% of microbursts diameters are between 12 and 47  
 1824 km and larger microbursts are very uncommon.

1825 A variety of continuous  $p(d)$  such as the Maxwellian, Weibull and log-normal  
 1826 were also tested. While the continuous microburst PDFs are more realistic, there is

no clear choice of which microburst PDF nature prefers. The one and two-size model are simple to interpret, and the two-size model qualitatively fits the observations the best out of all  $p(d)$  tested. Surely nature does not only have two discrete microburst sizes. Rather, the current evidence and reasoning supports a bimodal and continuous PDF hypothesis. Due to lack of prior observations and theoretical predictions, it is difficult to identify and test a more appropriate  $p(d)$  hypothesis at this time.

The equatorial microburst  $\bar{F}(s)$  estimated in section 4 and Fig. 4.4b in particular shows that the majority of microbursts were observed when the equatorial AC6 separation was less than 200 km. We will now explore how these results compare to prior multi-point measurements of chorus source sizes made near the magnetic equator. The International Sun-Earth Explorers (ISEE 1 and 2) were used by Gurnett et al. (1979) to make one of the first direct chorus source scale measurements. Gurnett et al. (1979) estimated that the wave power correlation scale was on the order of a few hundred km across the background magnetic field. Using the Cluster Wide Band Data measurements Santolik et al. (2003) found the correlation scale of whistler mode chorus waves to be around 100 km near the source region at  $L \approx 4$  and midnight MLT sector. Furthermore, Turner et al. (2017) used the four satellites comprising the Magnetospheric Multiscale Mission and found that rising tone whistler mode chorus elements were phase coherent up to 70 km at  $L \approx 8$ . Lastly, Agapitov et al. (2017, 2011, 2010, 2018) used multiple sets of spacecraft missions with wave measurements near the chorus source region to statistically show that the extent of chorus source region can extend from 600 km in the outer radiation belt to greater than 1,000 km in the outer magnetosphere.

The equatorial microburst size of less than a few hundred km shows that the waves responsible for scattering microburst electrons must have correlated properties on those scales. The wave properties necessary for scattering microburst electrons

1853 e.g. coherence, polarization, wave normal angle, etc. can be identified by studying  
 1854 the waves properties that are only observed by multiple equatorial spacecraft at  
 1855 small separations. These properties can then aid wave-particle scattering model  
 1856 development by constraining the wave properties and scattering modes responsible for  
 1857 scattering microburst electrons. In turn, future models could then make predictions  
 1858 regarding the distribution of microburst sizes in LEO.

1859

### Conclusions

1860 In conclusion, the twin AC6 CubeSats enabled the detailed statistical study  
 1861 of microburst sizes from a two point measurement platform. Roughly 60% of  
 1862 the  $> 35$  keV microbursts were simultaneously observed while AC6 was separated  
 1863 by less than 20 km and the rest were observed up to  $\approx 70$  km separation.  
 1864 Modeling the microburst cumulative distribution function is essential to quantify  
 1865 the relationship between the number of microbursts observed as a function of  
 1866 separation to a hypothesized microburst size distributions. The AC6 microburst  
 1867 data, together with modeling, has hinted at the existence of a bimodal microburst  
 1868 size PDF with the majority of microbursts with a diameter smaller than 40 km and  
 1869 a rare microburst population with a diameter around 100 km. The bimodal size  
 1870 hypothesis may be more comprehensively addressed from LEO spacecraft with more  
 1871 simultaneous microburst observations, homogeneous MLT coverage, and differential  
 1872 energy channels. Moreover, to disentangle the compounding effect that affects two-  
 1873 point microburst measurements, a X-ray imager on a high altitude balloon can observe  
 1874 the atmospheric microburst footprint and determine the microburst size, shape, and  
 1875 any spatial correlations with little ambiguity.

1876 When mapped to the magnetic equator, most microbursts were observed while  
 1877 the mapped AC6 separation was less than 200 km. This correlates well with the sizes

1878 of highly correlated chorus waves and it suggests that the wave properties crucial for  
1879 scattering microbursts must be correlated over relatively small regions. By studying  
1880 the wave properties that are correlated on a few hundred km scales, the dominant  
1881 wave scattering modes may be identified.

1882

### Acknowledgments

1883 This work was made possible with the help from the many engineers and  
1884 scientists at The Aerospace Corporation who designed, built, and operated AC6. M.  
1885 Shumko was supported by NASA Headquarters under the NASA Earth and Space  
1886 Science Fellowship Program - Grant 80NSSC18K1204. D.L. Turner is thankful for  
1887 support from the Van Allen Probes mission and a NASA grant (Prime award number:  
1888 80NSSC19K0280). **Other Aerospace and MSU funding sources...** The AC6 data is  
1889 available at <http://rbspgway.jhuapl.edu/ac6> and the IRBEM-Lib version used for this  
1890 analysis can be downloaded from <https://sourceforge.net/p/irbem/code/616/tree/>.

1891

## CONCLUSIONS AND FUTURE WORK

1892 In this dissertation we have explored the microburst scattering mechanism  
1893 directly in Chapter 2 and indirectly in Chapters 3 and 4. In Chapter 2 we  
1894 used numerous particle and wave instruments on the Van Allen Probes and found  
1895 signatures of microbursts with the Magnetic Electron Ion Spectrometer. To these  
1896 observations we applied the relativistic theory of wave-particle resonant diffusion  
1897 and found that the motion of the microburst electrons was not along single-wave  
1898 particle characteristics in momentum phase space, given the spacecraft position and  
1899 orientation and most probable wave and plasma parameters. This result at first  
1900 appears to contradict the belief that many members of the community hold, that  
1901 microburst precipitation is due to a diffusive process. In reality both are probably  
1902 valid on different time scales. Individual microbursts are probably not scattered  
1903 diffusively, but the combined contribution of an ensemble of microbursts will have  
1904 properties that are well modeled as a diffusion process.

1905 The microburst sizes estimated in prior literature as well as Chapters 3 and  
1906 4 show that there is a large variability in microburst sizes although microbursts  
1907 are relatively small. The study in Ch. 3 gave us a glimpse into the dynamics  
1908 of a rarely observed bouncing packet microburst from a dual point measurement  
1909 platform. This study has shed light on the lower bound latitudinal and longitudinal  
1910 sizes of that microburst, and it was found to be larger than microburst sizes reported  
1911 in recent literature, and somewhat smaller than the microburst sizes observed with  
1912 high altitude balloons in the mid 1960s. Although this is probably an apples to  
1913 oranges comparison because the microburst shape is still unknown and FIREBIRD  
1914 was separated in latitude while balloons were separated mostly in longitude.

1915 The AC6 microburst study in Ch. 4 showed that in LEO, 60% of the 662

1916 microbursts were observed while the AC6 separation was less than a few tens of  
 1917 km while a minority of microbursts were observed up to  $\approx 100$  km separation.  
 1918 These conclusions agree with prior literature from high altitude balloons and LEO  
 1919 spacecraft, although as mentioned before the microburst shape makes comparisons  
 1920 somewhat ambiguous. What shape does a microburst have then? A circular  
 1921 microburst is easy to interpret and model due to its symmetry, but nature is not  
 1922 likely to be so perfect. For example, a circular microburst near the scattering region  
 1923 will be deformed into an ellipse when it gets to LEO by the changing topology of  
 1924 Earth's magnetic field lines. Microbursts may also have an exotic shape, but this can  
 1925 not be further investigated without direct observations of the microburst footprint.  
 1926 One feasible solutions exists: a X-ray imager on a high altitude balloon which will be  
 1927 discussed in the next section.

1928

### Future Work

1929 An extension of the case study in Chapter 2 will be a statistical study using the  
 1930 Van Allen Probes. Other microburst-like events have already been identified by eye.  
 1931 These other events were also simultaneously observed with enhanced wave activity,  
 1932 hence they may be related and a further investigation is warranted. A microburst  
 1933 detection scheme similar to the one used in Chapter 4 can be easily implemented to  
 1934 automatically identify other microbursts for further study. A few compelling questions  
 1935 that can be addressed with this study are: what is the typical pitch angle extent of  
 1936 microbursts? Do these microbursts have a similar MLT distribution to microbursts  
 1937 observed in LEO? What fraction of microbursts were observed during enhanced wave  
 1938 activity? What wave modes and properties are observed during these events? And  
 1939 lastly, what fraction of microbursts can be modeled with a diffusive process?

1940 Another study related to the electron bounce period analysis done in Ch. 3 can

1941 be used to verify magnetic field models and in particular the length of magnetic field  
 1942 lines. Current magnetospheric magnetic field models assume that Earth's magnetic  
 1943 field is relatively static e.g. the International Geomagnetic Reference Field, and  
 1944 superpose that field with a highly dynamic field model who's dynamics are driven by  
 1945 the plasma environment in the magnetosphere and the solar wind. The difficulty lies  
 1946 in accurately modeling this dynamic field, and verifying these models is somewhat  
 1947 difficult. One verification technique involves identifying bouncing packet microbursts  
 1948 observed by SAMPEX and FIREBIRD, and then estimate the electron bounce period.  
 1949 Then a similar analysis to the one in Ch. 3 can be applied to quantify model accuracy  
 1950 for a family of magnetospheric models via the length of the magnetic field line between  
 1951 the bounce points. Identifying the bouncing packet microbursts is not easy, but may  
 1952 be possible with an auto-correlation or machine learning approaches e.g. a neural  
 1953 network.

1954 The last project described here that can be done with existing data is to test  
 1955 the hypothesis that curtains, that were briefly described in Ch. 4, are the remnants  
 1956 of microbursts in the drift loss cone. One way to test this hypothesis is to look for  
 1957 the occurrence rates of curtains eastward and westward of the SAA. If curtains are  
 1958 electrons in the drift loss cone then the SAA will remove curtains as they drift to the  
 1959 east. Thus under the proposed hypothesis the number of curtains should be greater  
 1960 just to the west of the SAA than to the east of the SAA. An alternative approach  
 1961 to test this hypothesis is to estimate how the flux in each curtain changes between  
 1962 the two AC6 units. If curtains are drifting and have a falling energy spectra, then  
 1963 the larger number of slower-drifting electrons will appear as an enhancement in the  
 1964 curtain flux for the trailing spacecraft. If such a trend is apparent then curtains must  
 1965 be drifting, otherwise they may be actively scattered in the same location. Then one  
 1966 idea to entertain is the relation of curtains to precipitation bands reported in prior

1967 literature.

1968 Another approach to determine if microburst scattering is a diffusive or a non-  
 1969 linear process can be done in LEO where the transport of microburst electrons inside  
 1970 the loss cone can be more easily observed. In contrast to particle measurements  
 1971 made near the magnetic equator where the local loss cone is only a few degrees, the  
 1972 loss cone in LEO is  $\approx 60^\circ$  which is much easier to resolve with an instrument with  
 1973 multiple look directions. With this measurement, different scattering mechanisms  
 1974 can be discriminated. If the scattering process is diffusive, then the microburst flux  
 1975 will be monotonically decreasing (or flat) deeper into the loss cone. A non-linear  
 1976 scattering process, on the other hand, will have a more complex pitch angle vs flux  
 1977 profile e.g. a relative maximum at  $0^\circ$ , followed by decreasing flux towards the loss  
 1978 cone boundary. One mission that plans to make this measurement is The Relativistic  
 1979 Electron Atmospheric Loss (REAL) CubeSat. This CubeSat, planned to launch in  
 1980 2021, will sample the inside and outside of the loss cone with a solid state detector  
 1981 with a five look direction collimator.

1982 Lastly, as previously mentioned the microburst shape is an unknown parameter  
 1983 that adds ambiguity when comparing the results from the AC6 study in Ch. 4 and  
 1984 prior literature from balloons. Imaging microburst precipitation is one of the most  
 1985 feasible ways to see the microburst shape. This imaging is possible because when  
 1986 microburst electrons impact the atmosphere, they scatter with Earth's atmosphere  
 1987 and generate bremsstrahlung X-rays. These X-rays have a relatively long mean  
 1988 free path above the Pforzheim maximum above which a balloon-borne imager will  
 1989 predominately observe primary X-rays emitted directly from the microburst electrons.  
 1990 This idea is the basis for the upcoming Balloon Observations Of Microburst Scales  
 1991 (BOOMS) mission. The idea of BOOMS is to fly a set of X-ray pinhole imagers  
 1992 containing a scintillator crystal (to convert from X-rays to visible light) and a grid

1993 of photomultiplier tubes (PMT) underneath to record the distribution of light. With  
1994 triangulation techniques, this distribution of light across the grid of PMTs together  
1995 with instrument modeling can be used to convert between the PMT signal and the  
1996 angular position for each observed X-ray. When exposed for a longer duration, a  
1997 probabilistic image can then be constructed of the microburst X-ray source. Then  
1998 the shape, and any spatial correlations e.g., a microburst train is moving north to  
1999 south, can also be observed.

- 2001 Abel, B. and Thorne, R. M. (1998). Electron scattering loss in earth's inner  
2002 magnetosphere: 1. dominant physical processes. *Journal of Geophysical Research: Space Physics*, 103(A2):2385–2396.
- 2004 Agapitov, O., Blum, L. W., Mozer, F. S., Bonnell, J. W., and Wygant, J. (2017).  
2005 Chorus whistler wave source scales as determined from multipoint van allen probe  
2006 measurements. *Geophysical Research Letters*, pages n/a–n/a. 2017GL072701.
- 2007 Agapitov, O., Krasnoselskikh, V., Dudok de Wit, T., Khotyaintsev, Y., Pickett,  
2008 J. S., Santolik, O., and Rolland, G. (2011). Multispacecraft observations of chorus  
2009 emissions as a tool for the plasma density fluctuations' remote sensing. *Journal of  
2010 Geophysical Research: Space Physics*, 116(A9):n/a–n/a. A09222.
- 2011 Agapitov, O., Krasnoselskikh, V., Zaliznyak, Y., Angelopoulos, V., Le Contel, O.,  
2012 and Rolland, G. (2010). Chorus source region localization in the earth's outer  
2013 magnetosphere using themis measurements. *Annales Geophysicae*, 28(6):1377–  
2014 1386.
- 2015 Agapitov, O., Mourenas, D., Artemyev, A., Mozer, F., Bonnell, J., Angelopoulos, V.,  
2016 Shastun, V., and Krasnoselskikh, V. (2018). Spatial extent and temporal correlation  
2017 of chorus and hiss: Statistical results from multipoint themis observations. *Journal  
2018 of Geophysical Research: Space Physics*, 123(10):8317–8330.
- 2019 Anderson, B., Shekhar, S., Millan, R., Crew, A., Spence, H., Klumpar, D., Blake, J.,  
2020 O'Brien, T., and Turner, D. (2017). Spatial scale and duration of one microburst  
2021 region on 13 August 2015. *Journal of Geophysical Research: Space Physics*.
- 2022 Anderson, K. A. and Milton, D. W. (1964). Balloon observations of X rays in the  
2023 auroral zone: 3. High time resolution studies. *Journal of Geophysical Research*,  
2024 69(21):4457–4479.
- 2025 Barcus, J., Brown, R., and Rosenberg, T. (1966). Spatial and temporal character of  
2026 fast variations in auroral-zone x rays. *Journal of Geophysical Research*, 71(1):125–  
2027 141.
- 2028 Baumjohann, W. and Treumann, R. A. (1997). *Basic space plasma physics*. World  
2029 Scientific.
- 2030 Blake, J., Carranza, P., Claudepierre, S., Clemons, J., Crain, W., Dotan, Y.,  
2031 Fennell, J., Fuentes, F., Galvan, R., George, J., et al. (2013). The magnetic electron  
2032 ion spectrometer (MagEIS) instruments aboard the radiation belt storm probes  
2033 (RBSP) spacecraft. *Space Science Reviews*, 179(1-4):383–421.

- 2034 Blake, J., Looper, M., Baker, D., Nakamura, R., Klecker, B., and Hovestadt, D.  
 2035 (1996). New high temporal and spatial resolution measurements by sampex of the  
 2036 precipitation of relativistic electrons. *Advances in Space Research*, 18(8):171 – 186.
- 2037 Blake, J. B. and O'Brien, T. P. (2016). Observations of small-scale latitudinal  
 2038 structure in energetic electron precipitation. *Journal of Geophysical Research: Space Physics*, 121(4):3031–3035. 2015JA021815.
- 2040 Blum, L., Li, X., and Denton, M. (2015). Rapid MeV electron precipitation as  
 2041 observed by SAMPEX/HILT during high-speed stream-driven storms. *Journal of Geophysical Research: Space Physics*, 120(5):3783–3794. 2014JA020633.
- 2043 Bortnik, J., Thorne, R., and Inan, U. S. (2008). Nonlinear interaction of energetic  
 2044 electrons with large amplitude chorus. *Geophysical Research Letters*, 35(21).
- 2045 Boscher, D., Bourdarie, S., O'Brien, P., Guild, T., and Shumko, M. (2012). Irbem-lib  
 2046 library.
- 2047 Breneman, A., Crew, A., Sample, J., Klumpar, D., Johnson, A., Agapitov, O.,  
 2048 Shumko, M., Turner, D., Santolik, O., Wygant, J., et al. (2017). Observations  
 2049 directly linking relativistic electron microbursts to whistler mode chorus: Van allen  
 2050 probes and FIREBIRD II. *Geophysical Research Letters*.
- 2051 Breneman, A. W., Halford, A., Millan, R., McCarthy, M., Fennell, J., Sample, J.,  
 2052 Woodger, L., Hospodarsky, G., Wygant, J. R., Cattell, C. A., et al. (2015). Global-  
 2053 scale coherence modulation of radiation-belt electron loss from plasmaspheric hiss.  
 2054 *Nature*, 523(7559):193.
- 2055 Brown, R., Barcus, J., and Parsons, N. (1965). Balloon observations of auroral zone  
 2056 x rays in conjugate regions. 2. microbursts and pulsations. *Journal of Geophysical  
 2057 Research (U.S.)*.
- 2058 Capannolo, L., Li, W., Ma, Q., Shen, X.-C., Zhang, X.-J., Redmon, R., Rodriguez,  
 2059 J., Engebretson, M., Kletzing, C., Kurth, W., et al. (2019). Energetic electron  
 2060 precipitation: multi-event analysis of its spatial extent during emic wave activity.  
 2061 *Journal of Geophysical Research: Space Physics*.
- 2062 Claudepierre, S., O'Brien, T., Looper, M., Blake, J., Fennell, J., Roeder, J.,  
 2063 Clemons, J., Mazur, J., Turner, D., Reeves, G., et al. (2019). A revised look  
 2064 at relativistic electrons in the earth's inner radiation zone and slot region. *Journal  
 2065 of Geophysical Research: Space Physics*, 124(2):934–951.
- 2066 Comess, M., Smith, D., Selesnick, R., Millan, R., and Sample, J. (2013). Duskside  
 2067 relativistic electron precipitation as measured by sampex: A statistical survey.  
 2068 *Journal of Geophysical Research: Space Physics*, 118(8):5050–5058.

- 2069 Crew, A. B., Spence, H. E., Blake, J. B., Klumpar, D. M., Larsen, B. A., O'Brien,  
 2070 T. P., Driscoll, S., Handley, M., Legere, J., Longworth, S., Mashburn, K.,  
 2071 Mosleh, E., Ryhajlo, N., Smith, S., Springer, L., and Widholm, M. (2016). First  
 2072 multipoint in situ observations of electron microbursts: Initial results from the  
 2073 NSF FIREBIRD II mission. *Journal of Geophysical Research: Space Physics*,  
 2074 121(6):5272–5283. 2016JA022485.
- 2075 Datta, S., Skoug, R., McCarthy, M., and Parks, G. (1997). Modeling of microburst  
 2076 electron precipitation using pitch angle diffusion theory. *Journal of Geophysical  
 2077 Research: Space Physics*, 102(A8):17325–17333.
- 2078 Dietrich, S., Rodger, C. J., Clilverd, M. A., Bortnik, J., and Raita, T. (2010).  
 2079 Relativistic microburst storm characteristics: Combined satellite and ground-based  
 2080 observations. *Journal of Geophysical Research: Space Physics*, 115(A12).
- 2081 Douma, E., Rodger, C. J., Blum, L. W., and Clilverd, M. A. (2017). Occurrence  
 2082 characteristics of relativistic electron microbursts from SAMPEX observations.  
 2083 *Journal of Geophysical Research: Space Physics*, 122(8):8096–8107. 2017JA024067.
- 2084 Dungey, J. W. (1961). Interplanetary magnetic field and the auroral zones. *Phys.  
 2085 Rev. Lett.*, 6:47–48.
- 2086 Fang, X., Randall, C. E., Lummerzheim, D., Wang, W., Lu, G., Solomon, S. C., and  
 2087 Frahm, R. A. (2010). Parameterization of monoenergetic electron impact ionization.  
 2088 *Geophysical Research Letters*, 37(22).
- 2089 Funsten, H., Skoug, R., Guthrie, A., MacDonald, E., Baldonado, J., Harper, R.,  
 2090 Henderson, K., Kihara, K., Lake, J., Larsen, B., et al. (2013). Helium, Oxygen,  
 2091 Proton, and Electron (HOPE) mass spectrometer for the radiation belt storm  
 2092 probes mission. *Space Science Reviews*, 179(1-4):423–484.
- 2093 Greeley, A., Kanekal, S., Baker, D., Klecker, B., and Schiller, Q. (2019). Quantifying  
 2094 the contribution of microbursts to global electron loss in the radiation belts. *Journal  
 2095 of Geophysical Research: Space Physics*.
- 2096 Gurnett, D., Anderson, R., Scarf, F., Fredricks, R., and Smith, E. (1979). Initial  
 2097 results from the isee-1 and-2 plasma wave investigation. *Space Science Reviews*,  
 2098 23(1):103–122.
- 2099 Hastings, W. K. (1970). Monte carlo sampling methods using markov chains and  
 2100 their applications.
- 2101 Hendry, A. T., Rodger, C. J., and Clilverd, M. A. (2017). Evidence of sub-mev  
 2102 emic-driven electron precipitation. *Geophysical Research Letters*, 44(3):1210–1218.
- 2103 Hoots, F. R. and Roehrich, R. L. (1980). Models for propagation of norad element  
 2104 sets. Technical Report 3, Spacetrack.

- 2105 Horne, R., Glauert, S., Meredith, N., Boscher, D., Maget, V., Heynderickx, D., and  
 2106 Pitchford, D. (2013). Space weather impacts on satellites and forecasting the earth's  
 2107 electron radiation belts with spacecast. *Space Weather*, 11(4):169–186.
- 2108 Horne, R., Thorne, R., Meredith, N., and Anderson, R. (2003). Diffuse auroral  
 2109 electron scattering by electron cyclotron harmonic and whistler mode waves during  
 2110 an isolated substorm. *Journal of Geophysical Research: Space Physics*, 108(A7).
- 2111 Horne, R. B. and Thorne, R. M. (2003). Relativistic electron acceleration and  
 2112 precipitation during resonant interactions with whistler-mode chorus. *Geophysical  
 2113 Research Letters*, 30(10). 1527.
- 2114 Horne, R. B., Thorne, R. M., Shprits, Y. Y., Meredith, N. P., Glauert, S. A., Smith,  
 2115 A. J., Kanekal, S. G., Baker, D. N., Engebretson, M. J., Posch, J. L., et al.  
 2116 (2005). Wave acceleration of electrons in the van allen radiation belts. *Nature*,  
 2117 437(7056):227.
- 2118 Joy, S., Kivelson, M., Walker, R., Khurana, K., Russell, C., and Ogino, T. (2002).  
 2119 Probabilistic models of the jovian magnetopause and bow shock locations. *Journal  
 2120 of Geophysical Research: Space Physics*, 107(A10):SMP–17.
- 2121 Kasahara, S., Miyoshi, Y., Yokota, S., Mitani, T., Kasahara, Y., Matsuda, S.,  
 2122 Kumamoto, A., Matsuoka, A., Kazama, Y., Frey, H., et al. (2018). Pulsating  
 2123 aurora from electron scattering by chorus waves. *Nature*, 554(7692):337.
- 2124 Kletzing, C., Kurth, W., Acuna, M., MacDowall, R., Torbert, R., Averkamp, T.,  
 2125 Bodet, D., Bounds, S., Chutter, M., Connerney, J., et al. (2013). The electric and  
 2126 magnetic field instrument suite and integrated science (EMFISIS) on RBSP. *Space  
 2127 Science Reviews*, 179(1-4):127–181.
- 2128 Klumpar, D., Springer, L., Mosleh, E., Mashburn, K., Berardinelli, S., Gunderson,  
 2129 A., Handly, M., Ryhajlo, N., Spence, H., Smith, S., Legere, J., Widholm, M.,  
 2130 Longworth, S., Crew, A., Larsen, B., Blake, J., and Walmsley, N. (2015). Flight  
 2131 system technologies enabling the twin-cubesat firebird-ii scientific mission.
- 2132 Lee, J. J., Parks, G. K., Lee, E., Tsurutani, B. T., Hwang, J., Cho, K. S., Kim, K.-H.,  
 2133 Park, Y. D., Min, K. W., and McCarthy, M. P. (2012). Anisotropic pitch angle  
 2134 distribution of 100 keV microburst electrons in the loss cone: measurements from  
 2135 STSAT-1. *Annales Geophysicae*, 30(11):1567–1573.
- 2136 Lee, J.-J., Parks, G. K., Min, K. W., Kim, H. J., Park, J., Hwang, J., McCarthy,  
 2137 M. P., Lee, E., Ryu, K. S., Lim, J. T., Sim, E. S., Lee, H. W., Kang, K. I., and  
 2138 Park, H. Y. (2005). Energy spectra of 170–360 keV electron microbursts measured  
 2139 by the korean STSAT-1. *Geophysical Research Letters*, 32(13). L13106.

- 2140 Li, W., Thorne, R., Angelopoulos, V., Bonnell, J., McFadden, J., Carlson, C.,  
 2141 LeContel, O., Roux, A., Glassmeier, K., and Auster, H. (2009a). Evaluation of  
 2142 whistler-mode chorus intensification on the nightside during an injection event  
 2143 observed on the THEMIS spacecraft. *Journal of Geophysical Research: Space*  
 2144 *Physics*, 114(A1).
- 2145 Li, W., Thorne, R., Bortnik, J., Tao, X., and Angelopoulos, V. (2012). Characteristics  
 2146 of hiss-like and discrete whistler-mode emissions. *Geophysical Research Letters*,  
 2147 39(18).
- 2148 Li, W., Thorne, R. M., Angelopoulos, V., Bortnik, J., Cully, C. M., Ni, B., LeContel,  
 2149 O., Roux, A., Auster, U., and Magnes, W. (2009b). Global distribution of whistler-  
 2150 mode chorus waves observed on the THEMIS spacecraft. *Geophysical Research*  
 2151 *Letters*, 36(9). L09104.
- 2152 Li, X., Selesnick, R., Schiller, Q., Zhang, K., Zhao, H., Baker, D. N., and Temerin,  
 2153 M. A. (2017). Measurement of electrons from albedo neutron decay and neutron  
 2154 density in near-earth space. *Nature*, 552(7685):382.
- 2155 Lorentzen, K. R., Blake, J. B., Inan, U. S., and Bortnik, J. (2001a). Observations  
 2156 of relativistic electron microbursts in association with VLF chorus. *Journal of*  
 2157 *Geophysical Research: Space Physics*, 106(A4):6017–6027.
- 2158 Lorentzen, K. R.,Looper, M. D., and Blake, J. B. (2001b). Relativistic electron  
 2159 microbursts during the GEM storms. *Geophysical Research Letters*, 28(13):2573–  
 2160 2576.
- 2161 Lyons, L. R. and Thorne, R. M. (1973). Equilibrium structure of radiation belt  
 2162 electrons. *Journal of Geophysical Research*, 78(13):2142–2149.
- 2163 Manweiler, J. W. and Zwiener, H. M. (2018). Science Operations Center (SOC)  
 2164 RBSPICE Science Data Handbook Revision: e. Technical report, Fundamental  
 2165 Technologies, LLC.
- 2166 Mauk, B., Fox, N. J., Kanekal, S., Kessel, R., Sibeck, D., and Ukhorskiy, A. (2013).  
 2167 Science objectives and rationale for the radiation belt storm probes mission. *Space*  
 2168 *Science Reviews*, 179(1-4):3–27.
- 2169 Meredith, N., Horne, R., Summers, D., Thorne, R., Iles, R., Heynderickx, D., and  
 2170 Anderson, R. (2002). Evidence for acceleration of outer zone electrons to relativistic  
 2171 energies by whistler mode chorus. In *Annales Geophysicae*, volume 20, pages 967–  
 2172 979.
- 2173 Metropolis, N., Rosenbluth, A. W., Rosenbluth, M. N., Teller, A. H., and Teller, E.  
 2174 (1953). Equation of state calculations by fast computing machines. *The journal of*  
 2175 *chemical physics*, 21(6):1087–1092.

- 2176 Millan, R. and Thorne, R. (2007). Review of radiation belt relativistic electron losses.  
 2177 *Journal of Atmospheric and Solar-Terrestrial Physics*, 69(3):362 – 377.
- 2178 Millan, R. M., Lin, R., Smith, D., Lorentzen, K., and McCarthy, M. (2002). X-  
 2179 ray observations of mev electron precipitation with a balloon-borne germanium  
 2180 spectrometer. *Geophysical research letters*, 29(24).
- 2181 Mitchell, D., Lanzerotti, L., Kim, C., Stokes, M., Ho, G., Cooper, S., Ukhorskiy, A.,  
 2182 Manweiler, J., Jaskulek, S., Haggerty, D., et al. (2013). Radiation belt storm probes  
 2183 ion composition experiment (RBSPICE). *Space Science Reviews*, 179(1-4):263–308.
- 2184 Mozer, F. S., Agapitov, O. V., Blake, J. B., and Vasko, I. Y. (2018). Simultaneous  
 2185 observations of lower band chorus emissions at the equator and microburst  
 2186 precipitating electrons in the ionosphere. *Geophysical Research Letters*.
- 2187 Nakamura, R., Baker, D. N., Blake, J. B., Kanekal, S., Klecker, B., and Hovestadt,  
 2188 D. (1995). Relativistic electron precipitation enhancements near the outer edge of  
 2189 the radiation belt. *Geophysical Research Letters*, 22(9):1129–1132.
- 2190 Nakamura, R., Isowa, M., Kamide, Y., Baker, D., Blake, J., and Looper, M. (2000).  
 2191 Observations of relativistic electron microbursts in association with VLF chorus.  
 2192 *J. Geophys. Res*, 105:15875–15885.
- 2193 Nishimura, Y., Bortnik, J., Li, W., Thorne, R., Chen, L., Lyons, L., Angelopoulos,  
 2194 V., Mende, S., Bonnell, J., Le Contel, O., et al. (2011). Multievent study of the  
 2195 correlation between pulsating aurora and whistler mode chorus emissions. *Journal*  
 2196 *of Geophysical Research: Space Physics*, 116(A11).
- 2197 O'Brien, T., Claudepierre, S., Blake, J., Fennell, J. F., Clemons, J., Roeder, J.,  
 2198 Spence, H. E., Reeves, G., and Baker, D. (2014). An empirically observed pitch-  
 2199 angle diffusion eigenmode in the earth's electron belt near  $l^*= 5.0$ . *Geophysical*  
 2200 *Research Letters*, 41(2):251–258.
- 2201 O'Brien, T., Claudepierre, S., Guild, T., Fennell, J., Turner, D., Blake, J., Clemons,  
 2202 J., and Roeder, J. (2016a). Inner zone and slot electron radial diffusion revisited.  
 2203 *Geophysical Research Letters*, 43(14):7301–7310.
- 2204 O'Brien, T. and Moldwin, M. (2003). Empirical plasmapause models from magnetic  
 2205 indices. *Geophysical Research Letters*, 30(4).
- 2206 O'Brien, T. P., Blake, J. B., and W., G. J. (2016b). Aerocube-6 dosimeter data  
 2207 readme. Technical Report TOR-2016-01155, The Aerospace Corporation.
- 2208 O'Brien, T. P., Looper, M. D., and Blake, J. B. (2004). Quantification of relativistic  
 2209 electron microburst losses during the GEM storms. *Geophysical Research Letters*,  
 2210 31(4). L04802.

- 2211 O'Brien, T. P., Lorentzen, K. R., Mann, I. R., Meredith, N. P., Blake, J. B., Fennell,  
 2212 J. F., Looper, M. D., Milling, D. K., and Anderson, R. R. (2003). Energization of  
 2213 relativistic electrons in the presence of ULF power and MeV microbursts: Evidence  
 2214 for dual ULF and VLF acceleration. *Journal of Geophysical Research: Space*  
 2215 *Physics*, 108(A8).
- 2216 Olson, W. P. and Pfitzer, K. A. (1982). A dynamic model of the magnetospheric  
 2217 magnetic and electric fields for july 29, 1977. *Journal of Geophysical Research: Space*  
 2218 *Physics*, 87(A8):5943–5948.
- 2219 Ozaki, M., Miyoshi, Y., Shiokawa, K., Hosokawa, K., Oyama, S.-i., Kataoka, R.,  
 2220 Ebihara, Y., Ogawa, Y., Kasahara, Y., Yagitani, S., et al. (2019). Visualization of  
 2221 rapid electron precipitation via chorus element wave–particle interactions. *Nature*  
 2222 *communications*, 10(1):257.
- 2223 Ozaki, M., Yagitani, S., Ishizaka, K., Shiokawa, K., Miyoshi, Y., Kadokura, A.,  
 2224 Yamagishi, H., Kataoka, R., Ieda, A., Ebihara, Y., Sato, N., and Nagano, I. (2012).  
 2225 Observed correlation between pulsating aurora and chorus waves at Syowa Station  
 2226 in Antarctica: A case study. *Journal of Geophysical Research: Space Physics*,  
 2227 117(A8).
- 2228 Parks, G. (2003). *Physics Of Space Plasmas: An Introduction, Second Edition*.  
 2229 Westview Press.
- 2230 Parks, G. K. (1967). Spatial characteristics of auroral-zone X-ray microbursts. *Journal*  
 2231 *of Geophysical Research*, 72(1):215–226.
- 2232 Reeves, G., Spence, H. E., Henderson, M., Morley, S., Friedel, R., Funsten, H., Baker,  
 2233 D., Kanekal, S., Blake, J., Fennell, J., et al. (2013). Electron acceleration in the  
 2234 heart of the van allen radiation belts. *Science*, 341(6149):991–994.
- 2235 Reeves, G. D., McAdams, K. L., Friedel, R. H. W., and O'Brien, T. P. (2003). Ac-  
 2236 celeration and loss of relativistic electrons during geomagnetic storms. *Geophysical*  
 2237 *Research Letters*, 30(10):n/a–n/a. 1529.
- 2238 Sambridge, M., Gallagher, K., Jackson, A., and Rickwood, P. (2006). Trans-  
 2239 dimensional inverse problems, model comparison and the evidence. *Geophysical*  
 2240 *Journal International*, 167(2):528–542.
- 2241 Santolik, O., Gurnett, D., Pickett, J., Parrot, M., and Cornilleau-Wehrlin, N. (2003).  
 2242 Spatio-temporal structure of storm-time chorus. *Journal of Geophysical Research:*  
 2243 *Space Physics*, 108(A7).
- 2244 Santolk, O., Parrot, M., and Lefevre, F. (2003). Singular value decomposition  
 2245 methods for wave propagation analysis. *Radio Science*, 38(1):n/a–n/a. 1010.

- 2246 Schulz, M. and Lanzerotti, L. J. (1974). *Particle Diffusion in the Radiation Belts*.  
 2247 Springer.
- 2248 Selesnick, R. S., Blake, J. B., and Mewaldt, R. A. (2003). Atmospheric losses of  
 2249 radiation belt electrons. *Journal of Geophysical Research: Space Physics*, 108(A12).  
 2250 1468.
- 2251 Sharma, S. (2017). Markov chain monte carlo methods for bayesian data analysis in  
 2252 astronomy. *Annual Review of Astronomy and Astrophysics*, 55:213–259.
- 2253 Shprits, Y. Y., Meredith, N. P., and Thorne, R. M. (2007). Parameterization  
 2254 of radiation belt electron loss timescales due to interactions with chorus waves.  
 2255 *Geophysical Research Letters*, 34(11):n/a–n/a. L11110.
- 2256 Shprits, Y. Y. and Thorne, R. M. (2004). Time dependent radial diffusion modeling  
 2257 of relativistic electrons with realistic loss rates. *Geophysical Research Letters*,  
 2258 31(8):n/a–n/a. L08805.
- 2259 Shumko, M., Sample, J., Johnson, A., Blake, B., Crew, A., Spence, H., Klumpar, D.,  
 2260 Agapitov, O., and Handley, M. (2018). Microburst scale size derived from multiple  
 2261 bounces of a microburst simultaneously observed with the firebird-ii cubesats.  
 2262 *Geophysical Research Letters*, 45(17):8811–8818.
- 2263 Spence, H. E., Blake, J. B., Crew, A. B., Driscoll, S., Klumpar, D. M., Larsen,  
 2264 B. A., Legere, J., Longworth, S., Mosleh, E., O’Brien, T. P., Smith, S., Springer,  
 2265 L., and Widholm, M. (2012). Focusing on size and energy dependence of electron  
 2266 microbursts from the van allen radiation belts. *Space Weather*, 10(11).
- 2267 Summers, D., Thorne, R. M., and Xiao, F. (1998). Relativistic theory of wave-particle  
 2268 resonant diffusion with application to electron acceleration in the magnetosphere.  
 2269 *Journal of Geophysical Research: Space Physics*, 103(A9):20487–20500.
- 2270 Takahashi, K. and Denton, R. E. (2007). Magnetospheric seismology using multi-  
 2271 harmonic toroidal waves observed at geosynchronous orbit. *Journal of Geophysical  
 2272 Research: Space Physics*, 112(A5).
- 2273 Thorne, R. M. (2010). Radiation belt dynamics: The importance of wave-particle  
 2274 interactions. *Geophysical Research Letters*, 37(22). L22107.
- 2275 Thorne, R. M. and Andreoli, L. J. (1981). *Mechanisms for Intense Relativistic  
 2276 Electron Precipitation*, pages 381–394. Springer Netherlands, Dordrecht.
- 2277 Thorne, R. M., O’Brien, T. P., Shprits, Y. Y., Summers, D., and Horne, R. B. (2005).  
 2278 Timescale for MeV electron microburst loss during geomagnetic storms. *Journal  
 2279 of Geophysical Research: Space Physics*, 110(A9). A09202.

- 2280 Trefall, H., Bjordal, J., Ullaland, S., and Stadsnes, J. (1966). On the extension of  
 2281 auroral-zone x-ray microbursts. *Journal of Atmospheric and Terrestrial Physics*,  
 2282 28(2):225–233.
- 2283 Tsurutani, B. T. and Lakhina, G. S. (1997). Some basic concepts of wave-particle  
 2284 interactions in collisionless plasmas. *Reviews of Geophysics*, 35(4):491–501.
- 2285 Tsurutani, B. T., Lakhina, G. S., and Verkhoglyadova, O. P. (2013). Energetic  
 2286 electron ( $\sim 10$  kev) microburst precipitation,  $\sim 5\text{--}15$  s x-ray pulsations, chorus,  
 2287 and wave-particle interactions: A review. *Journal of Geophysical Research: Space  
 2288 Physics*, 118(5):2296–2312.
- 2289 Tsyganenko, N. (1989). A solution of the chapman-ferraro problem for an ellipsoidal  
 2290 magnetopause. *Planetary and Space Science*, 37(9):1037 – 1046.
- 2291 Tsyganenko, N. A. and Sitnov, M. I. (2005). Modeling the dynamics of the inner  
 2292 magnetosphere during strong geomagnetic storms. *Journal of Geophysical Research: Space  
 2293 Physics*, 110(A3).
- 2294 Turner, D., Claudepierre, S., Fennell, J., O'Brien, T., Blake, J., Lemon, C.,  
 2295 Gkioulidou, M., Takahashi, K., Reeves, G., Thaller, S., et al. (2015). Energetic  
 2296 electron injections deep into the inner magnetosphere associated with substorm  
 2297 activity. *Geophysical Research Letters*, 42(7):2079–2087.
- 2298 Turner, D., Lee, J., Claudepierre, S., Fennell, J., Blake, J., Jaynes, A., Leonard,  
 2299 T., Wilder, F., Ergun, R., Baker, D., et al. (2017). Examining coherency  
 2300 scales, substructure, and propagation of whistler mode chorus elements with  
 2301 magnetospheric multiscale (mms). *Journal of Geophysical Research: Space Physics*,  
 2302 122(11).
- 2303 Ukhorskiy, A. Y., Anderson, B. J., Brandt, P. C., and Tsyganenko, N. A. (2006).  
 2304 Storm time evolution of the outer radiation belt: Transport and losses. *Journal of  
 2305 Geophysical Research: Space Physics*, 111(A11):n/a–n/a. A11S03.
- 2306 Van Allen, J. A. (1959). The geomagnetically trapped corpuscular radiation. *Journal  
 2307 of Geophysical Research*, 64(11):1683–1689.
- 2308 Vernov, S. and Chudakov, A. (1960). Investigation of radiation in outer space. In  
 2309 *International Cosmic Ray Conference*, volume 3, page 19.
- 2310 Walker, A. D. M. (1993). *Plasma waves in the magnetosphere*, volume 24. Springer  
 2311 Science & Business Media.
- 2312 Woodger, L., Halford, A., Millan, R., McCarthy, M., Smith, D., Bowers, G., Sample,  
 2313 J., Anderson, B., and Liang, X. (2015). A summary of the BARREL campaigns:  
 2314 Technique for studying electron precipitation. *Journal of Geophysical Research: Space  
 2315 Physics*, 120(6):4922–4935.

2317 This appendix contains Figs. A.1 and A.2. Figure A.1 shows evidence that  
2318 supports our claim that the “hiss-like” chorus wave observed at 11:17:03 UT with  
2319 EMFISIS WFR instrument on RBSP-A was parallel propagating. The polar angle  
2320 of the wave vector and the supporting planarity of the magnetic field polarization  
2321 shown in Fig. A.1 was calculated using the singular value decomposition (SVD)  
2322 method (Santolk et al., 2003).

2323 Figure A.2 supports the claim that RBSPICE-A observed a 10-80% increase in  
2324 the count rates at the microburst times and pitch angles. Figure A.2 shows the ratio  
2325 of the RBSPICE-A’s EBR count rates during the four microbursts to the quiet time  
2326 one spin before, at the same pitch angles.

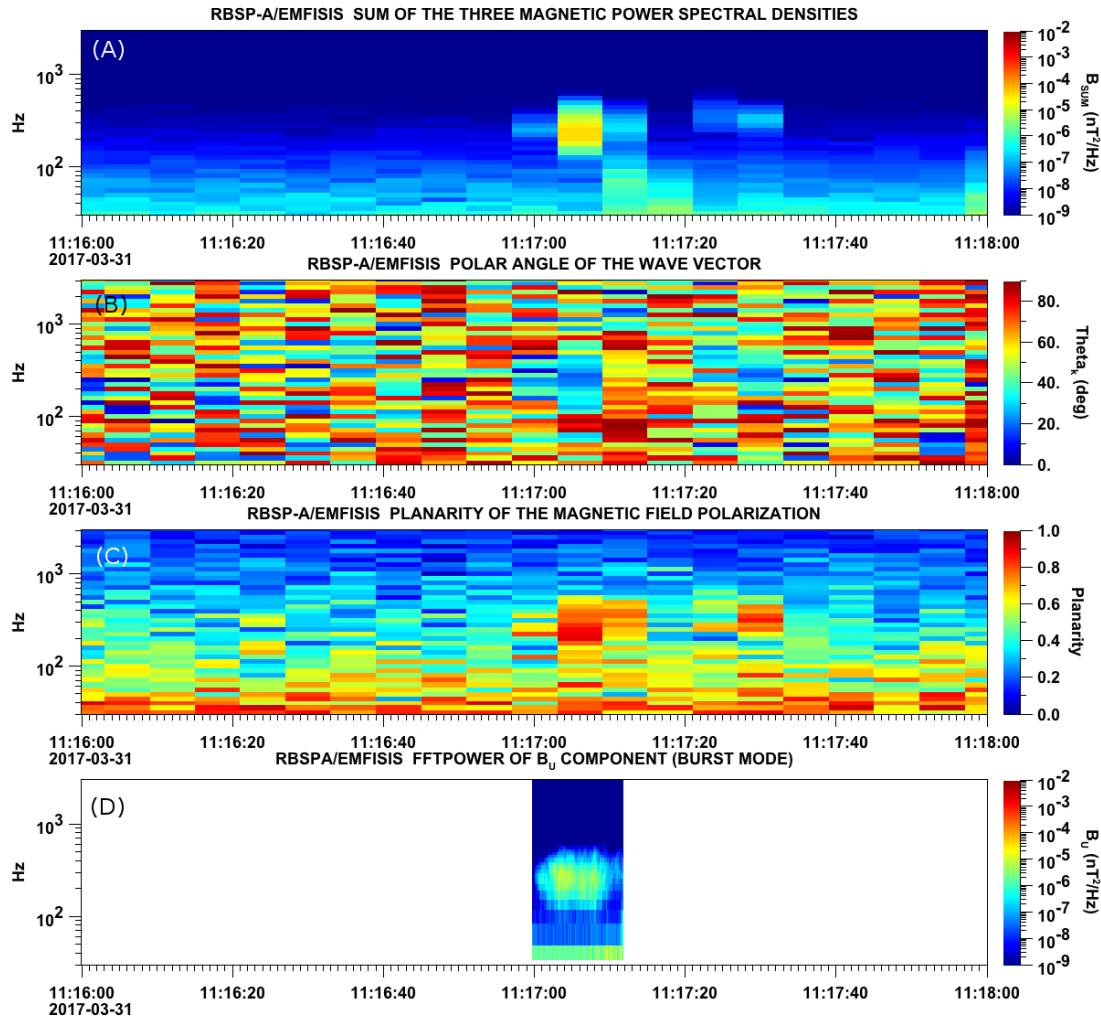


Figure A.1: Panel (A) shows the magnetic power spectral density as a function of frequency and time from the EMFISIS WFR instrument on board RBSP-A. The “hiss-like” wave used for the resonant diffusion analysis was observed starting at 11:17:03 UT. In the same format as panel (A), panel (B) shows the polar angle of the wave vector for this time period. The wave of interest had a normal wave vector,  $\theta_k < 30^\circ$ . Since the results in panel (B) are valid only for high planarity, panel (C) shows planarity in the same format as panels (A) and (B). The wave of interest was found to have a planarity of  $> 0.8$ . Lastly, panel (D) shows the available burst mode data.

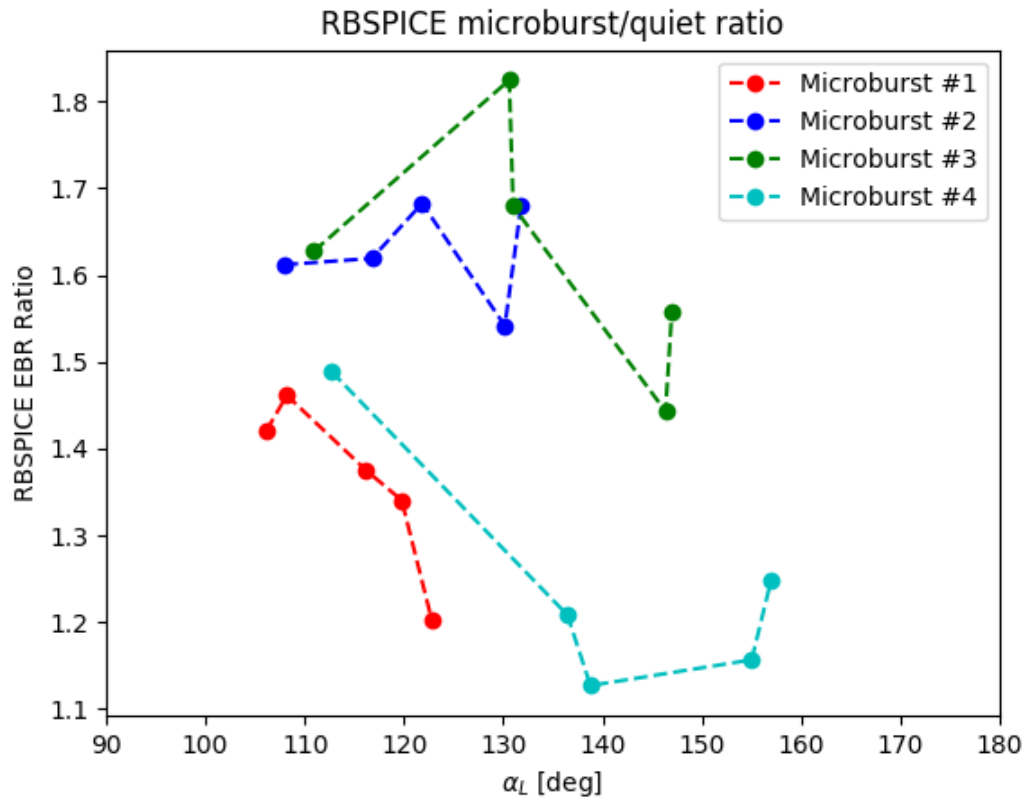


Figure A.2: Ratio of the RBSPICE EBR at microburst times indicated with the black vertical arrows in Fig. 2, to the EBR at the same pitch angles one spin prior (quiet time). The microburst flux was enhanced by 10-80% across  $100^\circ < \alpha_L < 160^\circ$  PA, and appear to be peaked closer to  $\alpha_L = 90^\circ$ .

2327

## APPENDIX: APPENDIX B

2328 This appendix describes the method we used to calculate the time difference and  
 2329 separation between FU3 and FU4 at 06:12 UT on February 2nd, 2015. We used the  
 2330 following method to calculate the clock difference,  $\delta t_c$  and separation,  $d$  between FU3  
 2331 and FU4 at 06:12 UT on February 2nd, 2015.

2332 The relative clock difference was calculated with a cross-correlation time  
 2333 lag analysis on uniquely-identified trains of microbursts that hit both spacecraft  
 2334 simultaneously. Four time periods with coincident microbursts were hand-picked on  
 2335 February 2nd, 2015 and are shown in Figs. B.1-B.4, panels (a) and (b). The cross-  
 2336 correlation time lag analysis was applied to the HiRes time series in panels (a) and  
 2337 (b), and the resulting normalized cross-correlation coefficient as a function of time is  
 2338 shown in panel (c). To validate the peak lag identified in panel (c), FU3's time series  
 2339 was shifted by that lag and is shown in panel (d).

2340 The clock differences from the simultaneous microbursts in Figs. B.1-B.4 were  
 2341 linearly fit to account for the relative clock drift ( $\approx 20$  ms/hour at this time), giving  
 2342 a value of  $\delta t_c = 2.28 \pm 0.12$  s at the time of the microburst analyzed here. This time  
 2343 shift was applied to the HiRes data in Fig. 1. A clock difference of  $\delta t_c = 2.45^{+0.51}_{-0.98}$  s  
 2344 was independently calculated with the FIREBIRD-II telemetry beacon time stamps  
 2345 that were downlinked during operational passes.

2346 We calculate the spacecraft separation, by applying same the cross-correlation  
 2347 time lag analysis on structures assumed to be spatial and are shown in Figs. B.5  
 2348 and B.6. The lag from the peak cross-correlation between these events is a sum of  
 2349 the clock difference and time lag due to the spacecraft separation. We interpret the  
 2350 time lag due to the spacecraft separation as the time difference between when the  
 2351 leading satellite observed a stationary spatial feature, to when the trailing satellite  
 2352 observed the same stationary spatial feature. With the method described above, we  
 2353 find the spatial time lag to be  $\delta t_d = 2.64 \pm 0.12$  s (after we account for the clock  
 2354 difference and its uncertainty). To convert from a spatial time lag to a spacecraft  
 2355 separation, we calculate the satellite velocity. We calculate the velocity using a Two  
 2356 Line Element (TLE), a data format containing the orbit parameters that are used  
 2357 for orbit propagation. With the TLE derived spacecraft velocity,  $v = 7.57$  km/s, the  
 2358 spacecraft separation was  $d = 19.9 \pm 0.9$  km.

2359 An independent method to calculate the spacecraft separation was developed.  
 2360 The separation was calculated using TLEs. The TLE from February 2nd was  
 2361 anomalous and was not used in this analysis. Instead, seven TLEs released up to  
 2362 five days after the microburst event were backpropagated, using the SGP-4 algorithm  
 2363 (Hoots and Roehrich, 1980) that calculates orbital state vectors with perturbations  
 2364 such as Earth's atmosphere, as well as gravitational effects from the moon and sun.  
 2365 Then the predicted spacecraft separations at the time of the microburst event were

2366 averaged to derive a separation of  $d = 18.4 \pm 1.5$  km. These two methods give  
2367 similar separations, which implies that the stationary event assumption used in the  
2368 cross-correlation time lag analysis is reasonable.

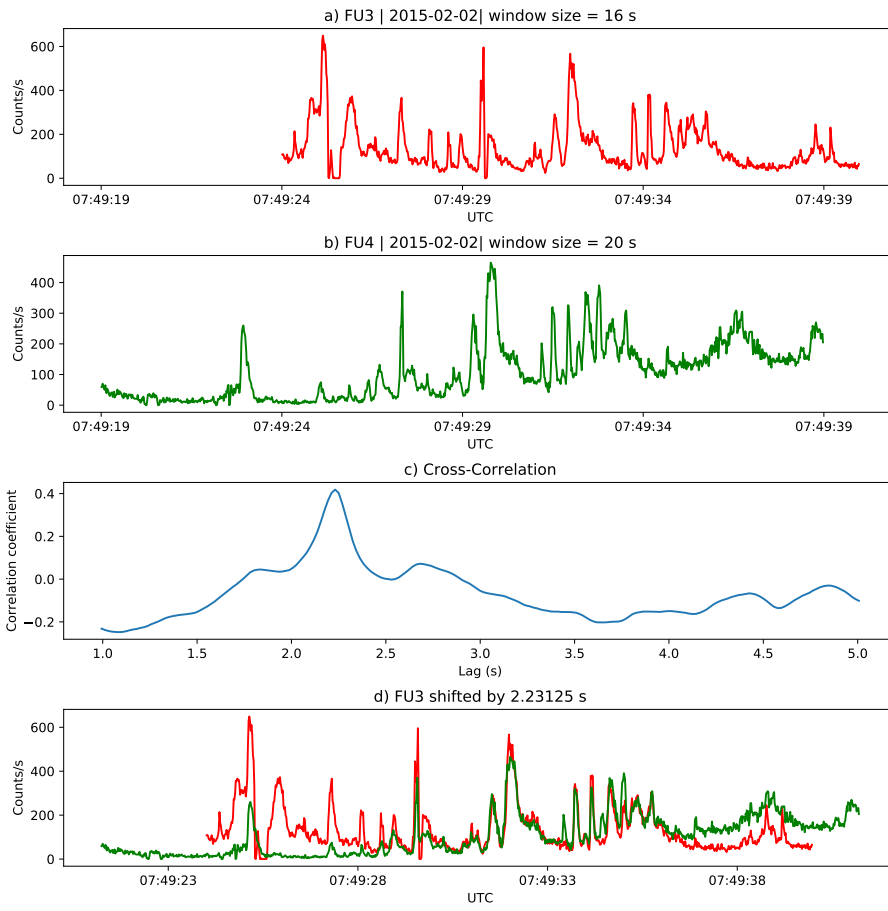


Figure B.1: Cross-correlation time lag analysis applied to a train of microbursts. Panel (a) and (b) show the count rate from the lowest energy channel. Panel (c) shows the cross-correlation coefficient as a function of time lag. Panel (d) shows the shifted timeseries. Clock difference was 2.23 s.

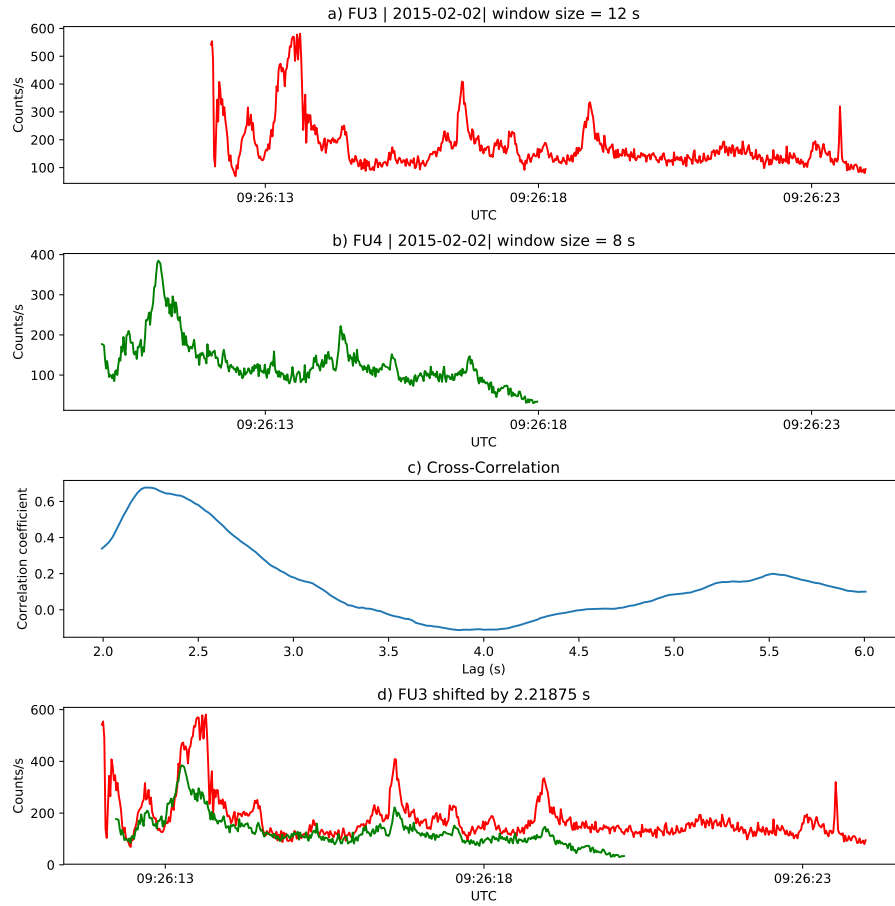


Figure B.2: Same analysis as Fig. B.1 on a different time period. Clock difference was 2.21 s.

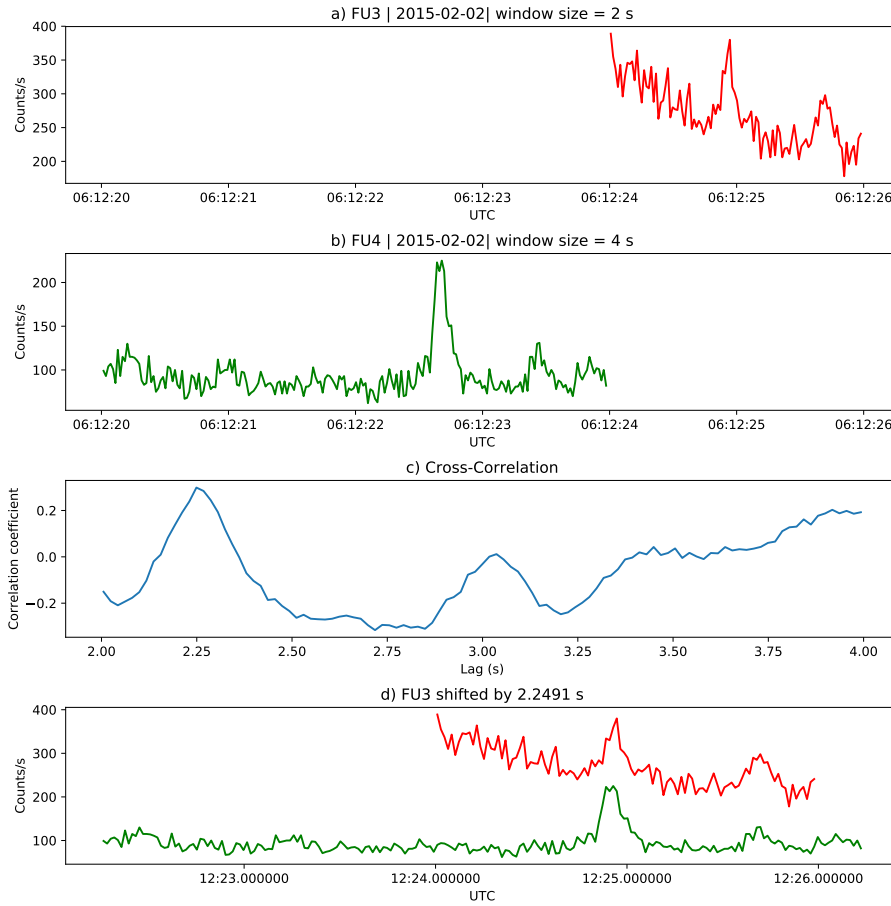


Figure B.3: Same analysis as Fig. B.1 on a different time period. Clock difference was 2.25 s.

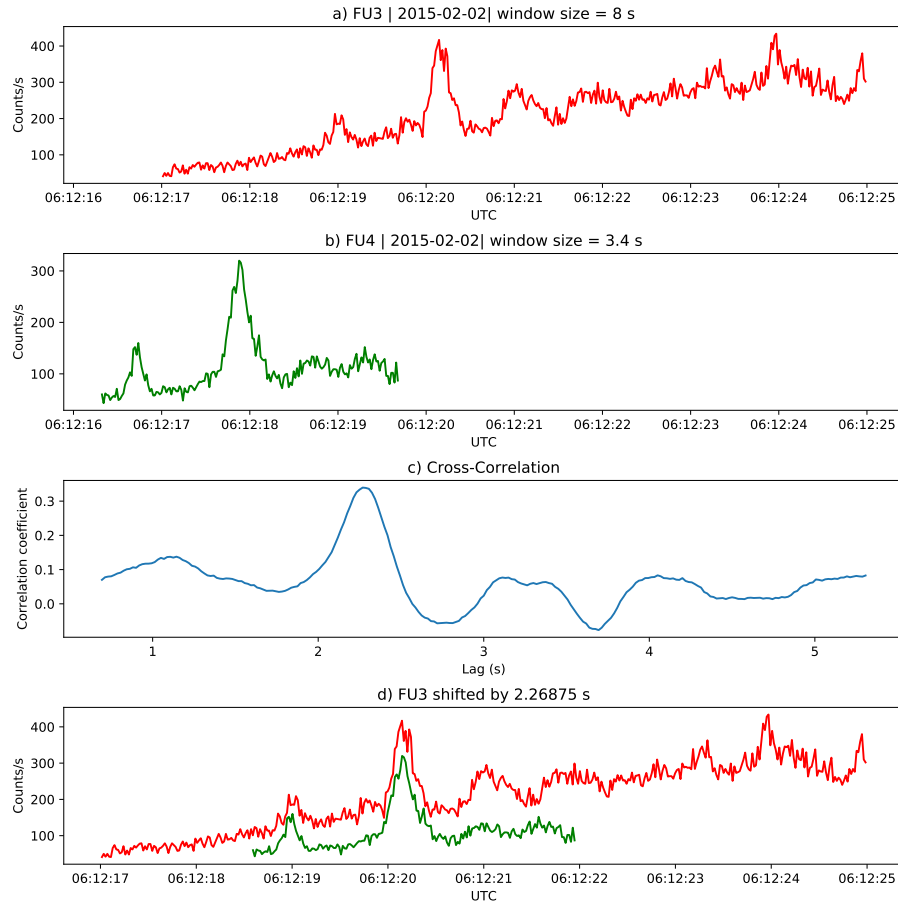


Figure B.4: Same analysis as Fig. B.1 on a different time period. Clock difference was 2.27 s.

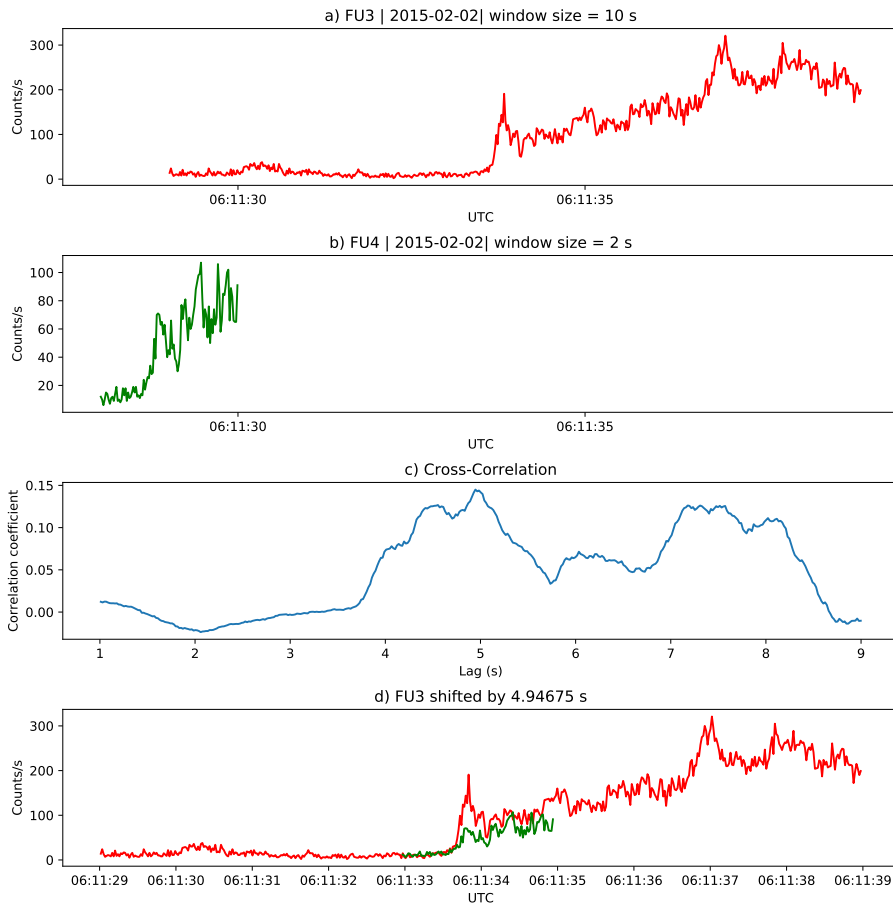


Figure B.5: Same cross-correlation time lag analysis applied to stationary spatial structures. The cross-correlation lag between these events is a sum of the clock difference and time lag due to the spacecraft separation. The lag derived at this time was 4.95 s.

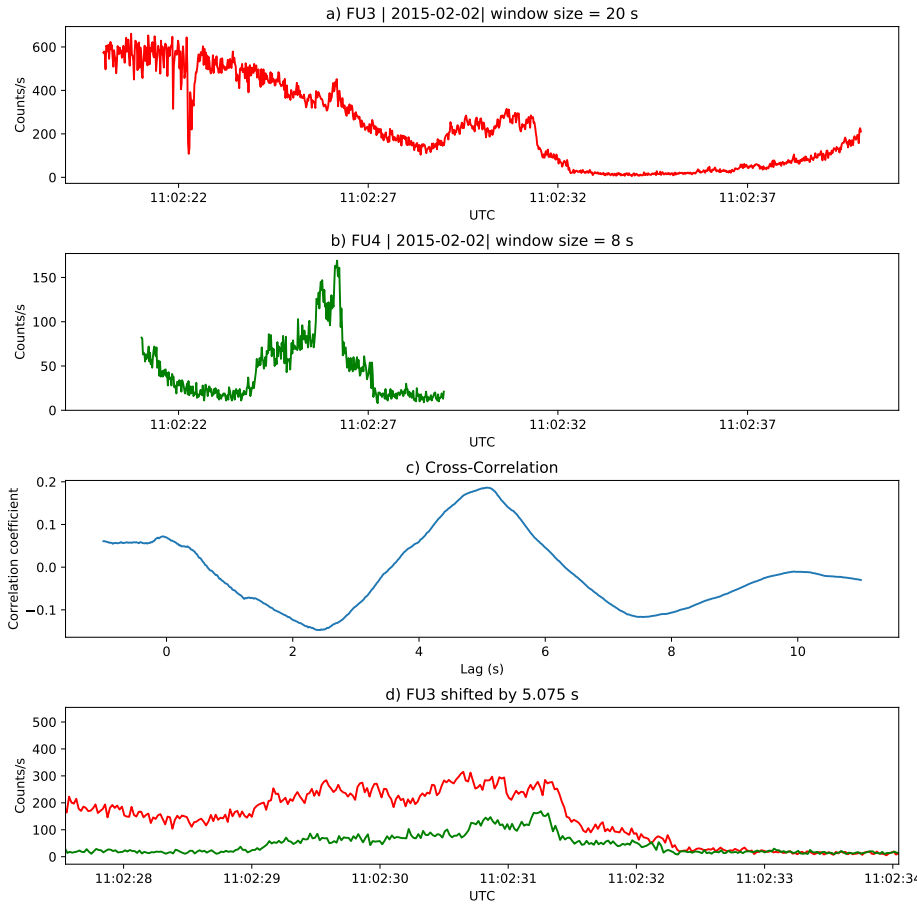


Figure B.6: Same analysis as Fig. B.5 applied to a different stationary spatial feature. The lag derived at this time was 5.01 s.

2370 This appendix contains texts S1-S3. Text S1 derives the analytic model that  
2371 transforms a prescribed microburst PDF into a  $\bar{F}$  curve as a function of AC6  
2372 separation,  $s$ . Text S2 expands on the two-sized microburst model results presented  
2373 in Section 5.3 and the range of optimal model parameters assuming continuous  
2374 microburst PDFs such as the log-normal, Weibull, and Maxwellian. Lastly, text  
2375 S3 presents the percent of microbursts observed in each separation bin, as a function  
2376 of separation and compares it to the observed scale size of chorus waves as a function  
2377 of wave amplitude.

2378 **Text S1: Analytic Derivation of  $\bar{F}(s)$**  Here we derive the integral form of  $\bar{F}(s)$   
2379 under the following assumptions:

- 2380 1. microbursts are circular with radius  $r$   
2381 2. microbursts are randomly and uniformly distributed around AC6.

First recall the area  $A(r, s)$ , given in Eq. 4 in the main text and copied here for convenience

$$A(r, s) = 2r^2 \cos^{-1} \left( \frac{s}{2r} \right) - \frac{s}{2} \sqrt{4r^2 - s^2}. \quad (\text{C.1})$$

2382 A circular microburst who's center lies in  $A(r, s)$  will be observed by both AC6 units  
2383 and is counted in  $\bar{F}(s)$ . Now we derive the integral form of  $\bar{F}(s)$  that accounts for  
2384 the different spacecraft separations and microburst sizes that are distributed by a  
2385 hypothesized PDF  $p(r, \theta)$ .

2386 First we will account for the effects of various spacecraft separation, assuming all  
2387 microbursts are one size. For reference choose of radius,  $r_0$  and spacecraft separation,  
2388  $s_0$  such that  $A(r_0, s_0) > 0$  which implies that some number of microbursts,  $n_0$  will be  
2389 simultaneously observed. Now, if for example the spacecraft separation (or microburst  
2390 radius) is changed such that the area doubles, the second assumption implies that the  
2391 number of microbursts observed during the same time interval must double as well.  
2392 This can be expressed as

$$\frac{n_0}{A(r_0, s_0)} = \frac{n}{A(r, s)} \quad (\text{C.2})$$

2393 and interpreted as the conservation of the microburst area density. By rewriting Eq.  
2394 C.2 as

$$n(r, s) = \left( \frac{n_0}{A(r_0, s_0)} \right) A(r, s) \quad (\text{C.3})$$

2395 it is more clear that the number of microbursts of size  $r$  observed at separation  $s$  is  
2396 just  $A(r, s)$  scaled by the reference microburst area density. The cumulative number  
2397 of microbursts observed above  $s$  is then

$$N(r, s) = \int_s^\infty n(r, s') ds' = \left( \frac{n_0}{A(r_0, s_0)} \right) \int_s^\infty A(r, s') ds'. \quad (\text{C.4})$$

2398 Lastly,  $\bar{F}(s)$  for a single  $r$  is then

$$\bar{F}(s) = \frac{N(s)}{N(0)} = \frac{\int_s^\infty A(r, s') ds'}{\int_0^\infty A(r, s') ds'} \quad (\text{C.5})$$

2399 To incorporate a continuous microburst PDF such as  $p(r) = p_1\delta(r - r_1) + p_2\delta(r -$   
2400  $r_2) + \dots$  we sum up the weighted number of microbursts that each size contributes to

<sub>2401</sub>  $N(s)$  i.e.

$$N(s) = \left( \frac{n_0}{A(r_0, s_0)} \right) \left( \int_s^\infty p_1 A(r_1, s') ds' + \int_s^\infty p_2 A(r_2, s') ds' + \dots \right) \quad (\text{C.6})$$

<sub>2402</sub> The last step is to convert the sum of Dirac Delta functions into a continuous  
<sub>2403</sub> PDF  $p(r)$  after which

$$N(s) = \left( \frac{n_0}{A(r_0, s_0)} \right) \int_s^\infty \int_0^\infty A(r, s') p(r) dr ds'. \quad (\text{C.7})$$

<sub>2404</sub> With these considerations,  $\bar{F}(s)$  is then given by

$$\bar{F}(s, \theta) = \frac{\int_s^\infty \int_0^\infty A(r, s') p(r, \theta) dr ds'}{\int_0^\infty \int_0^\infty A(r, s') p(r, \theta) dr ds'} \quad (\text{C.8})$$

2405 **Text S2: Most probable parameter values for continuous microburst PDFs**

2406 Besides the one and two-size microburst models described in the main text,  
 2407 continuous PDFs such as the log-normal, Weibull, and Maxwellian were fit and their  
 2408 optimal parameters presented here.

2409 For the Maxwellian PDF, we assumed the following form

$$p(r|a) = \sqrt{\frac{2}{\pi}} \frac{r^2 e^{-r^2/(2a^2)}}{a^3}. \quad (\text{C.9})$$

The range of  $a$  consistent with the observed data was found to be between 0 and 35 km. Next, the log-normal distribution of the following form was used

$$p(r|\mu, \sigma) = \frac{1}{\sigma r \sqrt{2\pi}} e^{\left(-\left(\ln(r)-\ln(\mu)\right)^2/(2\sigma^2)\right)} \quad (\text{C.10})$$

and the results are summarized in C.1. Lastly the Weibull distribution of the following form was tested

$$p(r|c, r_0, \lambda) = c \left( \frac{r - r_0}{\lambda} \right)^{c-1} \exp \left( - \left( \frac{r - r_0}{\lambda} \right)^c \right). \quad (\text{C.11})$$

2410 for which the model parameters are summarized in Table C.2.

Table C.1: Range of log-normal model parameters consistent with the observed AC6  $\bar{F}(s)$

percentile (%)	$\mu$	$\sigma$
2.5	1.8	0
50	21.8	0.4
97.5	52.0	1.1

Table C.2: Range of Weibull model parameters consistent with the observed AC6  $\bar{F}(s)$

percentile (%)	$c$	$r_0$	$\lambda$
2.5	0.6	1.3	2.7
50	5.5	26.2	32
97.5	19.3	72.5	72.2

<sup>2411</sup> **Text S3: Comparison of microburst to whistler mode chorus  $\bar{F}(s)$**   
<sup>2412</sup> **TBD**